

# Online Research @ Cardiff

This is an Open Access document downloaded from ORCA, Cardiff University's institutional repository: <https://orca.cardiff.ac.uk/id/eprint/142496/>

This is the author's version of a work that was submitted to / accepted for publication.

Citation for final published version:

Gomaa, Mohamed, Vaculik, Jaroslav, Soebarto, Veronica, Griffith, Michael and Jabi, Wassim ORCID: <https://orcid.org/0000-0002-2594-9568> 2021. Feasibility of 3DP cob walls under compression loads in low-rise construction. Construction and Building Materials 301 , 124079. 10.1016/j.conbuildmat.2021.124079 file

Publishers page: <https://doi.org/10.1016/j.conbuildmat.2021.124079>  
<<https://doi.org/10.1016/j.conbuildmat.2021.124079>>

Please note:

Changes made as a result of publishing processes such as copy-editing, formatting and page numbers may not be reflected in this version. For the definitive version of this publication, please refer to the published source. You are advised to consult the publisher's version if you wish to cite this paper.

This version is being made available in accordance with publisher policies.

See

<http://orca.cf.ac.uk/policies.html> for usage policies. Copyright and moral rights for publications made available in ORCA are retained by the copyright holders.



# Construction and Building Materials

## Feasibility of 3DP cob walls under compression loads in low-rise construction

--Manuscript Draft--

<b>Manuscript Number:</b>	CONBUILDMAT-D-20-08200R2
<b>Article Type:</b>	Research Paper
<b>Keywords:</b>	Additive Manufacturing; 3D printing; Cob; compression test; Limit-state design; Structural performance optimisation
<b>Corresponding Author:</b>	Jaroslav Vaculik University of Adelaide Adelaide, AUSTRALIA
<b>First Author:</b>	Mohamed Gomaa, MSc
<b>Order of Authors:</b>	Mohamed Gomaa, MSc Jaroslav Vaculik, PhD Veronica Soebarto, PhD Michael Griffith, PhD Wassim Jabi, PhD
<b>Abstract:</b>	<p>The rapid adoption of 3D-printing (3DP) technologies in construction, combined with an increased willingness to reduce the environmental impact of building industry, has facilitated reapproaching earth materials for modern building industry. The feasibility of 3DP earth-based materials has been under investigation in recent years, with a particular focus on cob due to its favourable characteristics toward the 3DP process. Yet, there is a lack of definitive information on the construction of 3DP cob. Hence this paper investigates the structural feasibility of 3D-printed cob walls in low-rise buildings. The investigation involved experimental compression tests on 3DP cob samples to obtain key mechanical properties including the compressive strength and elastic modulus. These properties were then used as inputs for structural analyses with respect to three alternate types of 3DP cob wall patterns to evaluate their load-carrying capacity based on a limit-state design framework. Results from the analyses were implemented in modelling an idealised low-rise cob building covering a range of floor spans and wall heights. The analytical study found that 3D-printed walls have the potential to sustain gravity loads typical of residential construction. Further, since the 3DP material was shown to have similar mechanical performance to conventional (non-3DP) cob on the material scale, the 3D-printing process provides the opportunity to produce wall sections that are structurally more efficient than the solid section used in conventional cob construction. This results in lower material consumption, making 3DP cob attractive from the point of view of resource efficiency. An important outcome of the study is the demonstration of a model design technique for low-rise 3DP cob buildings that could be implemented as part of a broader optimisation procedure to satisfy structural and architectural design objectives.</p>

# Feasibility of 3DP Cob Walls Under Compression Loads in Low-Rise Construction

Mohamed Gomaa<sup>ae</sup>, Jaroslav Vaculik<sup>b,c\*</sup>, Veronica Soebarto<sup>a</sup>, Michael Griffith<sup>b,c</sup>, Wassim Jabi<sup>d</sup>

<sup>a</sup> School of Architecture and Built Environment, Horace Lamb Building, University of Adelaide, Adelaide SA5005, Australia.

<sup>b</sup> The School of Civil, Environmental and Mining Engineering, Engineering North Building, University of Adelaide, Adelaide SA5005, Australia.

<sup>c</sup> Bushfire and Natural Hazards Cooperative Research Centre, Melbourne, Australia

<sup>d</sup> The Welsh School of Architecture, Bute Building, Cardiff University, Cardiff CF10 3NB, UK.

<sup>e</sup> School of Engineering, B251- RMIT Bundoora East Campus, RMIT University, Melbourne VIC 3083, Australia.

\*Corresponding Author

Postal address: The School of Civil, Environmental and Mining Engineering, Engineering North Building, University of Adelaide, Adelaide SA5005, Australia.

Phone: (+61 8 8313 5451)

## Abstract

The rapid adoption of 3D-printing (3DP) technologies in construction, combined with an increased willingness to reduce the environmental impact of building industry, has facilitated reapproaching earth materials for modern building industry. The feasibility of 3DP earth-based materials has been under investigation in recent years, with a particular focus on cob due to its favourable characteristics toward the 3DP process. Yet, there is a lack of definitive information on the construction of 3DP cob. Hence this paper investigates the structural feasibility of 3D-printed cob walls in low-rise buildings. The investigation involved experimental compression tests on 3DP cob samples to obtain key mechanical properties including the compressive strength and elastic modulus. These properties were then used as inputs for structural analyses with respect to three alternate types of 3DP cob wall patterns to evaluate their load-carrying capacity based on a limit-state design framework. Results from the analyses were implemented in modelling an idealised low-rise cob building covering a range of floor spans and wall heights. The analytical study found that 3D-printed walls have the potential to sustain gravity loads typical of residential construction. Further, since the 3DP material was shown to have similar mechanical performance to conventional (non-3DP) cob on the material scale, the 3D-printing process provides the opportunity to produce wall sections that are structurally more efficient than the solid section used in conventional cob construction. This results in lower material consumption, making 3DP cob attractive from the point of view of resource efficiency. An important outcome of the study is the demonstration of a model design technique for low-rise 3DP cob buildings that could be implemented as part of a broader optimisation procedure to satisfy structural and architectural design objectives.

43 **Keywords:**

44 Additive manufacturing; 3D printing; Cob; Compression test; Limit-state design; Structural  
45 performance optimisation.

46 **1 Introduction**

47 Digital fabrication technologies, especially 3D printing (3DP), have been witnessing an  
48 increasing uptake in many areas of industry [1]. The construction industry has been adopting a  
49 scaled-up version of 3DP over the past two decades. The increased demand for 3DP  
50 technologies in construction industry has also encouraged researchers to develop novel ideas  
51 toward the full automation of the construction process. Several studies have proven that a well-  
52 developed digital-based process of construction offers various benefits such as larger design  
53 freedom, accelerated productivity, higher degree of customisation, and improved safety of  
54 construction personnel [2], [3].

55 Among the developed techniques of digital fabrication in construction, 3DP has been the most  
56 studied, and has seen a particular focus on cement-based materials [4]–[7]. This has led in  
57 recent years to a rapid spread of 3DP building prototypes around the world, as 3DP technology  
58 has been increasingly embraced by the construction industry [8]. Among the most notable  
59 examples are two concrete buildings constructed in 2019: One is the world’s largest 3DP  
60 building, constructed by Apis Cor in Dubai, United Arab Emirates having two storeys, a plan  
61 area of 640 m<sup>2</sup> and height of 9.5 m (Figure 1a). The second is a 80 m<sup>2</sup> prototype house built by  
62 CyBe as part of their contract with the Saudi Arabia Ministry of Housing with an ambitious  
63 goal to build 1.5 million houses using 3D concrete printing [9] (Figure 1b).



65  
66 *Figure 1: Notable examples of 3DP concrete buildings: (a) Two-storey office building in Dubai*  
67 *constructed by Apis Cor (image credit: Apis Cor), and (b) House in Saudi Arabia constructed by*  
68 *CyBe (image credit: CyBe).*

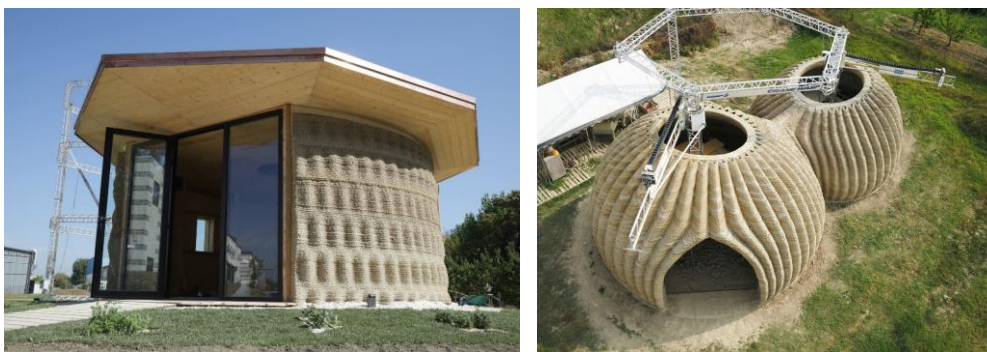
69  
70 The accelerating rate of present-day global construction is well known to produce adverse  
71 environmental impacts. Fortunately, the implementation of digital technology in construction  
72 offers great potential for sustainability [10]. For instance, according to Ford and Despeisse  
73 [11], additive manufacturing (e.g. 3D printing) in construction has several sustainability  
74 benefits such as improving efficiency of resources, extending product life, and upgrading the  
75 value and supply chains.



76 The increased motivation to harness the sustainability benefits of 3DP technology in  
77 construction has also recently renewed the interest in earthen construction materials after  
78 decades of dormancy [11],[14]. Significantly, a recent study by Hamard et al. [12] has revealed  
79 that considerable sustainability benefits can be realised through the integration of digital  
80 fabrication techniques with earth-based materials, which have low embodied energy, are highly  
81 recyclable, and generate limited waste. Furthermore, these materials typically have high  
82 material density and thus high thermal mass, which can lead to favourable thermal comfort  
83 performance, particularly in areas where there is a large difference in daytime and night-time  
84 temperatures [12], [14], [15]. As a further benefit, earth-based materials are significantly  
85 cheaper per unit volume compared to conventional building materials such as concrete or steel  
86 [13], and can under many circumstances result in more economical small-scale structures.

87 Earthen construction has three famous forms: cob, adobe, and rammed earth. Cob, which is the  
88 focus of this study, is a traditional building material comprising a mixture of subsoil, water and  
89 straw (or other fibres). It differs from adobe and rammed earth by using a wet-based  
90 construction technique that offers freedom of design while not requiring formwork. It also  
91 exhibits excellent maintenance characteristics through the ability to apply add-ons or create  
92 cuts-out, even after the cob is dry [16]–[18]. This makes cob particularly attractive for 3D  
93 printing.

94 In recent years, the performance of cob manufactured digitally using 3D printing has been the  
95 focus of emergent research at several institutions such as IAAC, Cardiff University and  
96 Plymouth University [19]. A proof of concept of the idea has also been successfully  
97 demonstrated by the 3D-printer manufacturer WASP by constructing two prototypes of cob  
98 houses [20] (Figure 2). And while the focus of the studies to date has been to examine feasibility  
99 with regard to aspects such as geometry and fabrication process [21], thermal performance  
100 [22], and life cycle assessment [8], the examination of structural performance not yet been  
101 carried out in any significant detail. As a consequence, the pursuit of fully implementing 3D  
102 cob in modern construction remains hindered by a lack of engineering guidance for structural  
103 design. Overcoming this hurdle requires establishing a reliable body of experimental test data  
104 on the mechanical (structural engineering) properties of 3DP cob, as well the development of  
105 appropriate structural design and modelling tools that can be used by design engineers.



106  
107  
108 *Figure 2: 3DP cob houses fabricated by WASP (image credit: WASP).*  
109

110 While numerous studies have focused on the mechanical properties of 3DP concrete [1][7], to  
111 the knowledge of the authors only a single study to date has investigated the mechanical  
112 properties of any 3DP cob-like material [23]. This study, by Perrot et al., tested material made  
113 from a mix of earth material and alginate seaweed biopolymer (as a substitute for straw which  
114 is traditionally used), and demonstrated compressive strength similar to that of conventional  
115 (non-3DP) cob. Besides this study, however, there is no existing research into the mechanical  
116 properties of traditional (straw-fibre) cob passed through the 3DP process. Moreover, there are,  
117 to the authors' knowledge, no existing studies involving the translation of these fundamental  
118 properties toward engineering design of 3DP cob on neither the wall nor building scale.

119 To address these gaps, this study aims to provide insight into the expected loadbearing  
120 capability 3DP cob walls. This is approached in two stages: The first conducts an experimental  
121 compression test on 3DP cob samples to obtain the basic mechanical properties including  
122 compressive strength, elastic modulus, and Poisson's ratio. The second stage evaluates the wall  
123 section geometries (dimensions) necessary to perform a loadbearing function in typical  
124 residential construction for alternate 3DP patterns through a first-principles analysis approach.  
125 This is combined with an optimisation process to examine the relationship between structural  
126 efficiency and several design variables such as variable room size, floor heights, number of  
127 storeys, and wall section properties. The outcomes are expected to empower architects and  
128 engineers with a model approach for the structural design and construction process of 3DP cob.  
129 The paper also acts as an essential part of larger overarching research by the authors on the  
130 feasibility of 3DP cob in modern construction.

131 The paper is structured as follows: Section 2 undertakes a review of previous material testing  
132 of traditional (non-3DP) cob to establish typical range of material properties. Section 3 reports  
133 original compression tests on 3DP cob cylinders. Section 4 demonstrates a simplified design  
134 approach for estimating the loadbearing capability of 3DP walls, and examines their feasibility  
135 in residential construction, including an investigation of the sensitivity on material properties.  
136 Section 5 demonstrates the essential design process on a fictional small house, and Section 6  
137 concludes with a summary and recommendations for future work.

## 2 Structural performance of cob as a building material

140 Cob buildings are well-known for their durability and resistance to weathering [24]. However,  
141 the lack of a binding agent (e.g. cement) makes the compressive strength of cob (typically < 2  
142 MPa) much weaker compared to concrete (typically > 20 MPa) and even other traditional  
143 materials such as rammed earth (typically 5–20 MPa). This combined with the fact that cob  
144 buildings were historically built without reinforcement means that building heights are  
145 typically restricted to low-rise (i.e. between one to three storeys), with most being 2-storey  
146 [13]. Some very rare but notable examples of high-rise are found however, such as the world  
147 heritage-listed towers in Yemen which have up to 9 storeys [25][26]. **The low compressive  
148 strength of cob** compared to other traditional materials is generally **compensated for** by large  
149 wall thickness [27], [28].

150 Multi-storey cob houses typically incorporate light-weight floor and roof systems in the form  
151 of timber framing. Floors usually comprise joists with wooden decking, while roofs include  
152 timber rafters plus purlins and have a typically sloped profile with extended eaves to protect  
153 walls from rain. Walls in multi-storey houses are typically around 600 mm thick, and for  
154 efficiency they are typically made thinner at upper storeys relative to the ground floor [13],  
155 [28].

156 Mechanical properties of cob are dependent on a number of factors: subsoil composition  
157 including clay content, straw and water content, degree of compaction, and the general quality  
158 of the workmanship [29], [27], [30]. Studies into the influence of the mix composition have  
159 demonstrated compressive strength to be generally enhanced by increased straw content (due  
160 to acting as local tensile reinforcement) and reduced by higher moisture content [16], [31].  
161 Table 1 provides a generalised overview of test studies to date, summarising the range of  
162 reported compressive strength ( $f_c$ ) and elastic modulus ( $E$ ). It is important to note that the cob  
163 mixtures in these studies vary in terms of their composition, with the intention of the table  
164 being to demonstrate the broad range of property values rather than parametric trends.

165 Compressive strength can be considered to be the fundamental engineering property of interest  
166 for earthen-material structures, as it controls the loadbearing capacity of walls under gravity  
167 loads [13], [32]. As demonstrated by Table 1, compressive strength usually falls between 0.4–  
168 1.35 MPa, although values less than 0.1 MPa and as high as 5 MPa have been reported. Notably,  
169 low values of strength ( $< 0.4$  MPa) are usually for mixtures with high moisture content ( $> 15\%$ )  
170 [13], [31]. Among the studies in Table 1, the range of scatter in compressive strength (where  
171 reported) varies between 2–21%. Stochastic variability has implications toward the lower-  
172 bound characteristic value that can be adopted in limit-state design as discussed later.

173 The reported elastic modulus varies drastically among the published studies. Most values fall  
174 within the range 4–200 MPa, but outlying values as low as 0.33 MPa and as high as 850 MPa  
175 have also been reported. As will be shown later (Section 4) the elastic modulus has particular  
176 importance toward the loadbearing capacity of 3DP cob walls due to the potential for local  
177 buckling of the printed sections.

178 Data on Poisson's ratio is limited to two studies [29] and [33], who reported mean values of  
179 0.15 and 0.12 respectively.

180 Additionally, cob exhibits considerably higher material ductility than rammed earth and adobe  
181 [29], [33], as characterised by the ability to maintain stress resistance into the post-peak phase  
182 of stress-strain response. Miccoli et al. [29] demonstrated this to be the case under both  
183 compressive and shear loading. The observed ductility of cob can be attributed to the influence  
184 of fibres, with fibres used in cob being typically longer than in adobe. This favourable  
185 behaviour implies that cob may be able to outperform the alternate earthen materials under  
186 deformation-controlled loading such as earthquake. While this warrants further investigation,  
187 it is outside the scope of the current paper.

188

Table 1: Compressive strength ( $f_c$ ), elastic modulus ( $E$ ), and Poisson's ratio ( $\nu$ ) for non-3DP cob. Values presented as a range (a–b) cover different cob mixtures, if applicable. Percentages in brackets denote the intra-batch CoV if specified. Unless noted otherwise, the mixtures have moisture content (mc) < 15%.

Source	$f_c$ (MPa)	$E$ (MPa)	$\nu$
Houben and Guillaud (1994) [34]	0.10	–	–
Saxton (1995) [31]	0.35–1.75 (mc<15%) 0–0.2 (mc>15%)	–	–
Ziegert (2003) [35]	0.45–1.40	170–335	–
Coventry (2004) [36]	0.48–1.24 (3%–10%)	0.33–1.25	–
Keefe (2005) [24]	0.6–1.4	–	–
Akinkurolere et al. (2006) [16]	0.6–2.2	–	–
Weismann and Bryce (2006) [28]	0.77	–	–
Quagliarini et al. (2010) [13]	0.24–0.40 (mc>15%)	4.0–40 *	–
Pullen and Scholz (2011) [32]	0.45–0.89 (22%)	11–69	–
Minke (2012) [37]	0.5–5.0	60–850	–
Miccoli et al. (2014) [29]	1.59 (2%)	651 (68%)	0.15 (4%)
Rizza and Bottger (2015) [38]	0.60 (13%)	71.5	–
Brunello et al. (2018) [39]	0.71–0.87 (8%–15%)	–	–
Quagliarini and Maracchini (2018) [33]	1.12 (5%)	16.9 (4%)	0.12 (66%)
Vincelas et al. (2018) [40]	0.50–0.76	110–350	–
Wright (2019) [30]	1.22–1.53 ** (18%–21%) 0.77–2.45 ***	–	–
Jimenez Rios and O'Dwyer (2020) [41]	0.70 (12%)	143 (23%)	–

Notes:

\*  $E$  determined from reported stress-strain curves

\*\* Specimens with varied straw content

\*\*\* Specimens with varied soil clay content

194

The only study, to the authors' knowledge, that has undertaken material testing on any 3D-printed earthen material is a recent study by Perrot et al. [23], which used a cob-like material incorporating alginate seaweed biopolymer as a substitute for straw. The produced material achieved a compressive strength between 1.2–1.8 MPa, demonstrating that 3DP earth material has the potential to achieve compressive strength toward the higher end of that for conventional non-3DP cob (Table 1).

201

### 3 Compression tests on 3D-printed cob cylinders

This section reports laboratory tests performed on 3DP-cob cylinders to quantify fundamental mechanical properties necessary for design. Among the side objectives of these tests was also to ensure that the 3D-printing process did not produce any unexpected strength reduction compared to conventional non-3DP cob (Table 1). Such a reduction could be conceivable due



207 to the altered form of the material as a result of being stacked in layers rather than being a  
208 homogeneous mass. Due to the lack of a structural testing standard specific to earthen  
209 materials, the study adopted general principles for the testing of quasi-brittle materials, as  
210 recommended by [42].

### 211 3.1 Test specimens

#### 212 3.1.1 Material mix preparation

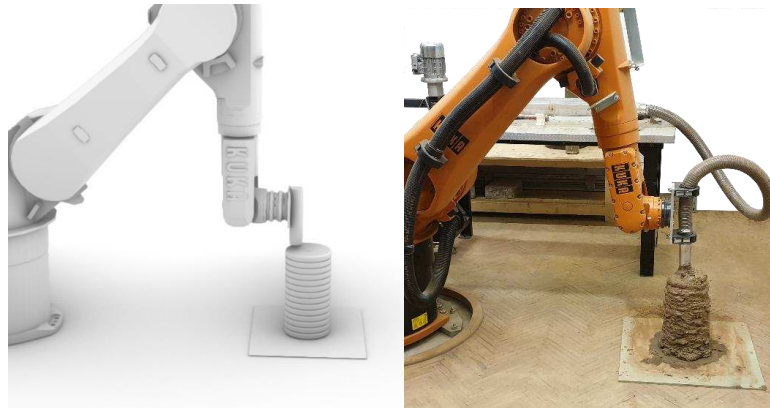
213 In the 3D-printing process, for both concrete and earth-based materials, the material must flow  
214 efficiently through the system, be deposited as layers and harden properly to reach a structural  
215 integrity threshold within an acceptable time frame that meets the construction requirements  
216 [5] [23]. The properties of the input material must therefore be formulated carefully considering  
217 both their wet (pre-hardening) and hardened states. According to Weismann and Bryce [28]  
218 and Hamard et al. [12], traditional cob mixture typically comprises 78% subsoil, 20% water  
219 and 2% fibre (straw) by weight. This however produces a nearly dry mixture with low  
220 flowability, making it unsuitable for 3D printing. To overcome this, the adopted mixture  
221 followed an alternate, 3DP-suitable, mix developed by the authors in a precursor study [22]. In  
222 the adopted mix, the water content was increased to an average of 25%, subsoil was reduced  
223 to 73%, and straw was maintained at 2% (by weight). The mixture used locally-sourced wheat  
224 straw chopped into lengths of 30–50 mm, as longer straw lengths were found to be unsuitable  
225 by causing blockage inside the extrusion system. The composition of the subsoil (sourced from  
226 Cardiff, UK) was examined using methods recommended by [28], [43] and found to contain  
227 19–20% clay and 80–81% aggregate/sand. This is in good agreement with subsoil composition  
228 recommended in the literature (15–25% clay to 75–85 % aggregate/sand) [28], [12].

229 It is worth mentioning that, despite the intentionally high moisture content of the input mixture,  
230 the moisture content of the final printed cob becomes slightly reduced by the 3DP extrusion  
231 process. This is caused by the pressurisation of the mixture inside the extrusion system, which  
232 leads to moisture release in the form of leakage around the cartridge connections. The moisture  
233 loss in this study was estimated at around 3%, leaving the printed cob at 22% moisture content.  
234 This reduction is considered favourable as it improves the structural stability of the printed  
235 layers and also reduces drying shrinkage. Note that while shrinkage is an important aspect of  
236 cob construction, it was not a specific focus of this study, especially as the observed shrinkage  
237 in the specimens was low (approx. 2%) and the specimens showed no signs of cracking during  
238 the drying period.

#### 239 3.1.2 3D-printing of specimens

240 The test specimens in this study were printed using a 6-axis KUKA KR60 HA robotic arm  
241 (Figure 3). The software package for robotic control was Rhinoceros via Grasshopper and  
242 KUKA PRC®. An electromechanical dual ram extruder, developed by the authors in a previous  
243 study [21], was used for material delivery. The test specimens comprised 400 mm-tall cob  
244 cylinders with an average diameter of 200 mm (Figure 4). Each cylinder was contoured as 14  
245 successive layers, with an average height of 29 mm per layer. The nozzle had a 45 mm  
246

248 diameter. The robotic arm moved in a circular pattern at an average movement speed of 35  
249 mm/sec.



251  
252 *Figure 3: Robotic 3D printing of the cob specimens: virtual model on Rhino (left) and the real output*  
253 *(right).*

### 254 3.2 Test arrangement and method

256 The test specimens were subjected to uniform axial load in a universal testing machine (Figure  
257 4). Prior to the test, the machine loading platens were coated with grease to minimise frictional  
258 confinement. The rate of applied load was approximately 0.08 MPa/min, with each test taking  
259 about 10 minutes to perform. The test apparatus monitored the applied load and axial  
260 (longitudinal) displacement between the two platens using a built-in linear variable differential  
261 transformer (LVDT). Due to the impracticality of applying strain gauges to the irregular surface  
262 of the specimens, horizontal deformation (necessary to evaluate the Poisson's ratio) was  
263 quantified in post-processing by digital image correlation using high-resolution video footage  
264 captured during the test. A total of three samples were tested, with examples of the failed  
265 specimens shown in Figure 5.



267  
268 *Figure 4: Compression test setup (left) and the cylindrical specimen (right).*



Figure 5: Typical examples of specimens after compressive failure.

### 3.3 Results

The observed stress-strain behaviour is shown in Figure 6. Each specimen exhibits quasi-brittle response with an approximately linear rising branch, followed by a reduction in slope up to the peak, and continued softening in the post-peak zone. The plotted stress was calculated as  $\sigma = P/A$ , where  $P$  is the applied force and  $A$  is the average cross-sectional area of the specimen ( $31,400 \text{ mm}^2$ ). Axial strain was computed as  $\epsilon_{\text{axial}} = \Delta/L$ , where  $\Delta$  is the displacement measured platen-to-platen, and  $L$  is the length of the specimen (400 mm).

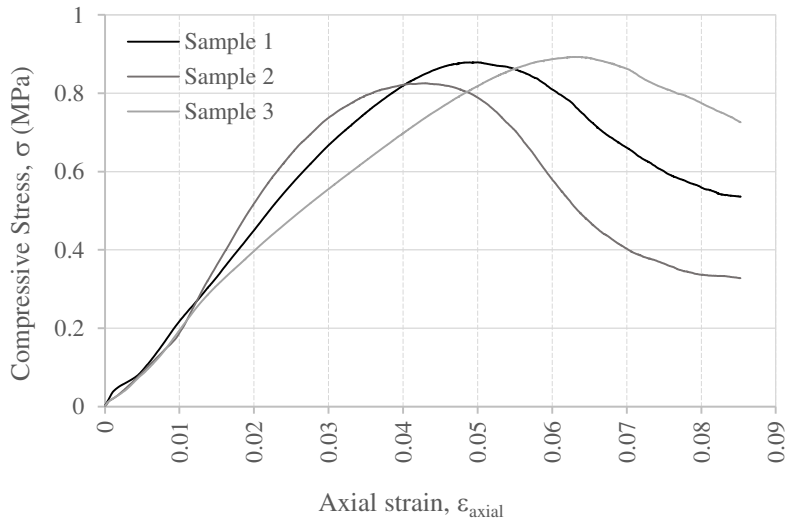


Figure 6: Stress-strain behaviour of compression test specimens.

The properties derived from the test, including the compressive strength, elastic modulus, and Poisson's ratio, are summarised in Table 2.

283 The average unconfined compressive strength ( $f_c$ ) of the specimens is 0.87 MPa. This compares  
 284 favourably to strength of non-3DP cob reported in the literature (Table 1) with most reported  
 285 values falling within 0.4–1.35 MPa. On this basis there does not appear to be any obvious  
 286 reduction in strength introduced by the 3DP process. Despite a limited number of samples, the  
 287 variability is low (CoV = 4%). It should be noted that the reported compressive strength  
 288 corresponds directly to the peak stress reached during the test. To account for the size-effect in  
 289 quasi-brittle materials as well as confinement resulting from the compression apparatus platens,  
 290 test standards typically apply a correction factor to the measured peak stress to obtain a size-  
 291 invariant unconfined compressive strength. For instance if these results were to be interpreted  
 292 according to the test standard for masonry units (EN 772-1, [44]) a correction factor of 1.25  
 293 would apply on the basis of the test specimen dimensions. However, for conservatism, the  
 294 subsequent analysis in Section 4 takes this factor as 1.

295 Elastic modulus ( $E$ ) was evaluated as the slope of the  $\sigma$ - $\epsilon$  curve along the initial rising branch  
 296 before the onset of nonlinearity. Mean  $E$  of the tested specimens is 22.9 MPa (CoV = 10%).  
 297 This falls into the lower end of values determined for non-3DP cob (Table 1) (median  $\approx$  60  
 298 MPa). As demonstrated later (Section 4), the elastic modulus is influential on wall loadbearing  
 299 strength as it controls local buckling of the printed cross section, thus providing impetus for  
 300 future investigations into 3DP-suitable cob mix design to focus on not just the material's  
 301 strength but also stiffness.

302 Poisson's ratio ( $\nu$ ) was calculated as the ratio of lateral to longitudinal strain over the initial  
 303 elastic portion of response, producing a mean value of 0.22. This is consistent with the range  
 304 of scatter reported by [29] and [33] for non-3DP cob (Table 1).

305  
 306 Table 2: Results of compression test, including unconfined compressive strength ( $f_c$ ), elastic  
 307 modulus ( $E$ ), and Poisson's ratio ( $\nu$ ).

Sample	$f_c$ (MPa)	$E$ (MPa)	$\nu$
1	0.88	22.7	0.16
2	0.83	25.3	0.28
3	0.89	20.6	0.21
Mean value	0.87	22.9	0.22
CoV	4%	10%	28%

#### 309 4 Evaluation of the feasibility of loadbearing 3DP cob walls

310 This section examines the feasibility of using 3DP cob walls as loadbearing in low-rise  
 311 residential construction. The design actions considered are from gravity loads only, and do not  
 312 include wind or earthquake loading which can be highly region-specific.

## 314 4.1 Method of structural analysis

1  
2 315 Although the expected behaviour of 3DP cob walls under gravity loads is expected to resemble  
3 316 that of walls constructed using conventional materials such as unreinforced masonry or  
4 317 concrete, the design-code provisions for these established materials are not necessarily  
5 318 translatable to 3DP cob. Therefore, the wall's load-carrying capacity **was** evaluated using first  
6 319 principles while adhering to the concepts of limit-state design. This includes using  
7 320 characteristic values of material stress capacity (rather than mean values), and applying factors  
8 321 to upscale design loads and downgrade the design capacity.

### 12 4.1.1 Limit-state design

13  
14 323 Capacity-adequacy checks were performed according to a limit-state design framework. With  
15 324 reference to the compressive strength, the design check can be expressed using the generalised  
16 325 form

$$19 N_c^* < \phi N_c. \quad (1)$$

20  
21 326 In Eq. (1),  $N_c^*$  is the design compressive force acting on the wall, determined as  $\gamma S$ , with  $S$   
22 327 being the unfactored working load and  $\gamma$  being the load factor (greater than 1). In turn,  $\phi N_c$  is  
23 328 the design compressive capacity of the wall, determined as the basic capacity  $N_c$  multiplied by  
24 329 the capacity-reduction factor  $\phi$  (less than 1). To account for the fact that the material stress  
25 330 capacities exhibit stochastic variability, capacity  $N_c$  **was** calculated using the characteristic  
26 331 compressive strength,  $f_c'$ , defined as the lower-5th-percentile value.

### 30 4.1.2 Wall cross-section patterns

31  
32 333 Three different types of printed patterns were considered as part of this feasibility study; these  
33 334 are referred to as A, B and C as shown in Figure 7. These three patterns align carefully with  
34 335 the wall sections in two previous studies that investigated thermal performance and life cycle  
35 336 assessment of 3D-printed cob by Gomaa et al. [22] and Alhumayani et al. [8] respectively. The  
36 337 criteria for choosing these wall sections are based on meeting multiple design requirements  
37 338 including adequate thermal insulation, efficient use of material, and structural integrity. A  
38 339 generic vertical cross section of a wall is shown in Figure 8. Because the 3D-printing process  
39 340 in the current study **dispensed** the cob material in circular cross sections while being flattened  
40 341 down into wider layers, the resulting vertical shells **did** not have a constant thickness (Figure  
41 342 8). Rather, the shell thickness **ranged** between an inner value,  $t_{in}$ , and outer value,  $t_{out}$ , as shown.  
42 343 Both  $t_{in}$  and  $t_{out}$  could be estimated according to a number of parameters in the 3D-printing  
43 344 process setup, such as the layer height, nozzle size and the extrusion rate [21]. On the basis of  
44 345 typical printed patterns,  $t_{out} - t_{in}$  **was** taken as 20 mm, with the average thickness ( $t$ ) being in  
45 346 turn defined as  $t = (t_{in} + t_{out})/2$ . For each section type, the nominal wall depth ( $d$ ) is defined as  
46 347 the distance between the centrelines of the two external 'face' shells; and  $a$  denotes the  
47 348 dimension between the internal 'web' shells (Figure 8). In all of the subsequent analyses,  $a$  is  
48 349 taken equal to  $d$ .

56 350



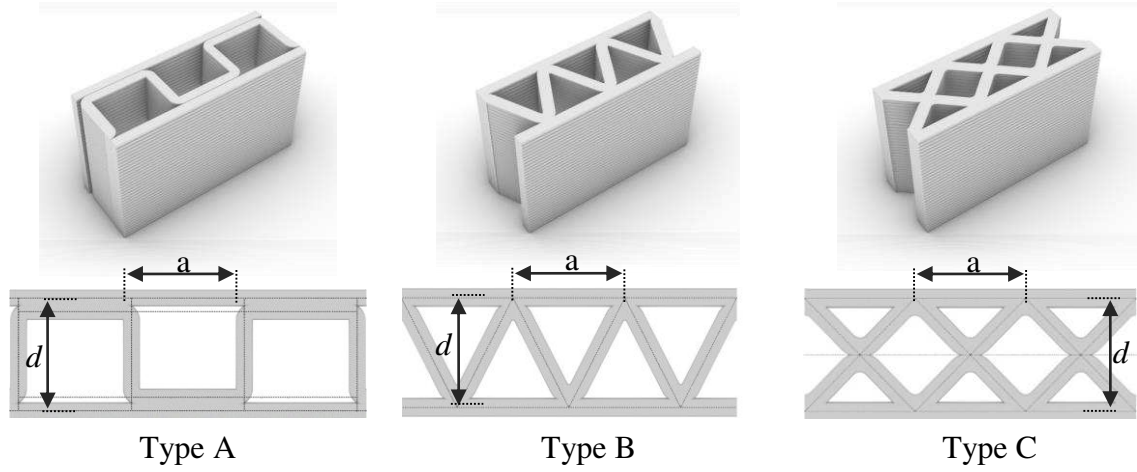


Figure 7: Alternate printed patterns considered in this study.

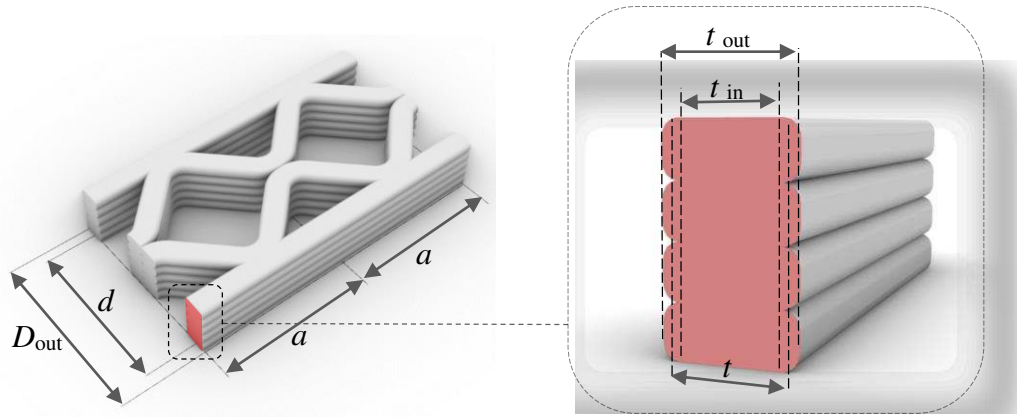


Figure 8: Definition of geometric properties along a generic cross section.

Evaluation of the wall's compressive capacity requires the wall's area ( $A$ ) and out-of-plane moment of inertia ( $I$ ). These were calculated for each type of section by conservatively taking the shell thickness as  $t_{in}$ . For comparative purposes, the sectional properties of the three pattern types are provided in Table 3.

Table 3: Section properties for the alternate printed patterns. Each considers a reference section with  $t_{in} = 50\text{mm}$  and  $d = 500\text{mm}$ . Properties accented by a bar ( $\bar{X}$ ) denote the value per unit length run of the wall.

Wall Type	$t_{in}$ (mm)	$t$ (mm)	$d$ (mm)	$\bar{A}$ (mm <sup>2</sup> /m)	$\bar{I}$ (mm <sup>4</sup> /m)	$\bar{P}_{buck,loc}$ (kN/m)
A	50	60	500	200,000	$9.32 \times 10^9$	145
B	50	60	500	212,000	$8.60 \times 10^9$	137
C	50	60	500	241,000	$9.23 \times 10^9$	181

### 361 4.1.3 Wall compressive strength

1  
2 362 The compressive strength of a generic (3DP or no-3DP) cob wall requires evaluation of its  
3 363 member capacity under combined axial load and eccentricity moment with the potential for  
4 364 global buckling combined with material failure. A 3DP wall however differs from a solid wall  
5  
6 365 in that the section capacity can be governed by not just material crushing, but also by local  
7 366 buckling of the shell structure. Thus, the compressive stress capacity of the section was  
8  
9 367 evaluated as

$$10 \quad \sigma_{c,\max} = \min(\sigma_{\text{mat}}, \sigma_{\text{buck,loc}}), \quad (2)$$

11  
12  
13 368 i.e. the lesser of the stress to cause material crushing ( $\sigma_{\text{mat}}$ ) and local buckling ( $\sigma_{\text{buck,loc}}$ ).

14  
15 369 The material crushing limit in Eq. (2) was taken as the characteristic (lower-5th-percentile)  
16 370 compressive strength ( $\sigma_{\text{mat}} = f_c'$ ). The characteristic strength was estimated to be 0.62 MPa,  
17 371 based on the assumption that it follows a lognormal distribution with mean = 0.87 MPa (Table  
18 372 1) and CoV = 20%.

19  
20  
21 373 The capacity of each of the three section types to withstand local buckling was determined  
22 374 using the finite-element analysis package ABAQUS. The model analysed for each type of  
23 375 printed section was built using shell elements and comprised a full-sized wall subjected to a  
24 376 uniform compressive force at its top and bottom boundaries. The length and height of each wall  
25 377 were taken as 2 m. These dimensions were chosen by trial-and-error so as to satisfy the  
26 378 conditions of: 1) being sufficiently large not to influence the computed local-buckling  
27 379 stress, but 2) not excessive to cause global buckling. A visual examination of the resulting  
28 380 buckling mode shape was undertaken to confirm that it indeed corresponded to local buckling  
29 381 of the shell structure. A typical local-buckling shape is shown in Figure 9 and is characterised  
30 382 by the face- and web-shells deforming perpendicular to their local planes in an alternating  
31 383 pattern, while maintaining the original angle at shell junctions. The corresponding load  
32 384 capacities are summarised in the last column of Table 3 as the load per unit length of the wall  
33 385 ( $\bar{P}_{\text{buck,loc}}$ ). These capacities were computed by assigning the material properties  $E = 22.9$  MPa  
34 386 and  $\nu = 0.22$  as informed by the material tests. The local-buckling stress used in Eq (2), was  
35 387 evaluated as  $\sigma_{\text{buck,loc}} = \bar{P}_{\text{buck,loc}}/\bar{A}$ .

36  
37  
38  
39  
40  
41  
42 388  
43  
44  
45  
46  
47  
48  
49  
50  
51  
52  
53  
54  
55  
56  
57  
58  
59  
60  
61  
62  
63  
64  
65

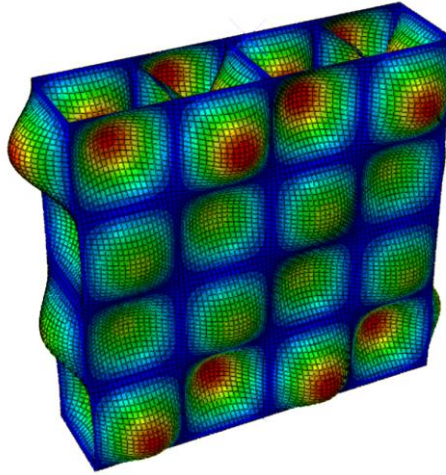


Figure 9: Visual representation of a typical local-buckling failure mode in a wall member as calculated by finite element analysis. Shown for section type A.

The member capacity of the wall was evaluated from first principles by treating it as a column under eccentric loading with potential for global buckling. In this treatment, the peak compressive stress  $\sigma_{\max}$  along on the section can be expressed as:

$$\sigma_{\max} = P \left[ \frac{1}{A} + \frac{ec}{I} \sec \left( \frac{\pi}{2} \sqrt{\frac{P}{P_{\text{buck, glob}}}} \right) \right] \quad (3)$$

where  $P$  is the applied axial load;  $e$  is the net eccentricity of the applied load (described later);  $A$  and  $I$  are the section's area and moment of inertia;  $c$  is the distance from the centreline to the extreme compressive fibre, equal to  $(d+t_{\text{in}})/2$ . The critical global buckling load of the wall,  $P_{\text{buck, glob}}$ , was obtained by Euler's formula:

$$P_{\text{buck, glob}} = \frac{\pi^2 EI}{L_e^2} \quad (4)$$

where  $L_e$  is the effective height of the wall being considered, taken as either the floor-to-floor or floor-to-roof height (indicated by  $H_w$  in Figure 9); and other properties as defined previously.

The wall's unfactored load capacity was evaluated by assigning  $\sigma_{c, \max}$  [from Eq (2)] to  $\sigma_{\max}$  in Eq (3) and solving for  $P$ . The limit-state design capacity was obtained by applying the capacity-reduction factor  $\phi = 0.5$  as per AS3700 [45], such that:

$$\phi N_c = \phi P . \quad (5)$$

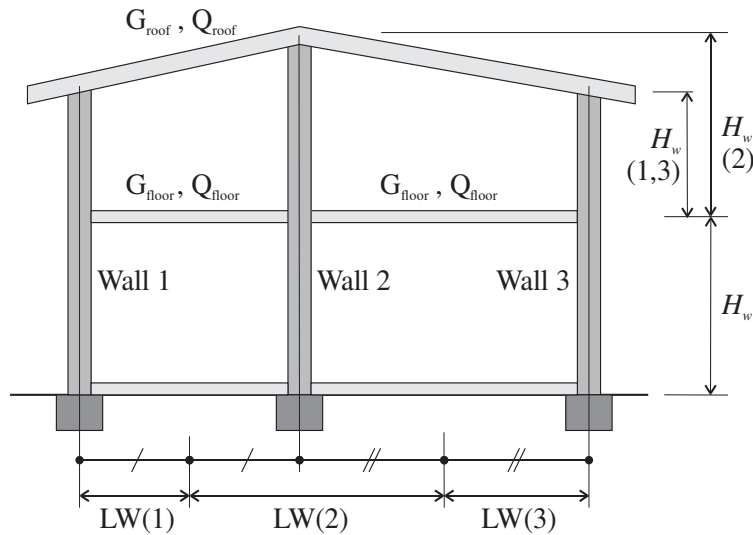
#### 4.1.4 Modelling an idealised low-rise building

To examine the feasibility of using 3DP cob walls as loadbearing structural elements, the study considered an idealised 1- and 2-storey house. Schematic representations of the building's geometry are shown in Figure 10. In the case of a 1-storey house, the walls carry only the roof load, while in the 2-storey house they carry loads from the roof and suspended floor. In each

408 scenario, the total compressive force acting on the wall also incorporates self-weight calculated  
 409 at the ground level.

410 The forces imparted to the wall by the roof and the floor depend on their respective dead load  
 411 (self-weight plus superimposed permanent load), live load, and span. The roof and floor are  
 412 treated as one-way-spanning, so the load that they apply to the wall can be calculated as the  
 413 total pressure load multiplied by a tributary width ( $L_{trib}$ ). The tributary width depends on the  
 414 configuration of the wall within building. In the case of an external wall, it is equivalent to half  
 415 the span of the floor/roof beam [LW(1) or (3) in Figure 10]. For an internal wall, it includes  
 416 the sum of the contributions from each side [LW(2) in Figure 10]. Further, if the wall contains  
 417 an opening, a simplistic treatment can be to scale the tributary width pro-rata depending on the  
 418 proportion of solid wall to openings. For instance, if half of the wall is perforated by openings,  
 419 then the tributary width becomes twice what it would be if the wall were solid.

420



421  
 422  
 423  
 424  
 425  
 426  
 427  
 428  
 429  
 430  
 431  
 432  
 433  
 434  
 435  
 436  
 437  
 438  
 439  
 440  
 441  
 442  
 443  
 444  
 445  
 446  
 447  
 448  
 449  
 450  
 451  
 452  
 453  
 454  
 455  
 456  
 457  
 458  
 459  
 460  
 461  
 462  
 463  
 464  
 465

Figure 10: Overall building geometry, Two-storey ( $n_s = 2$ ) double-bay building with internal and external walls, indicating the definition of wall height ( $H_w$ ) and tributary width (denoted here as  $LW$ ).

422 The gravity loads used in the analysis are representative of residential construction as  
 423 prescribed by loading standards (e.g. [45]). The adopted unfactored loads are summarised in  
 424 Table 4. The total dead load of the suspended floor is taken as 1.0 kPa, which allows for a  
 425 timber joist plus timber deck floor (typically 0.5 kPa) in addition to a superimposed permanent  
 426 load (0.5 kPa). The floor live load is taken as 1.5 kPa allowing for general residential  
 427 occupancy. The dead load of the roof is taken as 0.9 kPa, making allowance for timber framing  
 428 (rafters + purlins) with clay roof tiles. The live load on the roof is taken as 0.25 kPa.

429 The self-weight of the wall was calculated based on its section area, taking the weight density  
 430 of the material as  $18 \text{ kN/m}^3$ . Thus, the total design compressive load was evaluated as:

$$N_c^* = \begin{cases} P_{roof}^* + P_{wall}^* & \dots 1 \text{ storey} \\ P_{roof}^* + P_{floor}^* + 2P_{wall}^* & \dots 2 \text{ storey} \end{cases} \quad (6)$$

where  $P^*_{\text{roof}}$  is the load applied by the roof,  $P^*_{\text{floor}}$  by the suspended floor, and  $P^*_{\text{wall}}$  is the self-weight of the wall over a single storey height  $H_w$ . Each  $P^*$  is taken at the ultimate limit state using the load combination  $1.2G+1.5Q$  [45], with  $G$  being the dead load and  $Q$  the live load component.

Table 4: Summary of constant inputs used in the feasibility study. Explanations are provided in the text.

Property	Value
<i>Cob material properties:</i>	
Elastic modulus, $E$	22.9 MPa
Characteristic compressive strength, $f_c'$ (See note 1)	0.62 MPa
Weight density, $\gamma$	18 kN/m <sup>3</sup>
Poisson's ratio, $\nu$	0.22
<i>Unfactored loads:</i>	
Roof dead load, $G_{\text{roof}}$	0.9 kPa
Roof live load, $Q_{\text{roof}}$	0.25 kPa
Floor dead load, $G_{\text{floor}}$	1.0 kPa
Floor live load, $Q_{\text{floor}}$	1.5 kPa
<i>Limit-state design factors:</i>	
Compressive strength capacity-reduction factor, $\phi$	0.5
Ultimate limit-state design load combination	$1.2G + 1.5Q$
<i>Eccentricities (e) of applied load (w.r.t. wall centreline): (See note 2)</i>	
Load from roof	$0.1 \times D_{\text{out}}$
Load from floor	$0.25 \times D_{\text{out}}$
Self-weight of wall	$0.05 \times D_{\text{out}}$

Notes:

1. Determined from mean strength  $f_{cm} = 0.87$  MPa by assuming lognormal distribution and  $\text{CoV} = 20\%$ .
2. Where  $D_{\text{out}}$  is the full depth of the wall section measured between its outer edges (Figure 8).

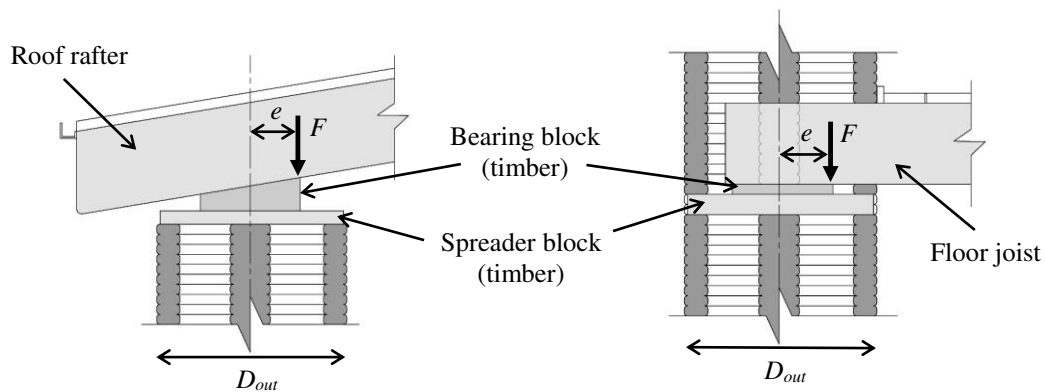
#### 4.1.5 Connection details and load eccentricity

It is important to consider that the floor and roof generally apply the load eccentrically with respect to the wall's centreline, and this generates an out-of-plane bending moment that can have a major influence on the wall's load-carrying capacity. The eccentricity of the applied load is controlled by the connection detail. While the development of the connection details



falls into the domain of detailed structural design and is outside the focus of this work, conceptual illustrations of the assumed connections are shown in Figure 11.

The connection between the roof and wall can be achieved by supporting the timber rafters using a timber bearing block, in turn resting on a spreader block that distributes the load onto the wall (Figure 11a). This detail is assumed to generate an eccentricity  $e = 0.1 D_{out}$ , with  $D_{out}$  as defined in Figure 8. The assumed wall-to-floor connection involves partial penetration of the joists into the wall and are supported by a bearing block and spreader block (Figure 11b), which is assumed to produce an eccentricity of  $0.25 D_{out}$ . It should be noted that a connection in which the floor is supported outside the extent of the wall is not advised, as it would generate an eccentricity  $> 0.5 D_{out}$  and significantly diminish the loadbearing capacity. The aforementioned values of the assumed eccentricities are consistent with similar details for conventional clay brick masonry provided in AS3700 [46].



(a) Wall-to-roof connection (section view). (b) Wall-to-floor connection (section view).

Figure 11: Potential connection details and definition of eccentricities ( $e$ ) of the applied load ( $F$ ).

Additionally, for sake of conservatism the self-weight of the wall is assumed to act at an eccentricity of  $0.05 D_{out}$  to allow for any incidental geometric imperfection of the wall. The internal bending moment was calculated as the sum of each applied load  $P^*$  (i.e.  $P^*_{roof}$ ,  $P^*_{floor}$ ,  $P^*_{wall}$ ) and its respective eccentricity, which dividing by the total compressive force  $N^*_c$  [from Eq. (6)] produces the net eccentricity:

$$e_{net} = \frac{\sum P_i^* e_i}{N_c^*} \quad (5)$$

The net eccentricity was used as the input value of  $e$  in Eq (3).

#### 4.1.6 Optimisation of wall cross section geometry

The geometry of the 3D-printed sections in Figure 7 can be defined by two variables: the nominal wall depth ( $d$ ) and average shell thickness ( $t$ ). To characterise the most efficient section to fulfil a loadbearing function, an optimisation process was undertaken that minimises the material volume while ensuring that the load capacity remains sufficient to accommodate the

467 applied design load. As a metric of the structural adequacy, the limit-state design formula [Eq  
468 (1)] can be rearranged and expressed as the capacity utilisation ( $u$ ), i.e. the ratio of the design  
469 load to the design capacity:

$$u = \frac{N_c^*(t, d)}{\phi N_c(t, d)} \quad (5)$$

470 where both the capacity and design load are functions of the optimisation variables  $d$  and  $t$ .

471 As a proxy for the material volume, we can adopt the area per unit length of the wall ( $\bar{A}$ ), since  
472 the two are directly proportional. Therefore, the optimisation process to determine the optimal  
473  $t$  and  $d$  can be expressed as:

474 Minimise  $\bar{A}$ , by varying  $t$  and  $d$ , subject to the constraints:

- 475 a.  $u \leq 1$  (to ensure structural adequacy),
- 476 b.  $t > 0, d > 0$  (positive values only),
- 477 c.  $d \geq t$  (in valid sections the shell thickness must not exceed the effective depth).

478 To cater for varying architectural requirements on the building geometry, this optimisation was  
479 performed at different combinations of the wall height ( $H_w$ ), tributary width ( $L_{trib}$ ), and number  
480 of storeys ( $n_s$ ). Constant inputs and their values are summarised in Table 4.

481 The optimisation problem was solved using two different methods in order to provide a means  
482 of cross-verifying the results and to examine alternate approaches to the representation of  
483 results. The first approach used a continuous optimiser in MATLAB, in which  $t$  and  $d$  can adopt  
484 any values along a continuous domain. The second approach used the evolutionary optimiser  
485 Galapagos in the Rhino-Grasshopper package [47] (Figure 12). The continuous-optimisation  
486 algorithm in MATLAB is the computationally faster of the two approaches; yet, implementing  
487 the optimisation in Grasshopper provides certain advantages, such as:

- 488 1) Direct link to the 3DP system (i.e. 3D printers and robotic arms), providing the ability to  
489 interface the design software with the printing tools.
- 490 2) Inclusive control over the design-to-fabrication framework, incorporating design of the  
491 geometry and other performance objectives such as thermal, lighting and environmental  
492 impacts.
- 493 3) The ability to provide visual representation of the modelling results in real time, including  
494 the building geometry and its aesthetics (Figure 13).

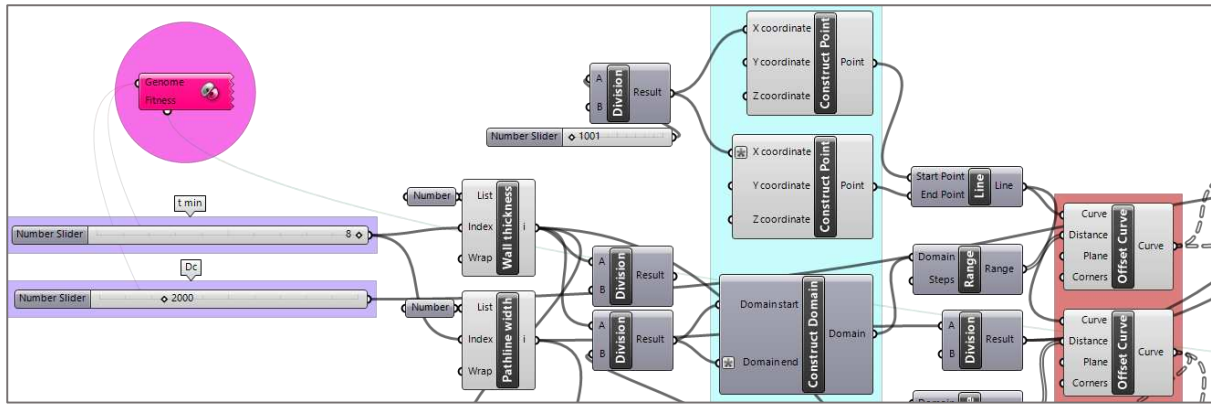


Figure 12: Part of the Grasshopper definition for the optimisation of the wall models.

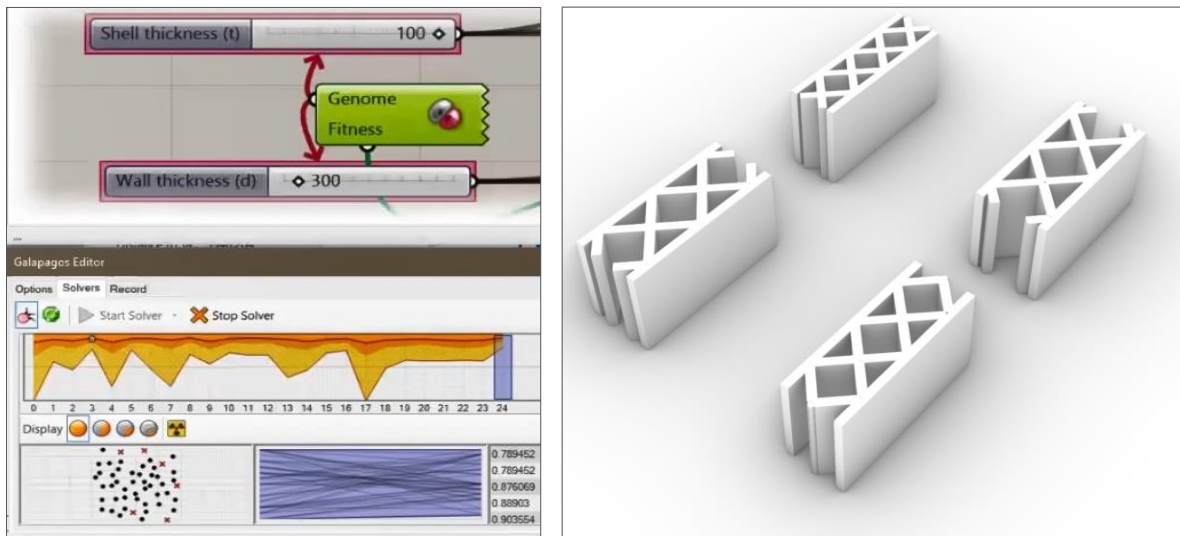


Figure 13: Visual representation of the optimisation process of Galapagos (left) and a sample of the visual generation of results for wall type C in Grasshopper (right).

## 4.2 Results and discussion

### 4.2.1 Single-scenario analysis

The typical relationship between structural adequacy versus the wall section geometry is illustrated in Figure 14, which plots contour lines of constant utilisation ( $u$ ) as a function of shell thickness ( $t$ ) and nominal wall depth ( $d$ ). The graph corresponds to a single scenario where  $H_w = 2.5$  m,  $L_{trib} = 3.5$  m, and  $n_s = 2$ ; however, the general trends are representative regardless of the selected values of these inputs. The thick black contour line corresponding to  $u=1$  represents sections whose capacity exactly matches the design load. Thus, the grey-shaded area above  $u=1$  encompasses sections that are structurally adequate. The red dashed line delineates the zones where the section is compact (governed by the material crushing) as opposed to slender (governed by local buckling), as per Eq (2). The black dashed lines bound the range of  $t$  values that correspond to available nozzle sizes in the 3DP system used in the present experimental study.

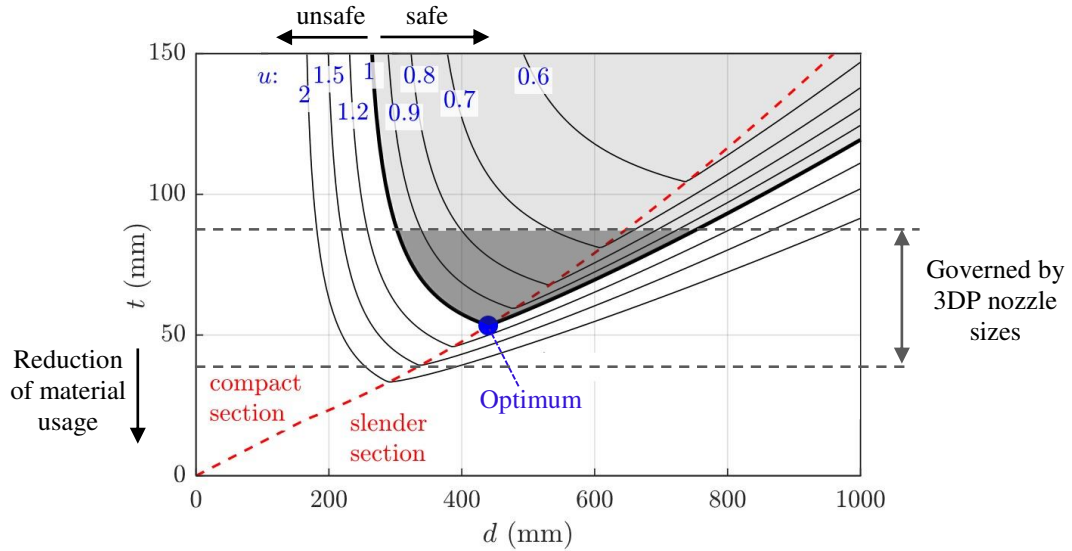


Figure 14: Typical utilisation-contour plot for varied shell thickness ( $t$ ) and nominal wall depth ( $d$ ). Shaded grey area indicates the zone where the wall's capacity is adequate for the design load. The dashed red line delineates compact sections (material stress failure) from slender sections (local-buckling failure). In this example:  $H_w = 2.5\text{m}$ ,  $L_{trib} = 3.5\text{m}$ ,  $n_s = 2$ .

For any of the printed patterns (A, B, C) the area-per-unit-length is approximately proportional to shell thickness (i.e.  $t \propto \bar{A}$ ), thus allowing the shell thickness to be used as a proxy for material consumption. Therefore, in the graphical representation in Figure 14, the optimal section occurs at the trough of the  $u=1$  contour line where  $t$  is minimised. Notably, the  $u$  contours follow different trajectories in the compact- and slender-section zones, and the optimal solution always occurs at the boundary that delineates them. In the compact-section zone, there is a roughly inverse relationship between  $t$  and  $d$ ; this is because a section with a reduced depth requires a thicker shell to maintain the necessary section area and moment of inertia. In the slender-section zone the capacity is governed by local buckling of the shell, and hence increasing the section depth requires an increase to the shell thickness to maintain a constant capacity. The existence of an optimal section also demonstrates that hollow 3DP sections offer improved material efficiency compared to equivalent solid sections. These observations also highlight that in the practical range of interest, the design capacity of the wall is governed both by the material's compressive strength and elastic modulus, underscoring the importance of both these properties.

#### 4.2.2 Design charts based on experimentally quantified material properties

The loadbearing capability of 3DP cob walls is examined in Figure 15 and Figure 16 by presenting model design charts for varied tributary width and wall height respectively. The figures plot the smallest required shell thickness ( $t$ ) and accompanying wall thickness ( $d$ ) of the optimised wall section that minimises material consumption. The constant inputs used to generate these figures are summarised in Table 4 and include the material properties established in Section 3. Figure 15 maintains a constant wall height of 3.0 m while varying the tributary width up to a maximum of 6 m. Conversely, Figure 16 maintains a constant tributary width at

4.0 m while varying the wall height between 2.5 to 3.5 m. These ranges of dimensions were selected to reflect the practical bounds of interest in a typical residential building. Each figure considers separately the alternate printed patterns (A, B, C) in either a 1- or 2-storey building. The relative efficiency of the alternate sections is presented in Figure 17 and Figure 18 by plotting the section area per unit length (a proxy for the material consumption).

Overall, the plots demonstrate that, on the assumption of the mechanical properties matching those established in the accompanying tests, loadbearing structural function in typical residential construction can be accomplished using wall section sizes that are reasonable and within the capability of the 3D printer system. The indicative range of shell thickness and wall thickness is summarised in Table 5. It is seen that in a single-storey house the section size can be kept small ( $t = 25\text{--}40\text{ mm}$ ,  $d = 250\text{--}400\text{ mm}$ ) relative to a 2-storey house ( $t = 35\text{--}120\text{ mm}$ ,  $d = 320\text{--}800\text{ mm}$ ).

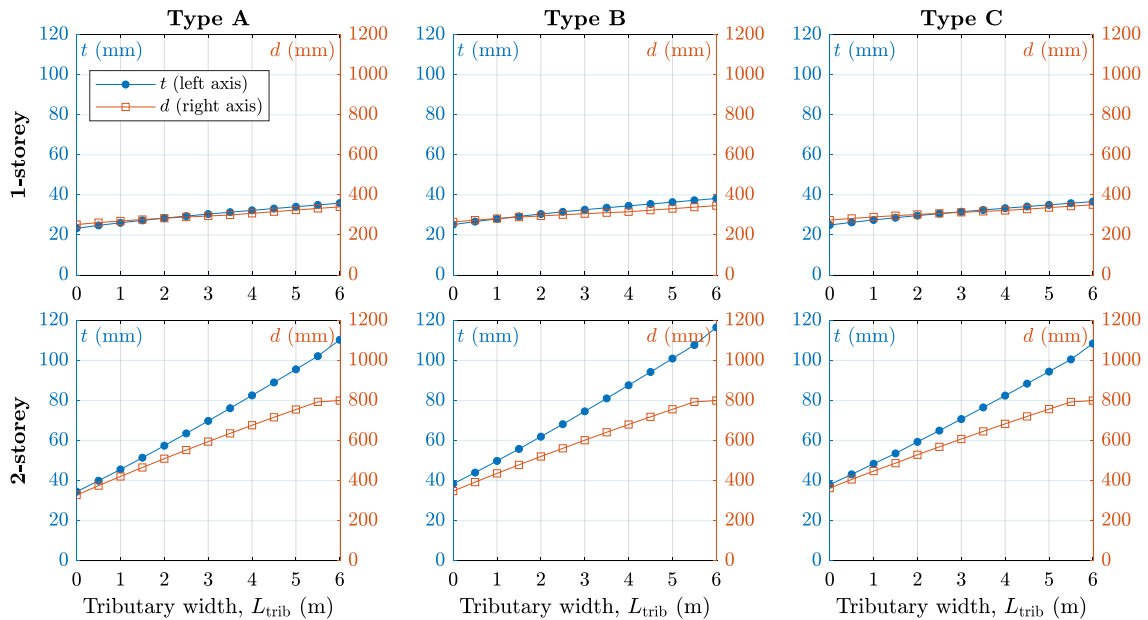


Figure 15: Dimensions  $t$  and  $d$  of optimised sections for varied tributary width (constant wall height of 3 m). All inputs including material properties are as per Table 4. Considers section types A, B, C, and either a 1- or 2-storey building. Each plot shows  $t$  on the left y-axis and  $d$  on the right y-axis.



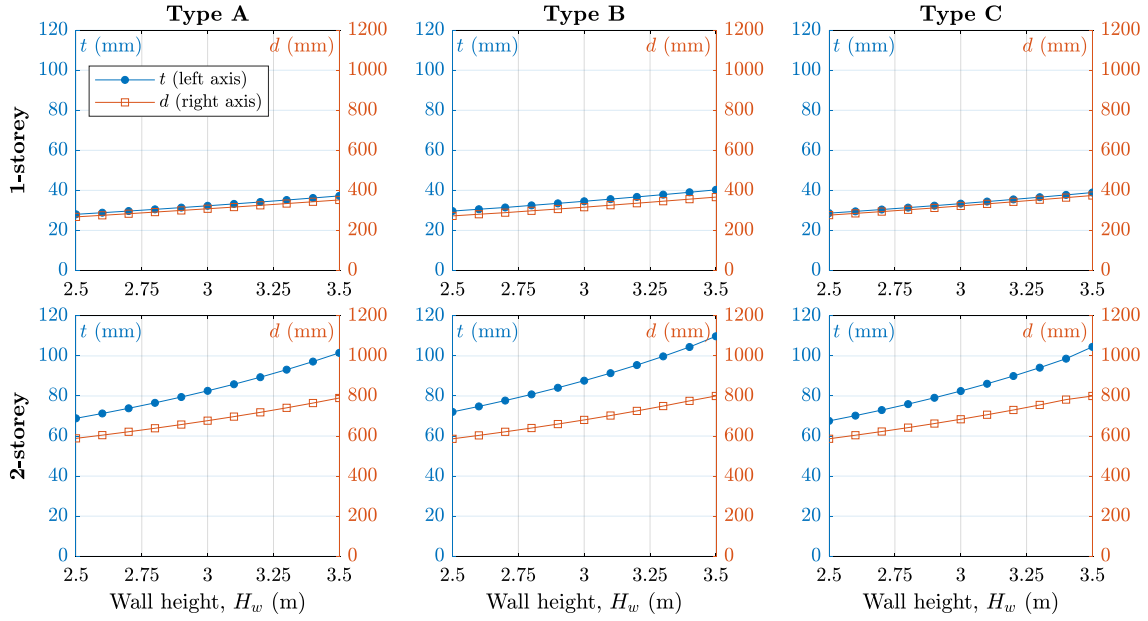


Figure 16: Dimensions  $t$  and  $d$  of optimised sections for varied wall height (constant tributary width of 4 m). All inputs including material properties are as per Table 4. Considers section types A, B, C, and either a 1- or 2-storey building. Each plot shows  $t$  on the left y-axis and  $d$  on the right y-axis.

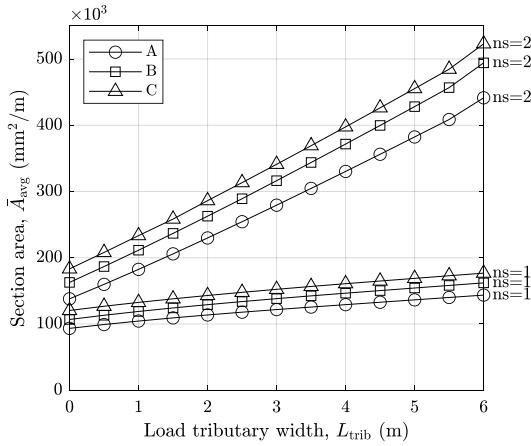


Figure 17: Section area per unit length for the optimised sections in Figure 15.

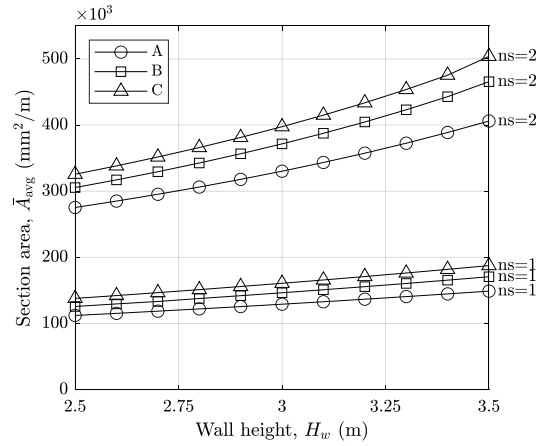


Figure 18: Section area per unit length for the optimised sections in Figure 16.

Table 5: The range of the section-defining parameters  $t$  and  $d$  corresponding to the design charts in Figure 15 and Figure 16.

	1 storey		2 stories	
	Min (mm)	Max (mm)	Min (mm)	Max (mm)
Shell thickness ( $t$ )	25	40	35	115
Wall thickness ( $d$ )	250	400	320	800

561 Note that in scenarios where a small section geometry may be permitted by structural  
562 considerations alone, the actual section could in practicality be dictated by other factors such  
563 as architectural requirements, aesthetics, thermal performance, standardisation of the  
564 construction process, and the capability of the 3D-printing system. For instance, a previous  
565 study by Gomaa et al. [21] found that 3D printing of large-scale cob walls requires a nozzle  
566 size of at least 40 mm, which can be used to generate an ‘average’ shell thickness ( $t$ ) between  
567 50–80 mm. Smaller nozzle diameters can slow down the printing process and also cause  
568 clogging of the extrusion system. On the other hand, using larger nozzles leads to reduced  
569 control over material consumption and accuracy.

570 The plots in Figure 17 and Figure 18 indicate that based solely on their structural performance,  
571 of the three section types, A is the most efficient, followed by B and then C. However, on any  
572 project it may also be necessary to consider other factors that may be impacted by the type of  
573 wall section. For example, from an architectural perspective, the notion of efficiency also  
574 includes considerations such as the design function, thermal performance, and environmental  
575 impacts. For instance, the thermal performance efficiency of 3DP cob was explored thoroughly  
576 in a recent study by Gomaa et al. [22], which demonstrated that the voids present in 3DP wall  
577 patterns dramatically improve thermal efficiency compared to solid cob walls. This means that  
578 the relative thermal performance of the alternate wall sections A, B or C may not necessarily  
579 match their relative structural performance. Hence, it is recommended that selecting the wall  
580 section type should be undertaken using a holistic approach that considers their structural,  
581 thermal, and environmental efficiency.

#### 582 4.2.3 Parametric study into the influence of the material properties

583 As demonstrated by the review of experimental studies (Table 1), the mechanical properties of  
584 cob can exhibit drastic variation depending on the mix composition. To account for the limited  
585 number of material tests in the current study, a parametric study was undertaken to examine  
586 the sensitivity of the feasibility study findings on the quality of the material. To this end, the  
587 mean compressive strength ( $f_{cm}$ ) and elastic modulus ( $E$ ) were varied so as to cover a realistic  
588 range of the respective properties as identified through the review of past testing (Table 1).

591 Three scenarios were considered (Note: Symbol ‘\*’ refers to the value being representative of  
592 the accompanying tests in Section 3):

- 593 1. Varied  $f_{cm} = 0.6/0.9^*/1.35$  MPa, at constant  $E = 23^*$  MPa,
- 594 2. Varied  $E = 20^*/40/80$  MPa, at constant  $f_{cm} = 0.87^*$  MPa,
- 595 3.  $E$  and  $f_{cm}$  both varied in equal proportion:  $[f_{cm}, E] = [0.4, 20^*]$ ,  $[0.8^*, 40]$ , and  $[1.6, 80]$   
596 MPa.

597  
598 The purpose of the first two scenarios was to gain insight into the parametric influence of the  
599 respective properties by varying them in isolation, while the third was meant to represent  
600 variation of the overall quality of the material by changing both properties simultaneously.  
601

602 The study considers wall pattern type C and varies the tributary width while keeping  $H_w = 3$   
603 m. Aside from  $f_c$  and  $E$ , the remaining inputs listed in Table 4 remain unchanged. The results  
604 are presented in Figures 19–24 respectively.

605  
606 • Scenario 1

607 The first scenario (Figures 19 and 20) looks at variation of compressive strength between  
608 0.6/0.9/1.35 MPa while maintaining  $E$  as per the current tests (23 MPa). Note that the  
609 **intermediate strength** level (0.9 MPa) is similar **to the result of** the current tests. It is observed  
610 that in the 1-storey case, the required cross section is relatively insensitive over the three levels  
611 of strength. In the 2-storey case however, the reduced strength (0.6 MPa) requires a cross  
612 section that becomes excessively large for any tributary width exceeding 1m, thus making the  
613 walls effectively incapable of performing a loadbearing function. Conversely, the improved  
614 strength (1.35 MPa) allows for a **smaller** section to be used, saving up to 30% in material  
615 volume.

616  
617 • Scenario 2

618 The second scenario (Figures 21 and 22) looks at variation of the elastic modulus at levels of  
619 20/40/80 MPa while maintaining  $f_{cm}$  as per the current tests (0.87 MPa). The lowest  $E$  value  
620 (i.e. 20 MPa) is comparable to the material of the current tests. For both the 1- and 2-storey  
621 cases, a higher elastic modulus leads to a reduction in the necessary cross section size. The  
622 improvement in increasing  $E$  from 20 to 80 MPa results in a material saving between 10–50%.  
623 It is also interesting to note that a higher elastic modulus results in an optimal cross section that  
624 has an increased wall thickness ( $d$ ) while having a lower shell thickness ( $t$ ); this can be  
625 explained by improved resistance to local buckling.

626  
627 • Scenario 3

628 The last scenario (Figures 23 and 24) examines the effect of proportionally increasing both  $f_{cm}$   
629 and  $E$ , which can be considered analogous to an overall variation in the quality of the material,  
630 i.e. low (0.4/40MPa), intermediate (0.8/40MPa) and high (1.6/80MPa) quality. The graphs  
631 indicate a strong dependence between the loadbearing capacity (i.e. required section size) and  
632 the input material properties in both the 1- and 2-storey cases. While not being directly  
633 comparable to the previous two scenarios because of different input values, a general  
634 comparison indicates that the most efficient improvement in overall loadbearing performance  
635 is achieved by simultaneously enhancing both  $f_{cm}$  and  $E$ , rather than by increasing either of  
636 these properties alone.

637  
638 Overall, the sensitivity study indicates that the feasibility of cob walls to act as loadbearing is  
639 conditional on a minimum required level of material performance. The 3DP cob tested in this  
640 study meets this threshold, but it is evident that a reduced compressive strength ( $< 0.75$  MPa)  
641 may not be sufficient for loadbearing walls in a 2-storey house. On the other hand, even weak  
642 cob ( $\approx 0.4$  MPa) may still be sufficient to construct loadbearing walls in a single-storey house.

644

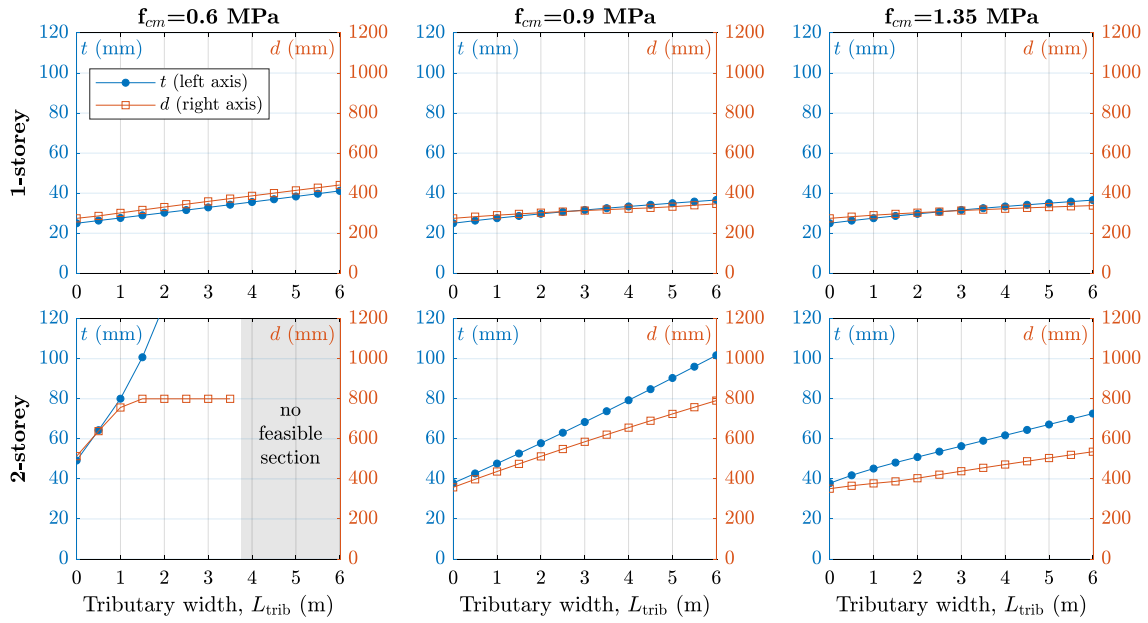


Figure 19: Dimensions  $t$  and  $d$  of optimised sections for varied compressive strength (constant  $E$ ).

645

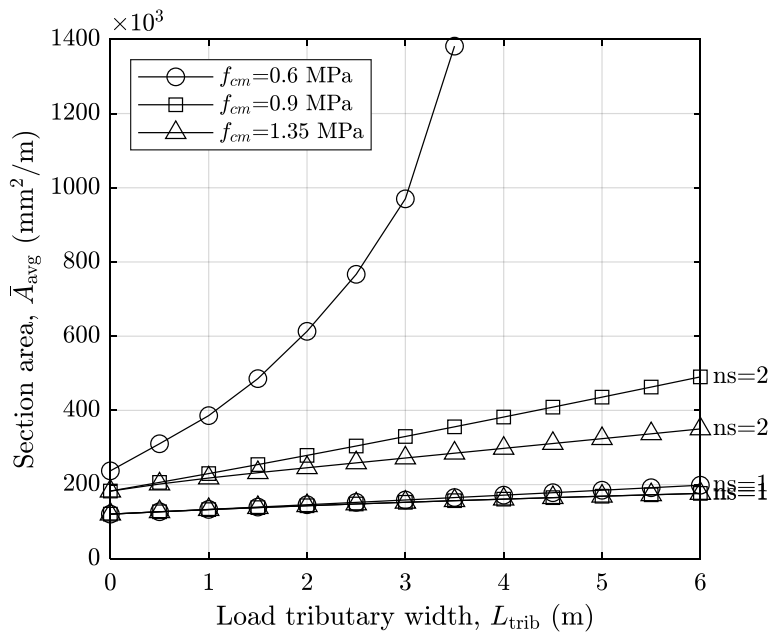


Figure 20: Material consumption of the optimised sections plotted in Figure 19.

646

647

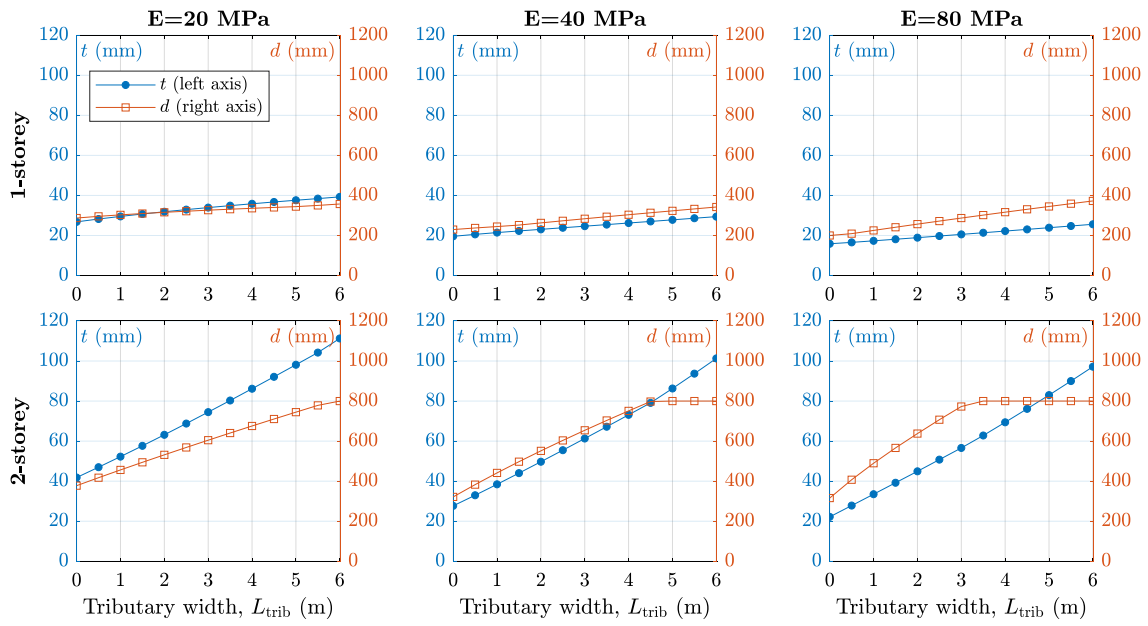


Figure 21: Dimensions  $t$  and  $d$  of optimised sections for varied elastic modulus (constant  $f_{cm}$ ).

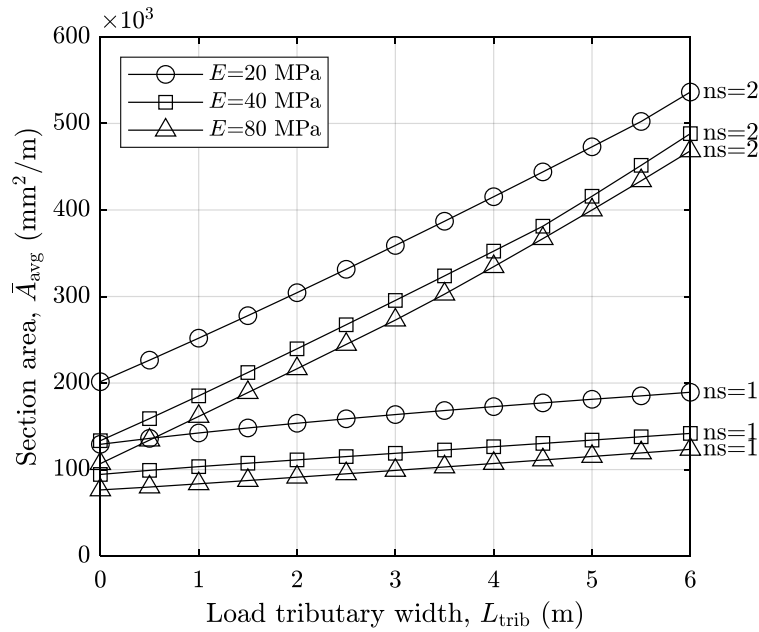


Figure 22: Material consumption of the optimised sections plotted in Figure 21.



653

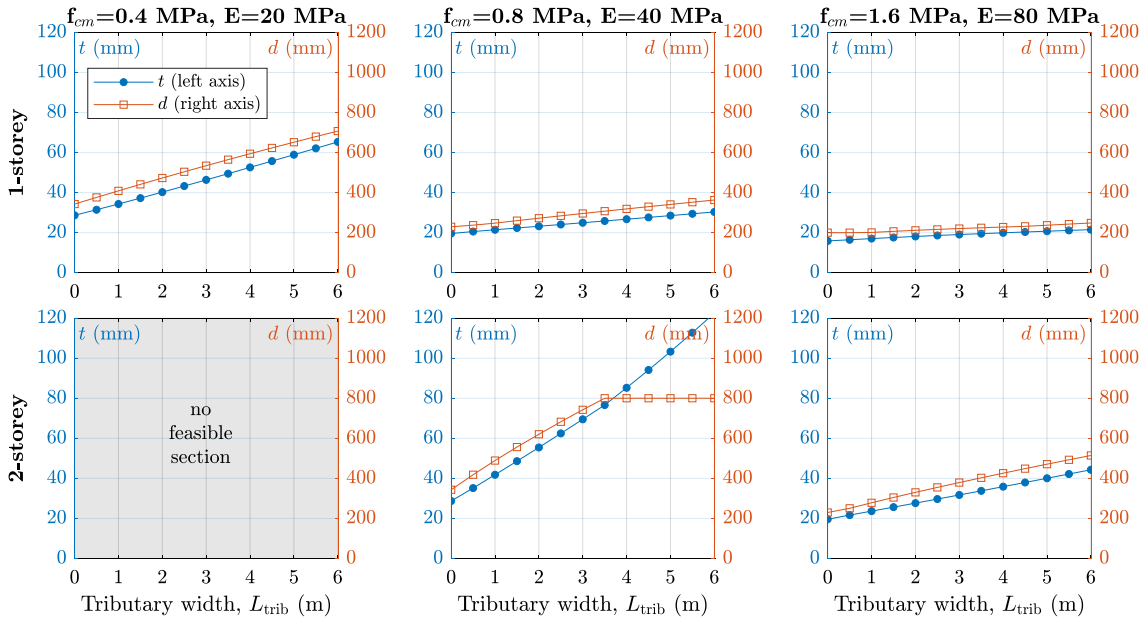


Figure 23: Dimensions  $t$  and  $d$  of optimised sections for varied  $f_{cm}$  and  $E$ , with ratio  $f_{cm}/E$  held fixed.

654

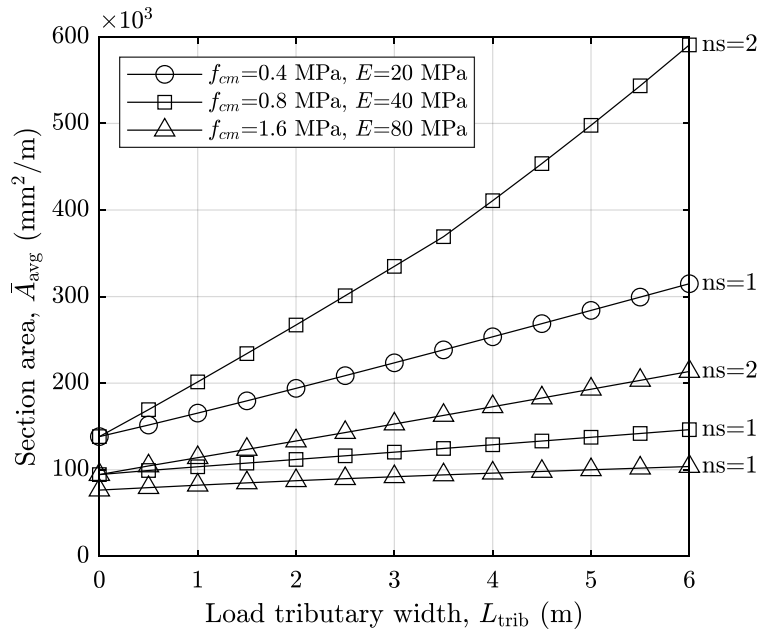


Figure 24: Material consumption of the optimised sections plotted in Figure 23.

655

656

657

658

659

## 5 Case study of a small 3DP cob house

As explained previously, the approach to leveraging the wall sizing charts (e.g. Figure 15) depends both on structural and architectural design considerations. To demonstrate the essential design process, a case study involving a small house will now be presented. The process starts with a floor plan defining the zoning and dimensions of the spaces (Figure 25). For illustrative purposes, the hypothetical house incorporates four spaces with different sizes and opening configurations, representing typical design requirements. The dimensions of the spaces range from 2m to 4 m, wall heights are set at 3m, and the number of storeys is taken as either 1 or 2. The roof (in the 1 and 2-storey cases) and the suspended floor (in the 2-storey case) are treated as one-way spanning in the directions indicated on Figure 25.

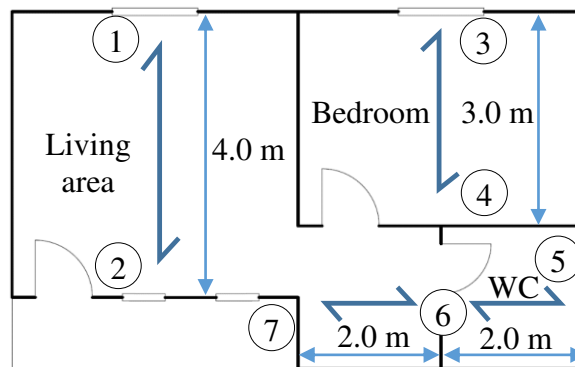


Figure 25: Basic floor plan of the idealised 3DP cob house. Half-headed arrows indicate the span direction of the suspended floor and roof. Loadbearing walls are numbered from 1 to 7.

The design parameters and final sizing of each wall are summarised in Tables 6 and 7 for the single and double storey alternatives respectively. The procedure to determine the minimum section sizes is as follows:

1. Establish which walls are loadbearing by considering the span direction of the floor/roof. In this example, walls 1–7 are loadbearing (Figure 25).
2. The ‘basic’ tributary width of each loadbearing wall is determined by considering whether the wall is internal or external and the effective span of the floor/roof being supported, using gross dimensions (refer to Figure 10).
3. If the wall has an opening, the basic tributary width is upscaled in relation to the ratio of the openings (as described in Section 4.1.4). For instance, a wall containing 50% openings (in plan view) carries an effective tributary width equal to double the basic tributary width. Note that for simplicity, the effective tributary widths in Tables 6 and 7 are rounded-up to the nearest 1m.
4. Non-loadbearing walls are analogous to having a zero effective tributary width.
5. The effective tributary width is then used to select  $t$  and  $d$  from the relevant design chart (Figure 15).

691 Note that the **nominated** section sizes in Tables 6 and 7 assume the material properties  
 692 quantified in the accompanying material tests (i.e. using Figure 15). Also note that  
 693 consideration is given here only to gravity loads and not to out-of-plane loads due to wind or  
 694 earthquake, which are region-specific and outside the scope of the current paper.

695 Figure 26 illustrates the floor plan by assigning the minimum section sizes to each wall. Since  
 696 the minimum required section size can be different for each wall, the designer has the choice  
 697 of standardising the sizes as needed to suit the other project requirements (e.g. thermal and  
 698 architectural) which may also serve to reduce the complexity of the design and improve the  
 699 efficiency of the construction process.

700

Table 6: Design of loadbearing (1–7) and non-loadbearing (NLB) walls in the 1-storey example house.

Wall	Basic $L_{trib}$ (m)	Opening ratio (%)	Tributary scale factor	Effective $L_{trib}$ (m)	Corresponding $t$ and $d$ (mm)					
					Type A		Type B		Type C	
					$t$	$d$	$t$	$d$	$t$	$d$
1	2	25	1.5	3	30	300	35	310	35	320
2	2	50	2.0	4	<b>35</b>	<b>310</b>	<b>35</b>	<b>320</b>	<b>35</b>	<b>330</b>
3	1.5	30	1.6	3	30	300	35	310	35	320
4	1.5	15	1.3	2	30	290	35	300	35	310
5	1	5	1.1	1	<b>30</b>	<b>280</b>	<b>30</b>	<b>290</b>	<b>30</b>	<b>300</b>
6	2	30	1.6	3	30	300	35	310	35	320
7	1	40	1.8	2	30	290	35	300	35	310
NLB	0	0	n/a	0	25	320	25	350	25	380

701

702

Table 7: Design of loadbearing (1–7) and non-loadbearing (NLB) walls in the 2-storey example house.

Wall	Basic $L_{trib}$ (m)	Opening ratio (%)	Tributary scale factor	Effective $L_{trib}$ (m)	Corresponding $t$ and $d$ (mm)					
					Type A		Type B		Type C	
					$t$	$d$	$t$	$d$	$t$	$d$
1	2	25	1.5	3	70	600	75	600	70	600
2	2	50	2.0	4	<b>80</b>	<b>700</b>	<b>85</b>	<b>640</b>	<b>80</b>	<b>700</b>
3	1.5	30	1.6	3	70	600	75	600	70	600
4	1.5	15	1.3	2	60	500	60	520	60	520
5	1	5	1.1	1	<b>45</b>	<b>420</b>	<b>50</b>	<b>420</b>	<b>50</b>	<b>420</b>
6	2	30	1.6	3	70	600	75	600	70	600
7	1	40	1.8	2	60	500	60	520	60	520
NLB	0	0	n/a	0	35	350	40	370	40	390

703

704

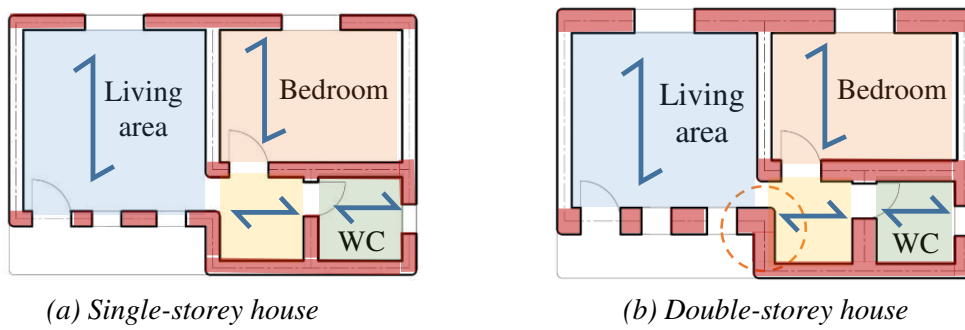


Figure 26: Floor plan showing the minimum required wall sizes walls to scale. (Shown for pattern type A for illustrative purposes)

From Table 6 and Figure 26a, it can be seen that in the case of 1-storey house, the required sections are relatively consistent across all of the walls present (in terms of  $t$  and  $d$ ), regardless of the chosen pattern (A, B, C). For example, if we consider pattern A, the required  $t$  varies between 30–35 mm, and  $d$  between 280–310 mm. The consistency in wall sizes in the case of a 1-storey building results from the required cross section being relatively insensitive to the tributary width, as reflected by Figure 15. For construction simplicity, the designer may therefore choose to standardise the wall sizes by assigning the largest required section to every wall.

In contrast to the 1-storey house, in the case of the 2-storey house the required section sizes (Table 7) vary substantially between the walls present (e.g. for type A:  $t = 45\text{--}80$  mm,  $d = 420\text{--}700$  mm). The resulting floor plan (Figure 26b) visually illustrates the difference in the wall thickness demands, especially between loadbearing and non-loadbearing walls. Therefore, in the case of the 2-storey building, the designer may opt for a suitable compromise between standardising the wall section sizes and economical material usage, for instance by adopting two or three different sizes across the building. Large wall thickness can also negatively impact the architectural functionality of the spaces, where, as highlighted in this example by the dotted circle in Figure 26b, the aisle linking the living area with the bedroom becomes severely narrowed due to the large thickness of the walls on both sides. Such considerations may require an iterative re-adjustment of the floor plan until both the structural and architectural requirements are satisfied.

An alternate way that the designer can balance the structural and architectural requirements **in relation to wall section sizes is by dictating the gravity load path by controlling**: 1) the span directivity of the floor/roof system being carried by the walls, 2) which cob walls act as loadbearing, and 3) which internal walls can be formed using lightweight partitions. To demonstrate this, Figure 27 illustrates three alternatives that maintain the same space layout as the original arrangement (Figure 25) but are reconfigured by altering the floor (or roof) spans and by implementing internal partitions to affect which walls are loadbearing.

Arrangement (a) is similar to the original configuration but rotates the floor span in south-east zone, thus allowing cob wall no. 6 (see Figure 25) to be replaced by a lightweight partition and also to reduce the size of wall no. 7. By removing some of the internal cob walls, configuration (a) arguably reduces the overall 3DP construction complexity compared to the original layout.

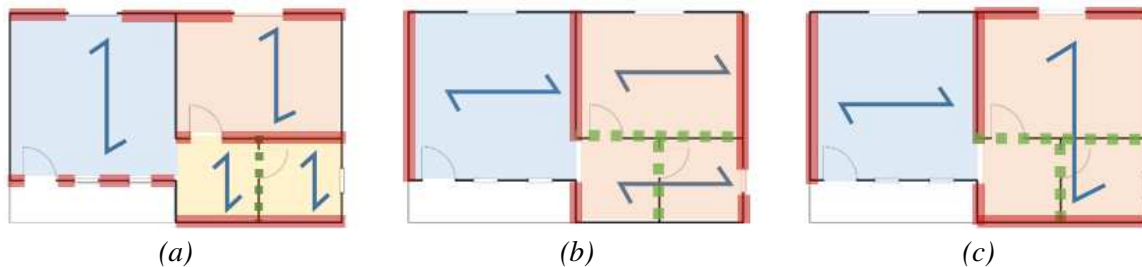
737 It does however increase the load demand on internal wall no. 4, therefore enlarging its section,  
738 and potentially hindering the functionality of the smaller rooms (i.e. toilets and lobby).

739 The presence of the internal cob wall (no. 4) in the original arrangement and configuration (a)  
740 also limits the freedom for future architectural changes to the internal space layout.  
741 Configurations (b) and (c) address this by replacing the internal walls in the east side of the  
742 house with lightweight partitions, thus improving the versatility for future layout alternations,  
743 but at the cost of requiring larger external walls because of a longer floor span in the east half  
744 out the house [compared to (a)].

745 Comparing configurations (b) and (c), a possible downside of (b) is that the central wall  
746 requires a large section since it acts as an internal loadbearing wall. By altering the direction  
747 of the floor span in the east half of the house, configuration (c) approximately halves the load  
748 on the central wall, but it does so at the cost of making the north and south outer walls  
749 loadbearing. Overall this would act to make the required wall sizes in option (c) more uniform  
750 across the house than in option (b), thus making (c) the potentially preferable option from a  
751 constructability point-of-view.

752 Overall, this example demonstrates that the process of selecting of the structural configuration  
753 is and exercise that involves compromise between a number of factors, including

- 754 • the dimensions and functionality of the spaces and location of openings,
- 755 • constructability and economical use of material,
- 756 • allowance for future alterations to the internal layout, and
- 757 • other factors not considered here, such as thermal insulation performance.



758  
759  
760  
761  
762  
763  
764  
765  
*Figure 27. Examples of alternative arrangements of the floor/roof span directivity in the example small 3DP cob house. The loadbearing walls in each instance are highlighted in red. The lightweight partitions are highlighted in green dotted lines.*

## 6 Conclusion

760 The increased uptake of 3DP technologies in construction, accompanied by a movement toward  
761 environmentally efficient materials has led to leveraging earthen materials in a contemporary  
762 3DP process. 3DP cob has been a subject of investigation for several years now; however,  
763 while those investigations have focused mostly on the architectural aspects and environmental  
764 performance, investigation into the material's feasibility to be used for load-carrying building  
765 elements has not yet been undertaken sufficiently.

766 This study has conducted a comprehensive feasibility investigation into the structural capacity  
767 of 3DP cob walls under gravity loads. This was accomplished by first quantifying the basic  
768 mechanical properties of 3DP cob using a standardised compression test. The tests  
769 demonstrated that 3DP cob appears to exhibit similar mechanical performance to conventional  
770 cob in terms of compressive strength and elastic modulus. The expected load-carrying capacity  
771 of 3DP walls was then predicted using established structural mechanics concepts and limit-  
772 state design principles. These predictions demonstrate that 3DP cob walls are expected to have  
773 sufficient capacity to act as loadbearing in residential buildings up to two storeys.

774 The feasibility study also demonstrated the following:

- 775 • Due to the favourable geometric properties of printable hollow sections, 3DP cob walls can  
776 perform a loadbearing function with more efficient material usage compared to traditional  
777 (non-3DP) solid cob walls.
- 778 • The model design approach demonstrated in this paper provides a means for integrating the  
779 structural design process of 3DP cob into the design-to-construction framework. The  
780 generated design guidelines can be directly implemented to a Rhino-Grasshopper definition  
781 that enables visual modelling and direct interfacing with the 3D-printing system.
- 782 • The range of wall section sizes (as informed by the analysis) required for loadbearing  
783 functionality in buildings up to 2-storeys can be efficiently fabricated using available 3DP  
784 technologies and extrusion systems.

785 The findings of this study complete a broader feasibility investigation of 3DP cob for modern  
786 construction which combines structural performance with three other aspects: 1) **constructability**  
787 and fabrication process, 2) **thermal** performance, and 3) life cycle assessment.  
788 The results lead to the conclusion that 3DP cob construction emerges as a strong competitor to  
789 conventional and 3DP concrete construction. 3DP cob can substitute concrete-based  
790 construction in small to medium size low-rise residential projects, especially as it provides  
791 higher environmental efficiency and rationalised energy use. It can also provide novel design  
792 opportunities in addition to higher precision compared to manually constructed cob, especially  
793 for producing complex geometries. Moreover, 3DP cob construction can provide quick  
794 sheltering solutions with low cost and efficient use of local materials in expeditionary and  
795 hostile environments.

796 It is however important to highlight that while the current study provides promising and  
797 necessary first insight into the structural feasibility of 3DP cob walls, the findings are based on  
798 structural analysis with input from small-scale material tests. Therefore, proof-of-concept  
799 structural testing on full printed wall sections is envisaged as a crucial next step of this research.

800 Furthermore, while the outcomes of this study are positive overall, the accompanying  
801 sensitivity study undertaken demonstrates that the quality of the material in terms of its  
802 mechanical properties (compression strength and elastic modulus) is highly influential on the  
803 resulting loadbearing capability of the walls. Therefore, further research into the development  
804 of 3DP-suitable cob mixtures with a focus on ensuring consistently high-quality mechanical  
805 performance could yield significant additional benefit to this form of construction.  
806 Accompanying focus into other material performance aspects, in particular shrinkage and  
807 creep, is also required.



808 **Acknowledgements**

809 We would like to acknowledge Dr Alejandro Veliz Reyes for his valuable collaboration and  
810 support (University of Plymouth). We also extend our gratitude to Aikaterini Chatzivasileiadi  
811 and Anas Lila (Cardiff University) for their invaluable help.

812 **Funding Resources**

813 This work was supported financially by the Engineering and Physical Sciences Research  
814 Council (EPSRC) and The University of Nottingham under the Network Plus: Industrial  
815 Systems in the Digital Age, Grant number: EP/P001246/1. This work is also partially supported  
816 by the University of Adelaide through the Research Abroad Scholarship scheme.

817 **References**

- 818 [1] P. Feng, X. Meng, J.-F. Chen, and L. Ye, “Mechanical properties of structures 3D  
819 printed with cementitious powders,” *Constr. Build. Mater.*, vol. 93, pp. 486–497, 2015,  
820 doi: 10.1016/j.conbuildmat.2015.05.132.
- 821 [2] A. Kazemian, X. Yuan, E. Cochran, and B. Khoshnevis, “Cementitious materials for  
822 construction-scale 3D printing: Laboratory testing of fresh printing mixture,” *Constr.*  
823 *Build. Mater.*, vol. 145, pp. 639–647, 2017, doi: 10.1016/j.conbuildmat.2017.04.015.
- 824 [3] B. Zareiyan and B. Khoshnevis, “Interlayer adhesion and strength of structures in  
825 Contour Crafting - Effects of aggregate size, extrusion rate, and layer thickness,”  
826 *Autom. Constr.*, vol. 81, pp. 112–121, 2017, doi: 10.1016/j.autcon.2017.06.013.
- 827 [4] B. Khoshnevis, “Automated construction by contour crafting — related robotics and  
828 information technologies,” vol. 13, pp. 5–19, 2004, doi: 10.1016/j.autcon.2003.08.012.
- 829 [5] T. T. Le, S. A. Austin, S. Lim, R. A. Buswell, A. G. F. Gibb, and T. Thorpe, “Mix  
830 design and fresh properties for high-performance printing concrete,” *Mater. Struct.*  
831 *Constr.*, vol. 45, pp. 1221–1232, 2012, doi: 10.1617/s11527-012-9828-z.
- 832 [6] A. Perrot, D. Rangeard, and A. Pierre, “Structural built-up of cement-based materials  
833 used for 3D- printing extrusion techniques,” *Mater. Struct.*, vol. 49, pp. 1213–1220,  
834 2016, doi: 10.1617/s11527-015-0571-0.
- 835 [7] L. Wang, H. Jiang, Z. Li, and G. Ma, “Mechanical behaviors of 3D printed lightweight  
836 concrete structure with hollow section,” *Arch. Civ. Mech. Eng.*, vol. 20, pp. 1–17, Mar.  
837 2020, doi: 10.1007/s43452-020-00017-1.
- 838 [8] H. Alhumayani, M. Gomaa, V. Soebarto, and W. Jabi, “Environmental Assessment of  
839 large-Scale 3D Printing in Construction: A Comparative Study between Cob and  
840 Concrete,” *J. Clean. Prod.*, vol. 270, pp. 122463, Jun. 2020, doi:  
841 10.1016/j.jclepro.2020.122463.
- 842 [9] CyBe, “3D Studio 2030 — CyBe Construction,” 2019. <https://cybe.eu/case/3d-studio-2030/> (accessed Nov. 20, 2019).
- 843 [10] C. Shrubsole *et al.*, “Bridging the gap: The need for a systems thinking approach in  
844 understanding and addressing energy and environmental performance in buildings,”  
845 *Indoor Built Environ.*, vol. 28, pp. 100–117, 2019, doi: 10.1177/1420326X17753513.
- 846 [11] S. Ford and M. Despeisse, “Additive manufacturing and sustainability: an exploratory  
847 study of the advantages and challenges,” *J. Clean. Prod.*, vol. 137, pp. 1573–1587,  
848 2016, doi: 10.1016/j.jclepro.2016.04.150.
- 849 [12] E. Hamard, B. Cazacliu, A. Razakamanantsoa, and J. C. Morel, “Cob, a vernacular  
850 earth construction process in the context of modern sustainable building,” *Build.*  
851 *Environ.*, vol. 106, pp. 103–119, 2016, doi: 10.1016/j.buildenv.2016.06.009.

- 853 [13] E. Quagliarini, A. Stazi, E. Pasqualini, and E. Fratolocchi, "Cob construction in Italy:  
 1 854 Some lessons from the past," *Sustainability*, vol. 2, pp. 3291–3308, 2010, doi:  
 2 855 10.3390/su2103291.
- 3 856 [14] T. Morton, F. Stevenson, B. Taylor, and N. C. Smith, "Low Cost Earth Brick  
 4 857 Construction: Monitoring & Evaluation," Fife, UK, 2005. [Online]. Available:  
 5 858 [http://www.arc-architects.com/downloads/Low-Cost-Earth-Masonry-Monitoring-](http://www.arc-architects.com/downloads/Low-Cost-Earth-Masonry-Monitoring-Evaluation-Report-2005.pdf)  
 6 859 [Evaluation-Report-2005.pdf](http://www.arc-architects.com/downloads/Low-Cost-Earth-Masonry-Monitoring-Evaluation-Report-2005.pdf).
- 7 860 [15] L. Ben-Alon, V. Loftness, K. A. Harries, and E. Cochran Hameen, "Integrating  
 8 861 Earthen Building Materials and Methods into Mainstream Construction Using  
 9 862 Environmental Performance Assessment and Building Policy," *IOP Conf. Ser. Earth*  
 10 863 *Environ. Sci.*, vol. 323, pp. 012139, 2019, doi: 10.1088/1755-1315/323/1/012139.
- 11 864 [16] O. O. Akinkulore, C. Jiang, A. T. Oyediran, O. I. Dele-Salawu, and A. K. Elensinnla,  
 12 865 "Engineering properties of Cob as a building material," *Journal of Applied Sciences*,  
 13 866 vol. 6, pp. 1882–1885, 2006, doi: 10.3923/jas.2006.1882.1885.
- 14 867 [17] J. Fordice and L. Ben-Alon, "A research project dedicated to making cob legally  
 15 868 accessible to the public," 2017.
- 16 869 [18] E. Kianfar and V. Toufigh, "Reliability analysis of rammed earth structures," *Constr.*  
 17 870 *Build. Mater.*, vol. 127, pp. 884–895, 2016, doi: 10.1016/j.conbuildmat.2016.10.052.
- 18 871 [19] A. Veliz Reyes, W. Jabi, M. Gomaa, A. Chatzivasileiadi, L. Ahmad, and N. M.  
 19 872 Wardhana, "Negotiated matter: a robotic exploration of craft-driven innovation,"  
 20 873 *Archit. Sci. Rev.*, vol. 62, pp. 1–11, 2019, doi: 10.1080/00038628.2019.1651688.
- 21 874 [20] 3D-WASP, "3D Printers | WASP | Leading Company in the 3d printing industry,"  
 22 875 2020. <https://www.3dwaspp.com/en/> (accessed Jan. 10, 2020).
- 23 876 [21] M. Gomaa, W. Jabi, A. Veliz Reyes, and V. Soebarto, "3D Printing System for Earth-  
 24 877 based construction: Case Study of Cob Walls," *Autom. Constr.*, vol. 124, pp. 103577,  
 25 878 2021, doi: <https://doi.org/10.1016/j.autcon.2021.103577>.
- 26 879 [22] M. Gomaa, J. Carfrae, S. Goodhew, W. Jabi, and A. Veliz Reyez, "Thermal  
 27 880 performance exploration of 3D printed cob," *Archit. Sci. Rev.*, vol. 62, pp. 1–8, Apr.  
 28 881 2019, doi: 10.1080/00038628.2019.1606776.
- 29 882 [23] A. Perrot, D. Rangeard, and E. Courteille, "3D printing of earth-based materials:  
 30 883 Processing aspects," *Constr. Build. Mater.*, vol. 172, pp. 670–676, 2018, doi:  
 31 884 10.1016/j.conbuildmat.2018.04.017.
- 32 885 [24] L. Keefe, *Earth building : methods and materials, repair and conservation*, 1st ed.  
 33 886 New York: Taylor and Francis Ltd., 2005.
- 34 887 [25] S. S. Damluji, *The Architecture of Yemen: From Yafi to Hadramut*. London: Laurence  
 35 888 King Publishing, 2008.
- 36 889 [26] Green Home Buildings, "Mixing and Applying Cob," 2020.  
 37 890 <http://www.greenhomebuilding.com/QandA/cob/mixing.htm> (accessed Jul. 03, 2020).
- 38 891 [27] Earth Devon, "Cob Dwellings: Compliance with The Building Regulations," *Cob*  
 39 892 *Unbaked Earth Dwellings*, vol. 2000, pp. 1–21, 2008.
- 40 893 [28] A. Weismann and K. Bryce, *Building with cob: a step-by-step guide*. Devon: Green  
 41 894 Books Ltd, 2006.
- 42 895 [29] L. Miccoli, U. Müller, and P. Fontana, "Mechanical behaviour of earthen materials: A  
 43 896 comparison between earth block masonry, rammed earth and cob," *Constr. Build.*  
 44 897 *Mater.*, vol. 61, pp. 327–339, 2014, doi: 10.1016/j.conbuildmat.2014.03.009.
- 45 898 [30] D. J. Wright, "Building From The Ground Up : Understanding and Predicting The  
 46 899 Strength of Cob , An Earthen Construction Material," The University of Tulsa. PhD  
 47 900 thesis, 2019.
- 48 901 [31] R. H. Saxton, "Performance of cob as a building material," *Struct. Eng. London*, vol.  
 49 902 73, pp. 111–115, 1995.

- 903 [32] Q. M. Pullen and T. V. Scholz, "Index and engineering properties of Oregon Cob," *J.*  
904 *Green Build.*, vol. 6, pp. 88–106, 2011, doi: 10.3992/jgb.6.2.88.
- 905 [33] E. Quagliarini and G. Maracchini, "Experimental and FEM Investigation of Cob Walls  
906 under Compression," *Adv. Civ. Eng.*, vol. 2018, pp. 21–29, 2018, doi:  
907 10.1155/2018/7027432.
- 908 [34] H. Houben and H. Guillaud, *Earth construction: a comprehensive guide*, 1st ed.  
909 London: Intermediate Technology Publications, 1994.
- 910 [35] L. Ziegert, "Konstruktion, Schäden und Sanierung, Berichte aus dem Konstruktiven  
911 Ingenieurbau," Technical University of Berlin. PhD Thesis., 2003.
- 912 [36] K. A. Coventry, "Specification Development for the Use of Devon Cob in Earthen  
913 Construction," University of Plymouth. PhD thesis, 2004.
- 914 [37] G. Minke, *Building with Earth: design and technology of a sustainable architecture*.  
915 Basel: Walter de Gruyter, 2012.
- 916 [38] M. Rizza and H. Bottger, *Effect of Straw Length and Quantity on Mechanical*  
917 *Properties of Cob*. San Francisco, 2015.
- 918 [39] G. Brunello, J. Espinoza, and A. Golitz, "Cob Property Analysis,". Dep of Civil &  
919 Environmental Engineering. Santa Clara University. MSc Thesis., 2018.
- 920 [40] T. Vincenas, E. Hamard, A. Razakamanantsoa, and F. Bendahmane, "Further  
921 development of a laboratory procedure to assess the mechanical performance of cob,"  
922 *Environ. Geotech.*, vol. 7, pp. 200–207, 2018, doi: 10.1680/jenge.17.00056.
- 923 [41] A. Jiménez Rios and D. O'Dwyer, "Experimental validation for the application of the  
924 flat jack test in cob walls," *Constr. Build. Mater.*, vol. 254, 2020, doi:  
925 10.1016/j.conbuildmat.2020.119148.
- 926 [42] A. Fabbri, J.-C. Morel, and D. Gallipoli, "Assessing the performance of earth building  
927 materials: a review of recent developments," *RILEM Tech. Lett.*, vol. 3, pp. 46–58,  
928 2018, doi: 10.21809/rilemtechlett.2018.71.
- 929 [43] S. Goodhew, P. C. Grindley, and S. D. Probeif, "Composition, Effective Thermal  
930 Conductivity And Specific Heat Of Cob Earth-walling," *Trans. Built Environ.*, vol. 15,  
931 pp. 205–213, Jan. 1995, doi: 10.2495/STR950231.
- 932 [44] CEN, "EN 772-1. Methods of test for masonry units - Part 1: Determination of  
933 compressive strength," 2011. [Online]. Available: [https://infostore.saiglobal.com/en-  
934 us/Standards/EN-772-1-2011-A1-2015-331320\\_SAIG\\_CEN\\_CEN\\_761952/](https://infostore.saiglobal.com/en-us/Standards/EN-772-1-2011-A1-2015-331320_SAIG_CEN_CEN_761952/).
- 935 [45] Standards Australia, *AS 1170.1–2002 (R2016) Structural design actions Part 1 :  
936 Permanent , imposed and other actions*. Sydney, NSW: Australian / New Zealand  
937 Standard <sup>TM</sup>, 2002.
- 938 [46] Standards Australia, *Australian Standard for Masonry structures (AS 3700:2018)*.  
939 Sydney, NSW: Australian / New Zealand Standard <sup>TM</sup>, 2018.
- 940 [47] R. McNeel, "Grasshopper - in Rhino 6," 2020.  
941 <https://www.rhino3d.com/6/new/grasshopper> (accessed Jul. 30, 2020).  
942

# Feasibility of 3DP Cob Walls Under Compression Loads in Low-Rise Construction

Mohamed Gomaa<sup>ae</sup>, Jaroslav Vaculik<sup>b,c\*</sup>, Veronica Soebarto<sup>a</sup>, Michael Griffith<sup>b,c</sup>, Wassim Jabi<sup>d</sup>

<sup>a</sup> School of Architecture and Built Environment, Horace Lamb Building, University of Adelaide, Adelaide SA5005, Australia.

<sup>b</sup> The School of Civil, Environmental and Mining Engineering, Engineering North Building, University of Adelaide, Adelaide SA5005, Australia.

<sup>c</sup> Bushfire and Natural Hazards Cooperative Research Centre, Melbourne, Australia

<sup>d</sup> The Welsh School of Architecture, Bute Building, Cardiff University, Cardiff CF10 3NB, UK.

<sup>e</sup> School of Engineering, B251- RMIT Bundoora East Campus, RMIT University, Melbourne VIC 3083, Australia.

\*Corresponding Author

Postal address: The School of Civil, Environmental and Mining Engineering, Engineering North Building, University of Adelaide, Adelaide SA5005, Australia.

Phone: (+61 8 8313 5451)

## Abstract

The rapid adoption of 3D-printing (3DP) technologies in construction, combined with an increased willingness to reduce the environmental impact of building industry, has facilitated reapproaching earth materials for modern building industry. The feasibility of 3DP earth-based materials has been under investigation in recent years, with a particular focus on cob due to its favourable characteristics toward the 3DP process. Yet, there is a lack of definitive information on the construction of 3DP cob. Hence this paper investigates the structural feasibility of 3D-printed cob walls in low-rise buildings. The investigation involved experimental compression tests on 3DP cob samples to obtain key mechanical properties including the compressive strength and elastic modulus. These properties were then used as inputs for structural analyses with respect to three alternate types of 3DP cob wall patterns to evaluate their load-carrying capacity based on a limit-state design framework. Results from the analyses were implemented in modelling an idealised low-rise cob building covering a range of floor spans and wall heights. The analytical study found that 3D-printed walls have the potential to sustain gravity loads typical of residential construction. Further, since the 3DP material was shown to have similar mechanical performance to conventional (non-3DP) cob on the material scale, the 3D-printing process provides the opportunity to produce wall sections that are structurally more efficient than the solid section used in conventional cob construction. This results in lower material consumption, making 3DP cob attractive from the point of view of resource efficiency. An important outcome of the study is the demonstration of a model design technique for low-rise 3DP cob buildings that could be implemented as part of a broader optimisation procedure to satisfy structural and architectural design objectives.

43 **Keywords:**

44 Additive manufacturing; 3D printing; Cob; Compression test; Limit-state design; Structural  
45 performance optimisation.

46 **1 Introduction**

47 Digital fabrication technologies, especially 3D printing (3DP), have been witnessing an  
48 increasing uptake in many areas of industry [1]. The construction industry has been adopting a  
49 scaled-up version of 3DP over the past two decades. The increased demand for 3DP  
50 technologies in construction industry has also encouraged researchers to develop novel ideas  
51 toward the full automation of the construction process. Several studies have proven that a well-  
52 developed digital-based process of construction offers various benefits such as larger design  
53 freedom, accelerated productivity, higher degree of customisation, and improved safety of  
54 construction personnel [2], [3].

55 Among the developed techniques of digital fabrication in construction, 3DP has been the most  
56 studied, and has seen a particular focus on cement-based materials [4]–[7]. This has led in  
57 recent years to a rapid spread of 3DP building prototypes around the world, as 3DP technology  
58 has been increasingly embraced by the construction industry [8]. Among the most notable  
59 examples are two concrete buildings constructed in 2019: One is the world’s largest 3DP  
60 building, constructed by Apis Cor in Dubai, United Arab Emirates having two storeys, a plan  
61 area of 640 m<sup>2</sup> and height of 9.5 m (Figure 1a). The second is a 80 m<sup>2</sup> prototype house built by  
62 CyBe as part of their contract with the Saudi Arabia Ministry of Housing with an ambitious  
63 goal to build 1.5 million houses using 3D concrete printing [9] (Figure 1b).



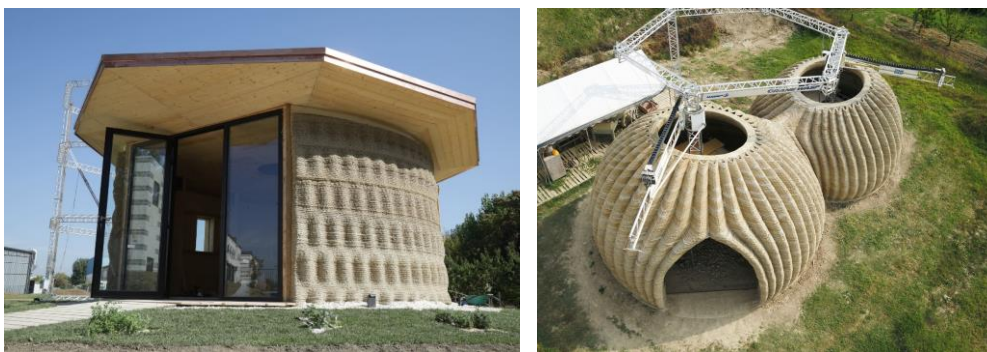
65  
66 *Figure 1: Notable examples of 3DP concrete buildings: (a) Two-storey office building in Dubai*  
67 *constructed by Apis Cor (image credit: Apis Cor), and (b) House in Saudi Arabia constructed by*  
68 *CyBe (image credit: CyBe).*

69  
70 The accelerating rate of present-day global construction is well known to produce adverse  
71 environmental impacts. Fortunately, the implementation of digital technology in construction  
72 offers great potential for sustainability [10]. For instance, according to Ford and Despeisse  
73 [11], additive manufacturing (e.g. 3D printing) in construction has several sustainability  
74 benefits such as improving efficiency of resources, extending product life, and upgrading the  
75 value and supply chains.

76 The increased motivation to harness the sustainability benefits of 3DP technology in  
77 construction has also recently renewed the interest in earthen construction materials after  
78 decades of dormancy [11],[14]. Significantly, a recent study by Hamard et al. [12] has revealed  
79 that considerable sustainability benefits can be realised through the integration of digital  
80 fabrication techniques with earth-based materials, which have low embodied energy, are highly  
81 recyclable, and generate limited waste. Furthermore, these materials typically have high  
82 material density and thus high thermal mass, which can lead to favourable thermal comfort  
83 performance, particularly in areas where there is a large difference in daytime and night-time  
84 temperatures [12], [14], [15]. As a further benefit, earth-based materials are significantly  
85 cheaper per unit volume compared to conventional building materials such as concrete or steel  
86 [13], and can under many circumstances result in more economical small-scale structures.

87 Earthen construction has three famous forms: cob, adobe, and rammed earth. Cob, which is the  
88 focus of this study, is a traditional building material comprising a mixture of subsoil, water and  
89 straw (or other fibres). It differs from adobe and rammed earth by using a wet-based  
90 construction technique that offers freedom of design while not requiring formwork. It also  
91 exhibits excellent maintenance characteristics through the ability to apply add-ons or create  
92 cuts-out, even after the cob is dry [16]–[18]. This makes cob particularly attractive for 3D  
93 printing.

94 In recent years, the performance of cob manufactured digitally using 3D printing has been the  
95 focus of emergent research at several institutions such as IAAC, Cardiff University and  
96 Plymouth University [19]. A proof of concept of the idea has also been successfully  
97 demonstrated by the 3D-printer manufacturer WASP by constructing two prototypes of cob  
98 houses [20] (Figure 2). And while the focus of the studies to date has been to examine feasibility  
99 with regard to aspects such as geometry and fabrication process [21], thermal performance  
100 [22], and life cycle assessment [8], the examination of structural performance not yet been  
101 carried out in any significant detail. As a consequence, the pursuit of fully implementing 3D  
102 cob in modern construction remains hindered by a lack of engineering guidance for structural  
103 design. Overcoming this hurdle requires establishing a reliable body of experimental test data  
104 on the mechanical (structural engineering) properties of 3DP cob, as well the development of  
105 appropriate structural design and modelling tools that can be used by design engineers.



106  
107  
108 *Figure 2: 3DP cob houses fabricated by WASP (image credit: WASP).*  
109



110 While numerous studies have focused on the mechanical properties of 3DP concrete [1][7], to  
111 the knowledge of the authors only a single study to date has investigated the mechanical  
112 properties of any 3DP cob-like material [23]. This study, by Perrot et al., tested material made  
113 from a mix of earth material and alginate seaweed biopolymer (as a substitute for straw which  
114 is traditionally used), and demonstrated compressive strength similar to that of conventional  
115 (non-3DP) cob. Besides this study, however, there is no existing research into the mechanical  
116 properties of traditional (straw-fibre) cob passed through the 3DP process. Moreover, there are,  
117 to the authors' knowledge, no existing studies involving the translation of these fundamental  
118 properties toward engineering design of 3DP cob on neither the wall nor building scale.

119 To address these gaps, this study aims to provide insight into the expected loadbearing  
120 capability 3DP cob walls. This is approached in two stages: The first conducts an experimental  
121 compression test on 3DP cob samples to obtain the basic mechanical properties including  
122 compressive strength, elastic modulus, and Poisson's ratio. The second stage evaluates the wall  
123 section geometries (dimensions) necessary to perform a loadbearing function in typical  
124 residential construction for alternate 3DP patterns through a first-principles analysis approach.  
125 This is combined with an optimisation process to examine the relationship between structural  
126 efficiency and several design variables such as variable room size, floor heights, number of  
127 storeys, and wall section properties. The outcomes are expected to empower architects and  
128 engineers with a model approach for the structural design and construction process of 3DP cob.  
129 The paper also acts as an essential part of larger overarching research by the authors on the  
130 feasibility of 3DP cob in modern construction.

131 The paper is structured as follows: Section 2 undertakes a review of previous material testing  
132 of traditional (non-3DP) cob to establish typical range of material properties. Section 3 reports  
133 original compression tests on 3DP cob cylinders. Section 4 demonstrates a simplified design  
134 approach for estimating the loadbearing capability of 3DP walls, and examines their feasibility  
135 in residential construction, including an investigation of the sensitivity on material properties.  
136 Section 5 demonstrates the essential design process on a fictional small house, and Section 6  
137 concludes with a summary and recommendations for future work.

## 2 Structural performance of cob as a building material

140 Cob buildings are well-known for their durability and resistance to weathering [24]. However,  
141 the lack of a binding agent (e.g. cement) makes the compressive strength of cob (typically < 2  
142 MPa) much weaker compared to concrete (typically > 20 MPa) and even other traditional  
143 materials such as rammed earth (typically 5–20 MPa). This combined with the fact that cob  
144 buildings were historically built without reinforcement means that building heights are  
145 typically restricted to low-rise (i.e. between one to three storeys), with most being 2-storey  
146 [13]. Some very rare but notable examples of high-rise are found however, such as the world  
147 heritage-listed towers in Yemen which have up to 9 storeys [25][26]. The low compressive  
148 strength of cob compared to other traditional materials is generally compensated for by large  
149 wall thickness [27], [28].

150 Multi-storey cob houses typically incorporate light-weight floor and roof systems in the form  
151 of timber framing. Floors usually comprise joists with wooden decking, while roofs include  
152 timber rafters plus purlins and have a typically sloped profile with extended eaves to protect  
153 walls from rain. Walls in multi-storey houses are typically around 600 mm thick, and for  
154 efficiency they are typically made thinner at upper storeys relative to the ground floor [13],  
155 [28].

156 Mechanical properties of cob are dependent on a number of factors: subsoil composition  
157 including clay content, straw and water content, degree of compaction, and the general quality  
158 of the workmanship [29], [27], [30]. Studies into the influence of the mix composition have  
159 demonstrated compressive strength to be generally enhanced by increased straw content (due  
160 to acting as local tensile reinforcement) and reduced by higher moisture content [16], [31].  
161 Table 1 provides a generalised overview of test studies to date, summarising the range of  
162 reported compressive strength ( $f_c$ ) and elastic modulus ( $E$ ). It is important to note that the cob  
163 mixtures in these studies vary in terms of their composition, with the intention of the table  
164 being to demonstrate the broad range of property values rather than parametric trends.

165 Compressive strength can be considered to be the fundamental engineering property of interest  
166 for earthen-material structures, as it controls the loadbearing capacity of walls under gravity  
167 loads [13], [32]. As demonstrated by Table 1, compressive strength usually falls between 0.4–  
168 1.35 MPa, although values less than 0.1 MPa and as high as 5 MPa have been reported. Notably,  
169 low values of strength ( $< 0.4$  MPa) are usually for mixtures with high moisture content ( $> 15\%$ )  
170 [13], [31]. Among the studies in Table 1, the range of scatter in compressive strength (where  
171 reported) varies between 2–21%. Stochastic variability has implications toward the lower-  
172 bound characteristic value that can be adopted in limit-state design as discussed later.

173 The reported elastic modulus varies drastically among the published studies. Most values fall  
174 within the range 4–200 MPa, but outlying values as low as 0.33 MPa and as high as 850 MPa  
175 have also been reported. As will be shown later (Section 4) the elastic modulus has particular  
176 importance toward the loadbearing capacity of 3DP cob walls due to the potential for local  
177 buckling of the printed sections.

178 Data on Poisson's ratio is limited to two studies [29] and [33], who reported mean values of  
179 0.15 and 0.12 respectively.

180 Additionally, cob exhibits considerably higher material ductility than rammed earth and adobe  
181 [29], [33], as characterised by the ability to maintain stress resistance into the post-peak phase  
182 of stress-strain response. Miccoli et al. [29] demonstrated this to be the case under both  
183 compressive and shear loading. The observed ductility of cob can be attributed to the influence  
184 of fibres, with fibres used in cob being typically longer than in adobe. This favourable  
185 behaviour implies that cob may be able to outperform the alternate earthen materials under  
186 deformation-controlled loading such as earthquake. While this warrants further investigation,  
187 it is outside the scope of the current paper.

188

Table 1: Compressive strength ( $f_c$ ), elastic modulus ( $E$ ), and Poisson's ratio ( $\nu$ ) for non-3DP cob. Values presented as a range (a–b) cover different cob mixtures, if applicable. Percentages in brackets denote the intra-batch CoV if specified. Unless noted otherwise, the mixtures have moisture content (mc) < 15%.

Source	$f_c$ (MPa)	$E$ (MPa)	$\nu$
Houben and Guillaud (1994) [34]	0.10	–	–
Saxton (1995) [31]	0.35–1.75 (mc<15%) 0–0.2 (mc>15%)	–	–
Ziegert (2003) [35]	0.45–1.40	170–335	–
Coventry (2004) [36]	0.48–1.24 (3%–10%)	0.33–1.25	–
Keefe (2005) [24]	0.6–1.4	–	–
Akinkurolere et al. (2006) [16]	0.6–2.2	–	–
Weismann and Bryce (2006) [28]	0.77	–	–
Quagliarini et al. (2010) [13]	0.24–0.40 (mc>15%)	4.0–40 *	–
Pullen and Scholz (2011) [32]	0.45–0.89 (22%)	11–69	–
Minke (2012) [37]	0.5–5.0	60–850	–
Miccoli et al. (2014) [29]	1.59 (2%)	651 (68%)	0.15 (4%)
Rizza and Bottger (2015) [38]	0.60 (13%)	71.5	–
Brunello et al. (2018) [39]	0.71–0.87 (8%–15%)	–	–
Quagliarini and Maracchini (2018) [33]	1.12 (5%)	16.9 (4%)	0.12 (66%)
Vincelas et al. (2018) [40]	0.50–0.76	110–350	–
Wright (2019) [30]	1.22–1.53 ** (18%–21%) 0.77–2.45 ***	–	–
Jimenez Rios and O'Dwyer (2020) [41]	0.70 (12%)	143 (23%)	–

Notes:

\*  $E$  determined from reported stress-strain curves

\*\* Specimens with varied straw content

\*\*\* Specimens with varied soil clay content

194

The only study, to the authors' knowledge, that has undertaken material testing on any 3D-printed earthen material is a recent study by Perrot et al. [23], which used a cob-like material incorporating alginate seaweed biopolymer as a substitute for straw. The produced material achieved a compressive strength between 1.2–1.8 MPa, demonstrating that 3DP earth material has the potential to achieve compressive strength toward the higher end of that for conventional non-3DP cob (Table 1).

201

### 3 Compression tests on 3D-printed cob cylinders

This section reports laboratory tests performed on 3DP-cob cylinders to quantify fundamental mechanical properties necessary for design. Among the side objectives of these tests was also to ensure that the 3D-printing process did not produce any unexpected strength reduction compared to conventional non-3DP cob (Table 1). Such a reduction could be conceivable due

207 to the altered form of the material as a result of being stacked in layers rather than being a  
208 homogeneous mass. Due to the lack of a structural testing standard specific to earthen  
209 materials, the study adopted general principles for the testing of quasi-brittle materials, as  
210 recommended by [42].

### 211 3.1 Test specimens

#### 212 3.1.1 Material mix preparation

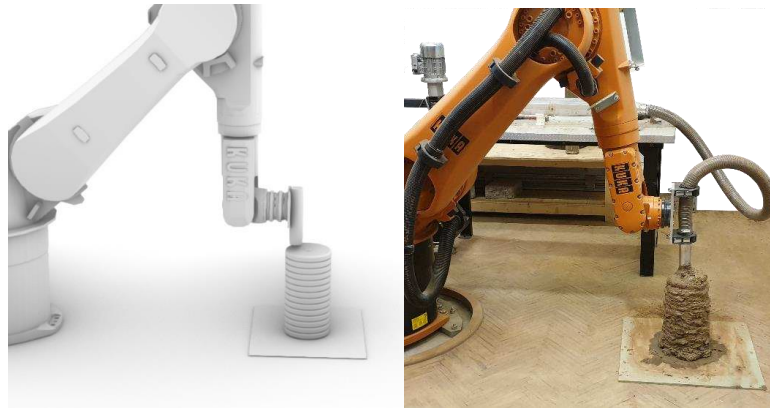
213 In the 3D-printing process, for both concrete and earth-based materials, the material must flow  
214 efficiently through the system, be deposited as layers and harden properly to reach a structural  
215 integrity threshold within an acceptable time frame that meets the construction requirements  
216 [5] [23]. The properties of the input material must therefore be formulated carefully considering  
217 both their wet (pre-hardening) and hardened states. According to Weismann and Bryce [28]  
218 and Hamard et al. [12], traditional cob mixture typically comprises 78% subsoil, 20% water  
219 and 2% fibre (straw) by weight. This however produces a nearly dry mixture with low  
220 flowability, making it unsuitable for 3D printing. To overcome this, the adopted mixture  
221 followed an alternate, 3DP-suitable, mix developed by the authors in a precursor study [22]. In  
222 the adopted mix, the water content was increased to an average of 25%, subsoil was reduced  
223 to 73%, and straw was maintained at 2% (by weight). The mixture used locally-sourced wheat  
224 straw chopped into lengths of 30–50 mm, as longer straw lengths were found to be unsuitable  
225 by causing blockage inside the extrusion system. The composition of the subsoil (sourced from  
226 Cardiff, UK) was examined using methods recommended by [28], [43] and found to contain  
227 19–20% clay and 80–81% aggregate/sand. This is in good agreement with subsoil composition  
228 recommended in the literature (15–25% clay to 75–85 % aggregate/sand) [28], [12].

229 It is worth mentioning that, despite the intentionally high moisture content of the input mixture,  
230 the moisture content of the final printed cob becomes slightly reduced by the 3DP extrusion  
231 process. This is caused by the pressurisation of the mixture inside the extrusion system, which  
232 leads to moisture release in the form of leakage around the cartridge connections. The moisture  
233 loss in this study was estimated at around 3%, leaving the printed cob at 22% moisture content.  
234 This reduction is considered favourable as it improves the structural stability of the printed  
235 layers and also reduces drying shrinkage. Note that while shrinkage is an important aspect of  
236 cob construction, it was not a specific focus of this study, especially as the observed shrinkage  
237 in the specimens was low (approx. 2%) and the specimens showed no signs of cracking during  
238 the drying period.

#### 239 3.1.2 3D-printing of specimens

240 The test specimens in this study were printed using a 6-axis KUKA KR60 HA robotic arm  
241 (Figure 3). The software package for robotic control was Rhinoceros via Grasshopper and  
242 KUKA PRC®. An electromechanical dual ram extruder, developed by the authors in a previous  
243 study [21], was used for material delivery. The test specimens comprised 400 mm-tall cob  
244 cylinders with an average diameter of 200 mm (Figure 4). Each cylinder was contoured as 14  
245 successive layers, with an average height of 29 mm per layer. The nozzle had a 45 mm  
246

248 diameter. The robotic arm moved in a circular pattern at an average movement speed of 35  
249 mm/sec.



251  
252 *Figure 3: Robotic 3D printing of the cob specimens: virtual model on Rhino (left) and the real output*  
253 *(right).*

### 254 3.2 Test arrangement and method

256 The test specimens were subjected to uniform axial load in a universal testing machine (Figure  
257 4). Prior to the test, the machine loading platens were coated with grease to minimise frictional  
258 confinement. The rate of applied load was approximately 0.08 MPa/min, with each test taking  
259 about 10 minutes to perform. The test apparatus monitored the applied load and axial  
260 (longitudinal) displacement between the two platens using a built-in linear variable differential  
261 transformer (LVDT). Due to the impracticality of applying strain gauges to the irregular surface  
262 of the specimens, horizontal deformation (necessary to evaluate the Poisson's ratio) was  
263 quantified in post-processing by digital image correlation using high-resolution video footage  
264 captured during the test. A total of three samples were tested, with examples of the failed  
265 specimens shown in Figure 5.



267  
268 *Figure 4: Compression test setup (left) and the cylindrical specimen (right).*



Figure 5: Typical examples of specimens after compressive failure.

### 3.3 Results

The observed stress-strain behaviour is shown in Figure 6. Each specimen exhibits quasi-brittle response with an approximately linear rising branch, followed by a reduction in slope up to the peak, and continued softening in the post-peak zone. The plotted stress was calculated as  $\sigma = P/A$ , where  $P$  is the applied force and  $A$  is the average cross-sectional area of the specimen ( $31,400 \text{ mm}^2$ ). Axial strain was computed as  $\epsilon_{\text{axial}} = \Delta/L$ , where  $\Delta$  is the displacement measured platen-to-platen, and  $L$  is the length of the specimen (400 mm).

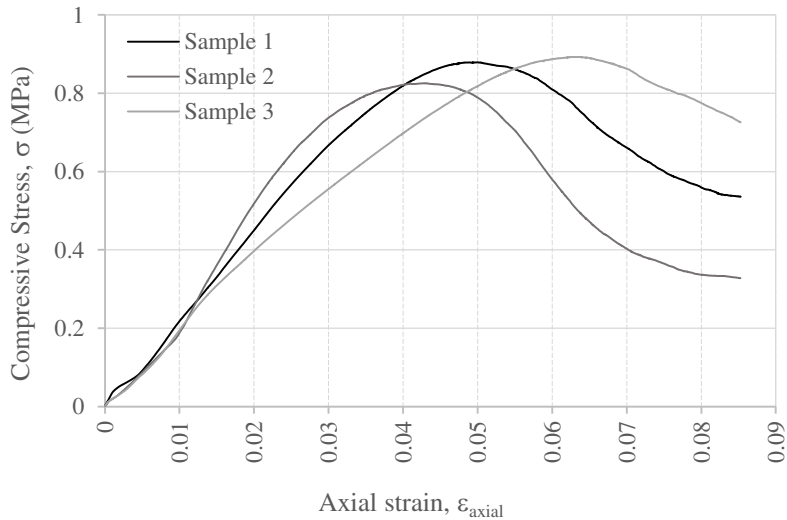


Figure 6: Stress-strain behaviour of compression test specimens.

The properties derived from the test, including the compressive strength, elastic modulus, and Poisson's ratio, are summarised in Table 2.



283 The average unconfined compressive strength ( $f_c$ ) of the specimens is 0.87 MPa. This compares  
 284 favourably to strength of non-3DP cob reported in the literature (Table 1) with most reported  
 285 values falling within 0.4–1.35 MPa. On this basis there does not appear to be any obvious  
 286 reduction in strength introduced by the 3DP process. Despite a limited number of samples, the  
 287 variability is low (CoV = 4%). It should be noted that the reported compressive strength  
 288 corresponds directly to the peak stress reached during the test. To account for the size-effect in  
 289 quasi-brittle materials as well as confinement resulting from the compression apparatus platens,  
 290 test standards typically apply a correction factor to the measured peak stress to obtain a size-  
 291 invariant unconfined compressive strength. For instance if these results were to be interpreted  
 292 according to the test standard for masonry units (EN 772-1, [44]) a correction factor of 1.25  
 293 would apply on the basis of the test specimen dimensions. However, for conservatism, the  
 294 subsequent analysis in Section 4 takes this factor as 1.

295 Elastic modulus ( $E$ ) was evaluated as the slope of the  $\sigma$ - $\epsilon$  curve along the initial rising branch  
 296 before the onset of nonlinearity. Mean  $E$  of the tested specimens is 22.9 MPa (CoV = 10%).  
 297 This falls into the lower end of values determined for non-3DP cob (Table 1) (median  $\approx$  60  
 298 MPa). As demonstrated later (Section 4), the elastic modulus is influential on wall loadbearing  
 299 strength as it controls local buckling of the printed cross section, thus providing impetus for  
 300 future investigations into 3DP-suitable cob mix design to focus on not just the material's  
 301 strength but also stiffness.

302 Poisson's ratio ( $\nu$ ) was calculated as the ratio of lateral to longitudinal strain over the initial  
 303 elastic portion of response, producing a mean value of 0.22. This is consistent with the range  
 304 of scatter reported by [29] and [33] for non-3DP cob (Table 1).

305  
 306 Table 2: Results of compression test, including unconfined compressive strength ( $f_c$ ), elastic  
 307 modulus ( $E$ ), and Poisson's ratio ( $\nu$ ).

Sample	$f_c$ (MPa)	$E$ (MPa)	$\nu$
1	0.88	22.7	0.16
2	0.83	25.3	0.28
3	0.89	20.6	0.21
Mean value	0.87	22.9	0.22
CoV	4%	10%	28%

#### 309 4 Evaluation of the feasibility of loadbearing 3DP cob walls

310 This section examines the feasibility of using 3DP cob walls as loadbearing in low-rise  
 311 residential construction. The design actions considered are from gravity loads only, and do not  
 312 include wind or earthquake loading which can be highly region-specific.

## 314 4.1 Method of structural analysis

1  
2 315 Although the expected behaviour of 3DP cob walls under gravity loads is expected to resemble  
3 316 that of walls constructed using conventional materials such as unreinforced masonry or  
4 317 concrete, the design-code provisions for these established materials are not necessarily  
5 318 translatable to 3DP cob. Therefore, the wall's load-carrying capacity was evaluated using first  
6 319 principles while adhering to the concepts of limit-state design. This includes using  
7 320 characteristic values of material stress capacity (rather than mean values), and applying factors  
8 321 to upscale design loads and downgrade the design capacity.

### 12 4.1.1 Limit-state design

13  
14 323 Capacity-adequacy checks were performed according to a limit-state design framework. With  
15 324 reference to the compressive strength, the design check can be expressed using the generalised  
16 325 form

$$19 N_c^* < \phi N_c. \quad (1)$$

20  
21 326 In Eq. (1),  $N_c^*$  is the design compressive force acting on the wall, determined as  $\gamma S$ , with  $S$   
22 327 being the unfactored working load and  $\gamma$  being the load factor (greater than 1). In turn,  $\phi N_c$  is  
23 328 the design compressive capacity of the wall, determined as the basic capacity  $N_c$  multiplied by  
24 329 the capacity-reduction factor  $\phi$  (less than 1). To account for the fact that the material stress  
25 330 capacities exhibit stochastic variability, capacity  $N_c$  was calculated using the characteristic  
26 331 compressive strength,  $f_c'$ , defined as the lower-5th-percentile value.

### 30 4.1.2 Wall cross-section patterns

31  
32 333 Three different types of printed patterns were considered as part of this feasibility study; these  
33 334 are referred to as A, B and C as shown in Figure 7. These three patterns align carefully with  
34 335 the wall sections in two previous studies that investigated thermal performance and life cycle  
35 336 assessment of 3D-printed cob by Gomaa et al. [22] and Alhumayani et al. [8] respectively. The  
36 337 criteria for choosing these wall sections are based on meeting multiple design requirements  
37 338 including adequate thermal insulation, efficient use of material, and structural integrity. A  
38 339 generic vertical cross section of a wall is shown in Figure 8. Because the 3D-printing process  
39 340 in the current study dispensed the cob material in circular cross sections while being flattened  
40 341 down into wider layers, the resulting vertical shells did not have a constant thickness (Figure  
41 342 8). Rather, the shell thickness ranged between an inner value,  $t_{in}$ , and outer value,  $t_{out}$ , as shown.  
42 343 Both  $t_{in}$  and  $t_{out}$  could be estimated according to a number of parameters in the 3D-printing  
43 344 process setup, such as the layer height, nozzle size and the extrusion rate [21]. On the basis of  
44 345 typical printed patterns,  $t_{out} - t_{in}$  was taken as 20 mm, with the average thickness ( $t$ ) being in  
45 346 turn defined as  $t = (t_{in} + t_{out})/2$ . For each section type, the nominal wall depth ( $d$ ) is defined as  
46 347 the distance between the centrelines of the two external 'face' shells; and  $a$  denotes the  
47 348 dimension between the internal 'web' shells (Figure 8). In all of the subsequent analyses,  $a$  is  
48 349 taken equal to  $d$ .

56 350

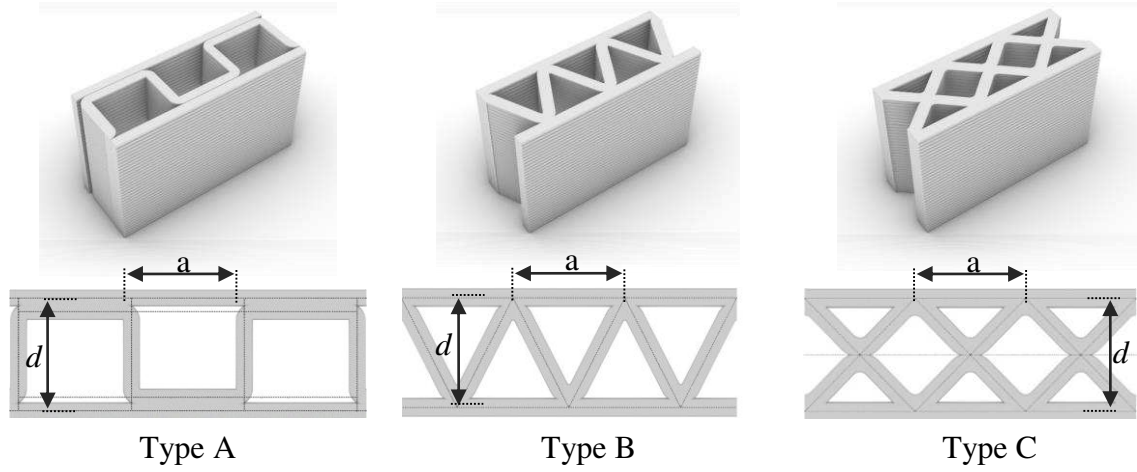


Figure 7: Alternate printed patterns considered in this study.

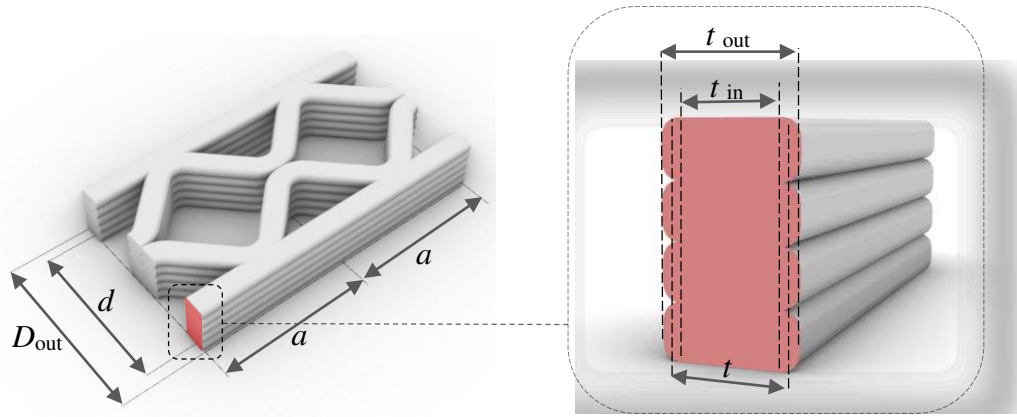


Figure 8: Definition of geometric properties along a generic cross section.

Evaluation of the wall's compressive capacity requires the wall's area ( $A$ ) and out-of-plane moment of inertia ( $I$ ). These were calculated for each type of section by conservatively taking the shell thickness as  $t_{in}$ . For comparative purposes, the sectional properties of the three pattern types are provided in Table 3.

Table 3: Section properties for the alternate printed patterns. Each considers a reference section with  $t_{in} = 50\text{mm}$  and  $d = 500\text{mm}$ . Properties accented by a bar ( $\bar{X}$ ) denote the value per unit length run of the wall.

Wall Type	$t_{in}$ (mm)	$t$ (mm)	$d$ (mm)	$\bar{A}$ (mm <sup>2</sup> /m)	$\bar{I}$ (mm <sup>4</sup> /m)	$\bar{P}_{buck,loc}$ (kN/m)
A	50	60	500	200,000	$9.32 \times 10^9$	145
B	50	60	500	212,000	$8.60 \times 10^9$	137
C	50	60	500	241,000	$9.23 \times 10^9$	181

### 4.1.3 Wall compressive strength

The compressive strength of a generic (3DP or no-3DP) cob wall requires evaluation of its member capacity under combined axial load and eccentricity moment with the potential for global buckling combined with material failure. A 3DP wall however differs from a solid wall in that the section capacity can be governed by not just material crushing, but also by local buckling of the shell structure. Thus, the compressive stress capacity of the section was evaluated as

$$\sigma_{c,\max} = \min(\sigma_{\text{mat}}, \sigma_{\text{buck,loc}}), \quad (2)$$

i.e. the lesser of the stress to cause material crushing ( $\sigma_{\text{mat}}$ ) and local buckling ( $\sigma_{\text{buck,loc}}$ ).

The material crushing limit in Eq. (2) was taken as the characteristic (lower-5th-percentile) compressive strength ( $\sigma_{\text{mat}} = f_c'$ ). The characteristic strength was estimated to be 0.62 MPa, based on the assumption that it follows a lognormal distribution with mean = 0.87 MPa (Table 1) and CoV = 20%.

The capacity of each of the three section types to withstand local buckling was determined using the finite-element analysis package ABAQUS. The model analysed for each type of printed section was built using shell elements and comprised a full-sized wall subjected to a uniform compressive force at its top and bottom boundaries. The length and height of each wall were taken as 2 m. These dimensions were chosen by trial-and-error so as to satisfy the conditions of: 1) being sufficiently large not to influence the computed local-buckling stress, but 2) not excessive to cause global buckling. A visual examination of the resulting buckling mode shape was undertaken to confirm that it indeed corresponded to local buckling of the shell structure. A typical local-buckling shape is shown in Figure 9 and is characterised by the face- and web-shells deforming perpendicular to their local planes in an alternating pattern, while maintaining the original angle at shell junctions. The corresponding load capacities are summarised in the last column of Table 3 as the load per unit length of the wall ( $\bar{P}_{\text{buck,loc}}$ ). These capacities were computed by assigning the material properties  $E = 22.9$  MPa and  $\nu = 0.22$  as informed by the material tests. The local-buckling stress used in Eq (2), was evaluated as  $\sigma_{\text{buck,loc}} = \bar{P}_{\text{buck,loc}}/\bar{A}$ .

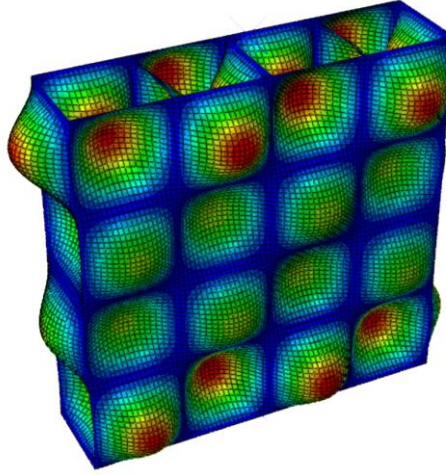


Figure 9: Visual representation of a typical local-buckling failure mode in a wall member as calculated by finite element analysis. Shown for section type A.

The member capacity of the wall was evaluated from first principles by treating it as a column under eccentric loading with potential for global buckling. In this treatment, the peak compressive stress  $\sigma_{\max}$  along on the section can be expressed as:

$$\sigma_{\max} = P \left[ \frac{1}{A} + \frac{ec}{I} \sec \left( \frac{\pi}{2} \sqrt{\frac{P}{P_{\text{buck, glob}}}} \right) \right] \quad (3)$$

where  $P$  is the applied axial load;  $e$  is the net eccentricity of the applied load (described later);  $A$  and  $I$  are the section's area and moment of inertia;  $c$  is the distance from the centreline to the extreme compressive fibre, equal to  $(d+t_{\text{in}})/2$ . The critical global buckling load of the wall,  $P_{\text{buck, glob}}$ , was obtained by Euler's formula:

$$P_{\text{buck, glob}} = \frac{\pi^2 EI}{L_e^2} \quad (4)$$

where  $L_e$  is the effective height of the wall being considered, taken as either the floor-to-floor or floor-to-roof height (indicated by  $H_w$  in Figure 9); and other properties as defined previously.

The wall's unfactored load capacity was evaluated by assigning  $\sigma_{c, \max}$  [from Eq (2)] to  $\sigma_{\max}$  in Eq (3) and solving for  $P$ . The limit-state design capacity was obtained by applying the capacity-reduction factor  $\phi = 0.5$  as per AS3700 [45], such that:

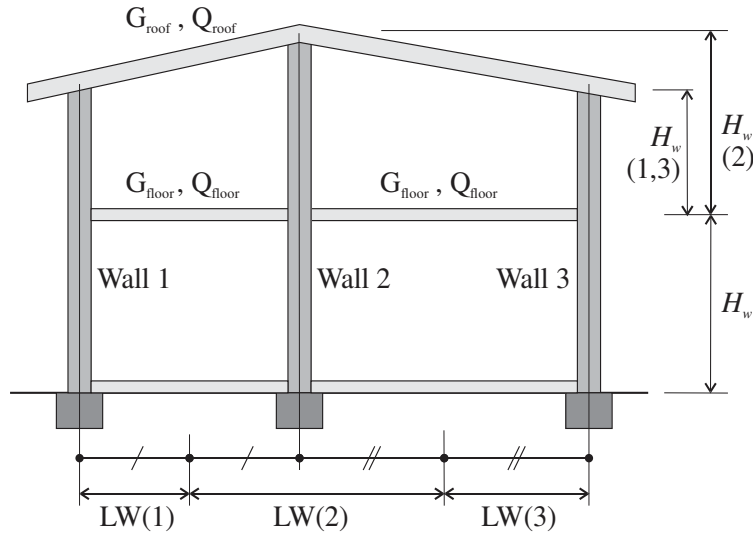
$$\phi N_c = \phi P . \quad (5)$$

#### 4.1.4 Modelling an idealised low-rise building

To examine the feasibility of using 3DP cob walls as loadbearing structural elements, the study considered an idealised 1- and 2-storey house. Schematic representations of the building's geometry are shown in Figure 10. In the case of a 1-storey house, the walls carry only the roof load, while in the 2-storey house they carry loads from the roof and suspended floor. In each

408 scenario, the total compressive force acting on the wall also incorporates self-weight calculated  
 409 at the ground level.

410 The forces imparted to the wall by the roof and the floor depend on their respective dead load  
 411 (self-weight plus superimposed permanent load), live load, and span. The roof and floor are  
 412 treated as one-way-spanning, so the load that they apply to the wall can be calculated as the  
 413 total pressure load multiplied by a tributary width ( $L_{trib}$ ). The tributary width depends on the  
 414 configuration of the wall within building. In the case of an external wall, it is equivalent to half  
 415 the span of the floor/roof beam [LW(1) or (3) in Figure 10]. For an internal wall, it includes  
 416 the sum of the contributions from each side [LW(2) in Figure 10]. Further, if the wall contains  
 417 an opening, a simplistic treatment can be to scale the tributary width pro-rata depending on the  
 418 proportion of solid wall to openings. For instance, if half of the wall is perforated by openings,  
 419 then the tributary width becomes twice what it would be if the wall were solid.



420  
 421  
 422  
 423  
 424  
 425  
 426  
 427  
 428  
 429  
 430  
 431  
 432  
 433  
 434  
 435  
 436  
 437  
 438  
 439  
 440  
 441  
 442  
 443  
 444  
 445  
 446  
 447  
 448  
 449  
 450  
 451  
 452  
 453  
 454  
 455  
 456  
 457  
 458  
 459  
 460  
 461  
 462  
 463  
 464  
 465

Figure 10: Overall building geometry, Two-storey ( $n_s = 2$ ) double-bay building with internal and external walls, indicating the definition of wall height ( $H_w$ ) and tributary width (denoted here as  $LW$ ).

422 The gravity loads used in the analysis are representative of residential construction as  
 423 prescribed by loading standards (e.g. [45]). The adopted unfactored loads are summarised in  
 424 Table 4. The total dead load of the suspended floor is taken as 1.0 kPa, which allows for a  
 425 timber joist plus timber deck floor (typically 0.5 kPa) in addition to a superimposed permanent  
 426 load (0.5 kPa). The floor live load is taken as 1.5 kPa allowing for general residential  
 427 occupancy. The dead load of the roof is taken as 0.9 kPa, making allowance for timber framing  
 428 (rafters + purlins) with clay roof tiles. The live load on the roof is taken as 0.25 kPa.

429 The self-weight of the wall was calculated based on its section area, taking the weight density  
 430 of the material as  $18 \text{ kN/m}^3$ . Thus, the total design compressive load was evaluated as:

$$N_c^* = \begin{cases} P_{roof}^* + P_{wall}^* & \dots 1 \text{ storey} \\ P_{roof}^* + P_{floor}^* + 2P_{wall}^* & \dots 2 \text{ storey} \end{cases} \quad (6)$$



where  $P^*_{\text{roof}}$  is the load applied by the roof,  $P^*_{\text{floor}}$  by the suspended floor, and  $P^*_{\text{wall}}$  is the self-weight of the wall over a single storey height  $H_w$ . Each  $P^*$  is taken at the ultimate limit state using the load combination  $1.2G+1.5Q$  [45], with  $G$  being the dead load and  $Q$  the live load component.

Table 4: Summary of constant inputs used in the feasibility study. Explanations are provided in the text.

Property	Value
<i>Cob material properties:</i>	
Elastic modulus, $E$	22.9 MPa
Characteristic compressive strength, $f_c'$ (See note 1)	0.62 MPa
Weight density, $\gamma$	18 kN/m <sup>3</sup>
Poisson's ratio, $\nu$	0.22
<i>Unfactored loads:</i>	
Roof dead load, $G_{\text{roof}}$	0.9 kPa
Roof live load, $Q_{\text{roof}}$	0.25 kPa
Floor dead load, $G_{\text{floor}}$	1.0 kPa
Floor live load, $Q_{\text{floor}}$	1.5 kPa
<i>Limit-state design factors:</i>	
Compressive strength capacity-reduction factor, $\phi$	0.5
Ultimate limit-state design load combination	$1.2G + 1.5Q$
<i>Eccentricities (e) of applied load (w.r.t. wall centreline): (See note 2)</i>	
Load from roof	$0.1 \times D_{\text{out}}$
Load from floor	$0.25 \times D_{\text{out}}$
Self-weight of wall	$0.05 \times D_{\text{out}}$

Notes:

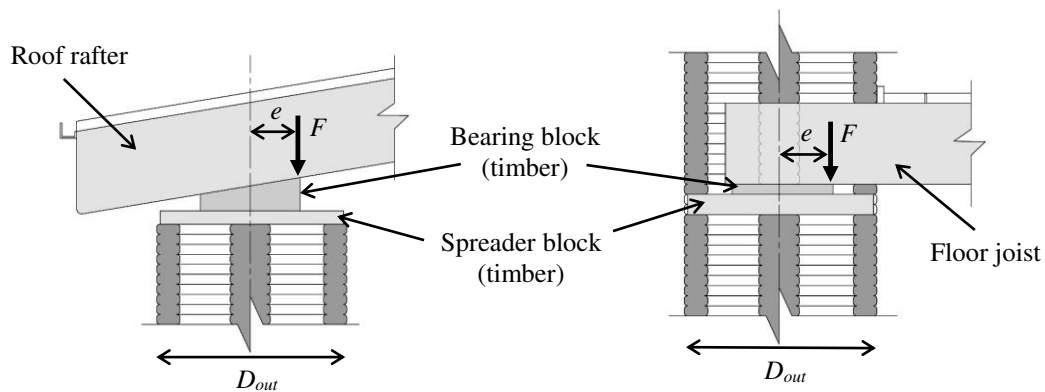
1. Determined from mean strength  $f_{cm} = 0.87$  MPa by assuming lognormal distribution and  $\text{CoV} = 20\%$ .
2. Where  $D_{\text{out}}$  is the full depth of the wall section measured between its outer edges (Figure 8).

#### 4.1.5 Connection details and load eccentricity

It is important to consider that the floor and roof generally apply the load eccentrically with respect to the wall's centreline, and this generates an out-of-plane bending moment that can have a major influence on the wall's load-carrying capacity. The eccentricity of the applied load is controlled by the connection detail. While the development of the connection details

falls into the domain of detailed structural design and is outside the focus of this work, conceptual illustrations of the assumed connections are shown in Figure 11.

The connection between the roof and wall can be achieved by supporting the timber rafters using a timber bearing block, in turn resting on a spreader block that distributes the load onto the wall (Figure 11a). This detail is assumed to generate an eccentricity  $e = 0.1 D_{out}$ , with  $D_{out}$  as defined in Figure 8. The assumed wall-to-floor connection involves partial penetration of the joists into the wall and are supported by a bearing block and spreader block (Figure 11b), which is assumed to produce an eccentricity of  $0.25 D_{out}$ . It should be noted that a connection in which the floor is supported outside the extent of the wall is not advised, as it would generate an eccentricity  $> 0.5 D_{out}$  and significantly diminish the loadbearing capacity. The aforementioned values of the assumed eccentricities are consistent with similar details for conventional clay brick masonry provided in AS3700 [46].



(a) Wall-to-roof connection (section view). (b) Wall-to-floor connection (section view).

Figure 11: Potential connection details and definition of eccentricities ( $e$ ) of the applied load ( $F$ ).

Additionally, for sake of conservatism the self-weight of the wall is assumed to act at an eccentricity of  $0.05 D_{out}$  to allow for any incidental geometric imperfection of the wall. The internal bending moment was calculated as the sum of each applied load  $P^*$  (i.e.  $P^*_{roof}$ ,  $P^*_{floor}$ ,  $P^*_{wall}$ ) and its respective eccentricity, which dividing by the total compressive force  $N^*_c$  [from Eq. (6)] produces the net eccentricity:

$$e_{net} = \frac{\sum P_i^* e_i}{N_c^*} \quad (5)$$

The net eccentricity was used as the input value of  $e$  in Eq (3).

#### 4.1.6 Optimisation of wall cross section geometry

The geometry of the 3D-printed sections in Figure 7 can be defined by two variables: the nominal wall depth ( $d$ ) and average shell thickness ( $t$ ). To characterise the most efficient section to fulfil a loadbearing function, an optimisation process was undertaken that minimises the material volume while ensuring that the load capacity remains sufficient to accommodate the

467 applied design load. As a metric of the structural adequacy, the limit-state design formula [Eq  
468 (1)] can be rearranged and expressed as the capacity utilisation ( $u$ ), i.e. the ratio of the design  
469 load to the design capacity:

$$u = \frac{N_c^*(t, d)}{\phi N_c(t, d)} \quad (5)$$

470 where both the capacity and design load are functions of the optimisation variables  $d$  and  $t$ .

471 As a proxy for the material volume, we can adopt the area per unit length of the wall ( $\bar{A}$ ), since  
472 the two are directly proportional. Therefore, the optimisation process to determine the optimal  
473  $t$  and  $d$  can be expressed as:

474 Minimise  $\bar{A}$ , by varying  $t$  and  $d$ , subject to the constraints:

- 475 a.  $u \leq 1$  (to ensure structural adequacy),
- 476 b.  $t > 0, d > 0$  (positive values only),
- 477 c.  $d \geq t$  (in valid sections the shell thickness must not exceed the effective depth).

478 To cater for varying architectural requirements on the building geometry, this optimisation was  
479 performed at different combinations of the wall height ( $H_w$ ), tributary width ( $L_{trib}$ ), and number  
480 of storeys ( $n_s$ ). Constant inputs and their values are summarised in Table 4.

481 The optimisation problem was solved using two different methods in order to provide a means  
482 of cross-verifying the results and to examine alternate approaches to the representation of  
483 results. The first approach used a continuous optimiser in MATLAB, in which  $t$  and  $d$  can adopt  
484 any values along a continuous domain. The second approach used the evolutionary optimiser  
485 Galapagos in the Rhino-Grasshopper package [47] (Figure 12). The continuous-optimisation  
486 algorithm in MATLAB is the computationally faster of the two approaches; yet, implementing  
487 the optimisation in Grasshopper provides certain advantages, such as:

- 488 1) Direct link to the 3DP system (i.e. 3D printers and robotic arms), providing the ability to  
489 interface the design software with the printing tools.
- 490 2) Inclusive control over the design-to-fabrication framework, incorporating design of the  
491 geometry and other performance objectives such as thermal, lighting and environmental  
492 impacts.
- 493 3) The ability to provide visual representation of the modelling results in real time, including  
494 the building geometry and its aesthetics (Figure 13).

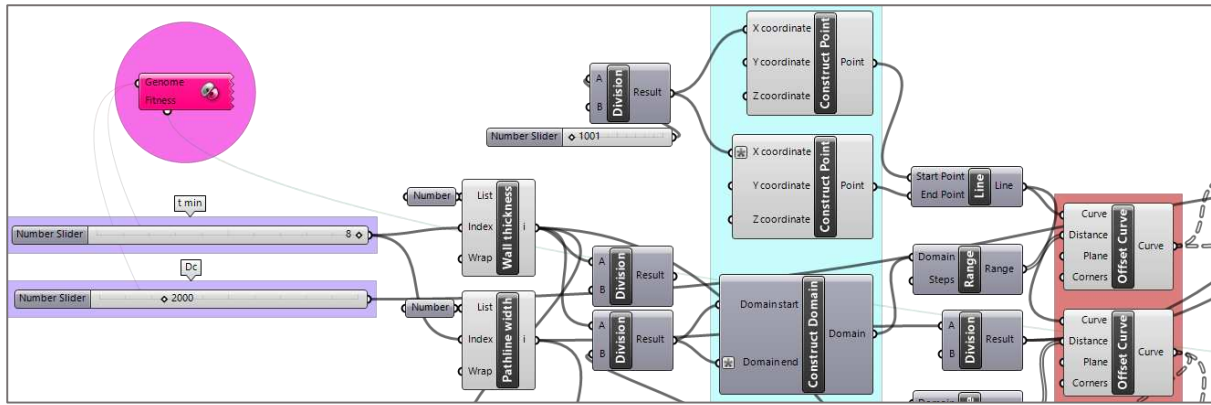


Figure 12: Part of the Grasshopper definition for the optimisation of the wall models.

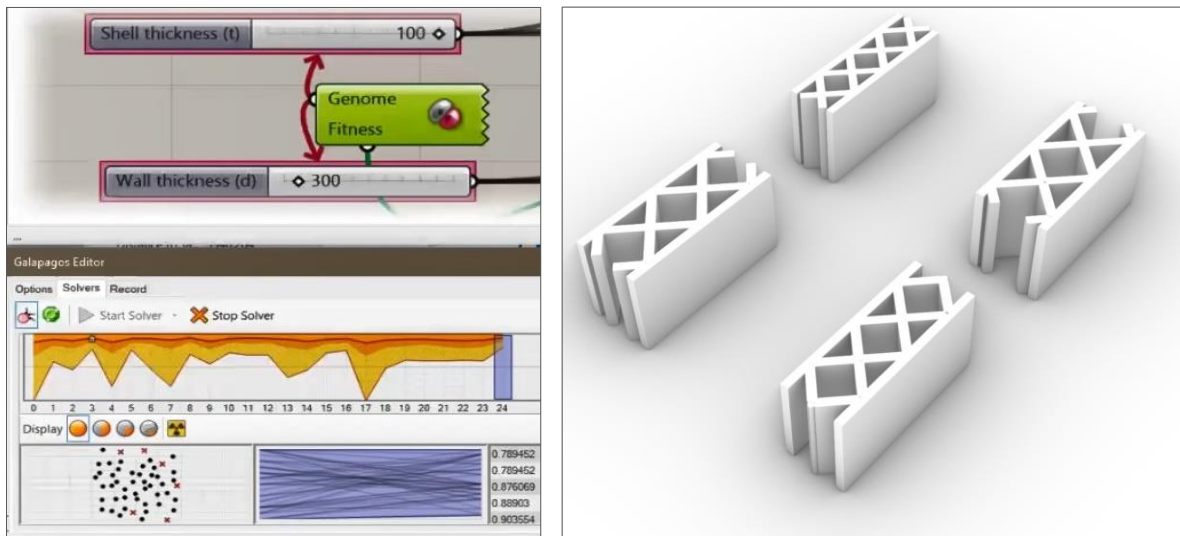


Figure 13: Visual representation of the optimisation process of Galapagos (left) and a sample of the visual generation of results for wall type C in Grasshopper (right).

## 4.2 Results and discussion

### 4.2.1 Single-scenario analysis

The typical relationship between structural adequacy versus the wall section geometry is illustrated in Figure 14, which plots contour lines of constant utilisation ( $u$ ) as a function of shell thickness ( $t$ ) and nominal wall depth ( $d$ ). The graph corresponds to a single scenario where  $H_w = 2.5$  m,  $L_{trib} = 3.5$  m, and  $n_s = 2$ ; however, the general trends are representative regardless of the selected values of these inputs. The thick black contour line corresponding to  $u=1$  represents sections whose capacity exactly matches the design load. Thus, the grey-shaded area above  $u=1$  encompasses sections that are structurally adequate. The red dashed line delineates the zones where the section is compact (governed by the material crushing) as opposed to slender (governed by local buckling), as per Eq (2). The black dashed lines bound the range of  $t$  values that correspond to available nozzle sizes in the 3DP system used in the present experimental study.

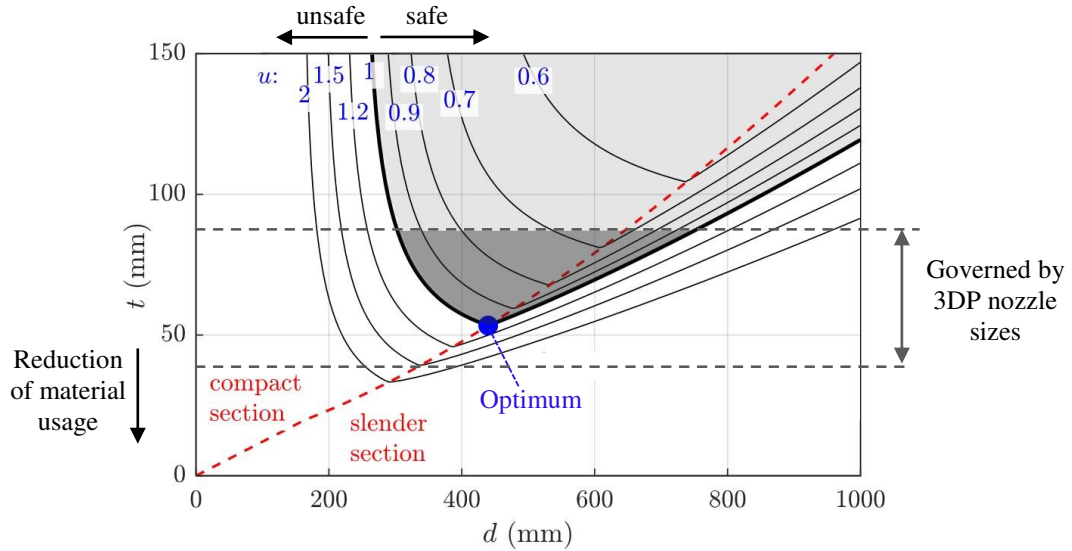


Figure 14: Typical utilisation-contour plot for varied shell thickness ( $t$ ) and nominal wall depth ( $d$ ). Shaded grey area indicates the zone where the wall's capacity is adequate for the design load. The dashed red line delineates compact sections (material stress failure) from slender sections (local-buckling failure). In this example:  $H_w = 2.5\text{m}$ ,  $L_{trib} = 3.5\text{m}$ ,  $n_s = 2$ .

For any of the printed patterns (A, B, C) the area-per-unit-length is approximately proportional to shell thickness (i.e.  $t \propto \bar{A}$ ), thus allowing the shell thickness to be used as a proxy for material consumption. Therefore, in the graphical representation in Figure 14, the optimal section occurs at the trough of the  $u=1$  contour line where  $t$  is minimised. Notably, the  $u$  contours follow different trajectories in the compact- and slender-section zones, and the optimal solution always occurs at the boundary that delineates them. In the compact-section zone, there is a roughly inverse relationship between  $t$  and  $d$ ; this is because a section with a reduced depth requires a thicker shell to maintain the necessary section area and moment of inertia. In the slender-section zone the capacity is governed by local buckling of the shell, and hence increasing the section depth requires an increase to the shell thickness to maintain a constant capacity. The existence of an optimal section also demonstrates that hollow 3DP sections offer improved material efficiency compared to equivalent solid sections. These observations also highlight that in the practical range of interest, the design capacity of the wall is governed both by the material's compressive strength and elastic modulus, underscoring the importance of both these properties.

#### 4.2.2 Design charts based on experimentally quantified material properties

The loadbearing capability of 3DP cob walls is examined in Figure 15 and Figure 16 by presenting model design charts for varied tributary width and wall height respectively. The figures plot the smallest required shell thickness ( $t$ ) and accompanying wall thickness ( $d$ ) of the optimised wall section that minimises material consumption. The constant inputs used to generate these figures are summarised in Table 4 and include the material properties established in Section 3. Figure 15 maintains a constant wall height of 3.0 m while varying the tributary width up to a maximum of 6 m. Conversely, Figure 16 maintains a constant tributary width at

4.0 m while varying the wall height between 2.5 to 3.5 m. These ranges of dimensions were selected to reflect the practical bounds of interest in a typical residential building. Each figure considers separately the alternate printed patterns (A, B, C) in either a 1- or 2-storey building. The relative efficiency of the alternate sections is presented in Figure 17 and Figure 18 by plotting the section area per unit length (a proxy for the material consumption).

Overall, the plots demonstrate that, on the assumption of the mechanical properties matching those established in the accompanying tests, loadbearing structural function in typical residential construction can be accomplished using wall section sizes that are reasonable and within the capability of the 3D printer system. The indicative range of shell thickness and wall thickness is summarised in Table 5. It is seen that in a single-storey house the section size can be kept small ( $t = 25\text{--}40\text{ mm}$ ,  $d = 250\text{--}400\text{ mm}$ ) relative to a 2-storey house ( $t = 35\text{--}120\text{ mm}$ ,  $d = 320\text{--}800\text{ mm}$ ).

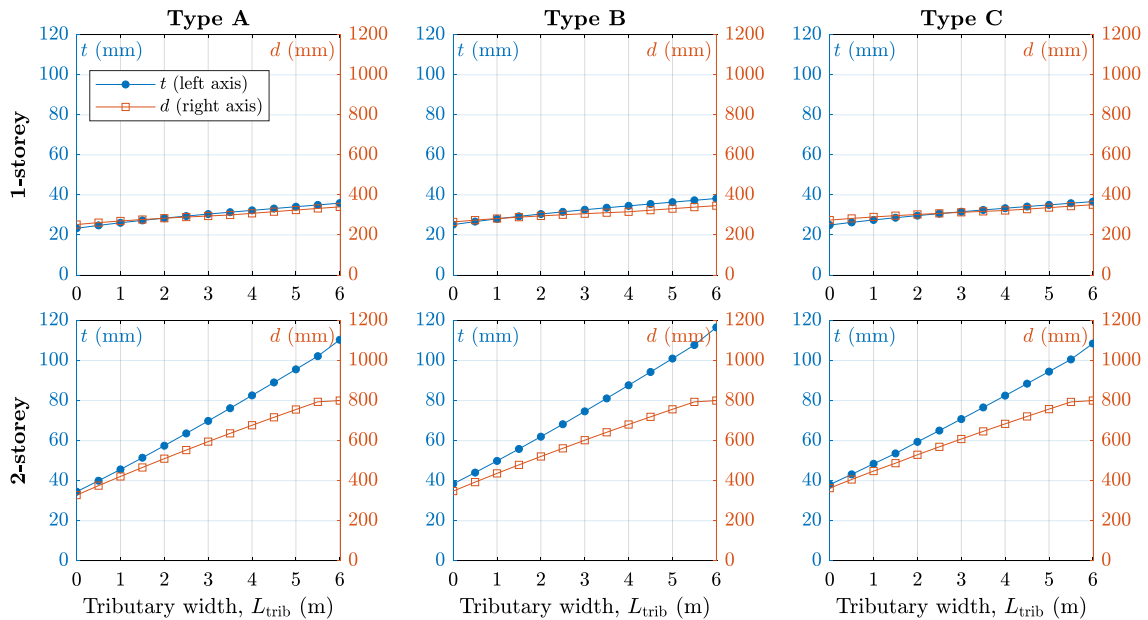


Figure 15: Dimensions  $t$  and  $d$  of optimised sections for varied tributary width (constant wall height of 3 m). All inputs including material properties are as per Table 4. Considers section types A, B, C, and either a 1- or 2-storey building. Each plot shows  $t$  on the left y-axis and  $d$  on the right y-axis.



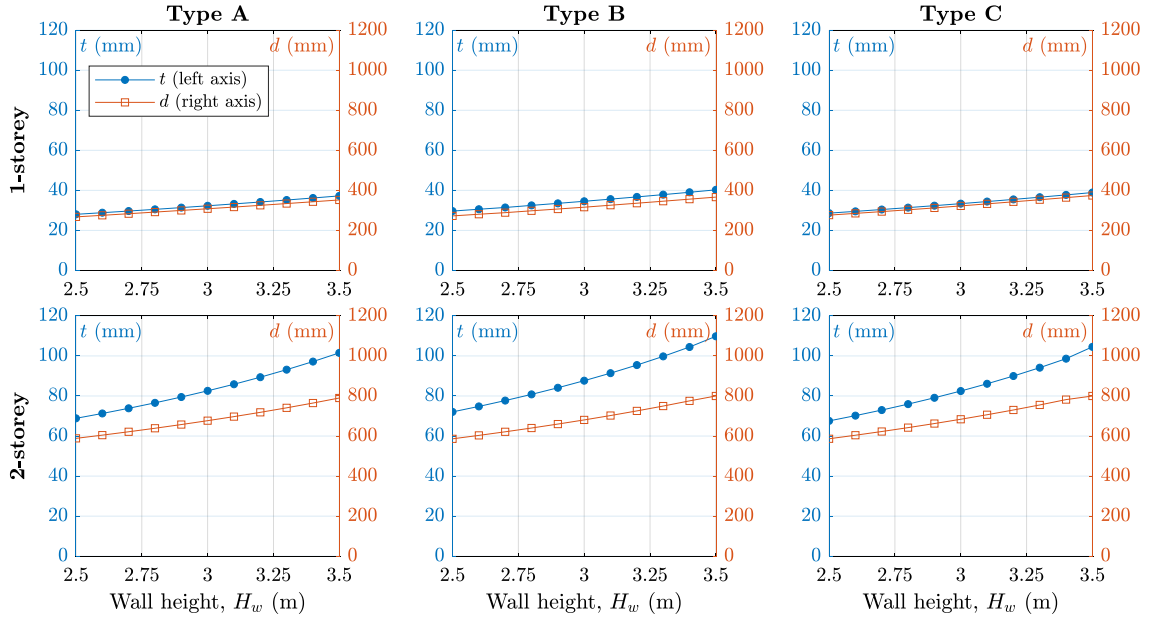


Figure 16: Dimensions  $t$  and  $d$  of optimised sections for varied wall height (constant tributary width of 4 m). All inputs including material properties are as per Table 4. Considers section types A, B, C, and either a 1- or 2-storey building. Each plot shows  $t$  on the left y-axis and  $d$  on the right y-axis.

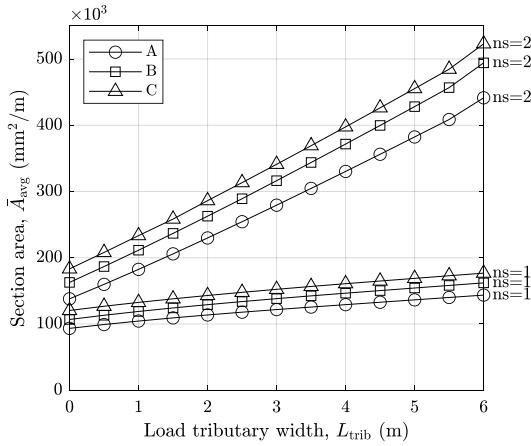


Figure 17: Section area per unit length for the optimised sections in Figure 15.

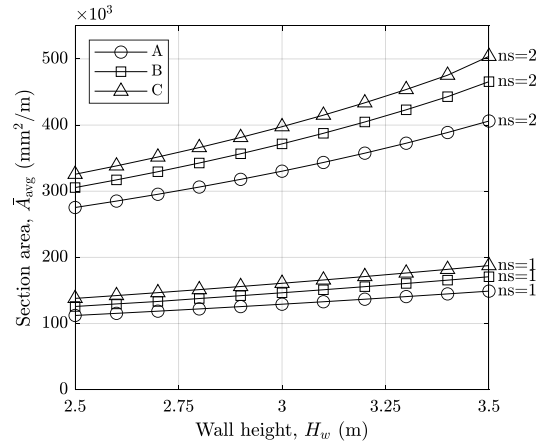


Figure 18: Section area per unit length for the optimised sections in Figure 16.

Table 5: The range of the section-defining parameters  $t$  and  $d$  corresponding to the design charts in Figure 15 and Figure 16.

	1 storey		2 stories	
	Min (mm)	Max (mm)	Min (mm)	Max (mm)
Shell thickness ( $t$ )	25	40	35	115
Wall thickness ( $d$ )	250	400	320	800

561 Note that in scenarios where a small section geometry may be permitted by structural  
562 considerations alone, the actual section could in practicality be dictated by other factors such  
563 as architectural requirements, aesthetics, thermal performance, standardisation of the  
564 construction process, and the capability of the 3D-printing system. For instance, a previous  
565 study by Gomaa et al. [21] found that 3D printing of large-scale cob walls requires a nozzle  
566 size of at least 40 mm, which can be used to generate an ‘average’ shell thickness ( $t$ ) between  
567 50–80 mm. Smaller nozzle diameters can slow down the printing process and also cause  
568 clogging of the extrusion system. On the other hand, using larger nozzles leads to reduced  
569 control over material consumption and accuracy.

570 The plots in Figure 17 and Figure 18 indicate that based solely on their structural performance,  
571 of the three section types, A is the most efficient, followed by B and then C. However, on any  
572 project it may also be necessary to consider other factors that may be impacted by the type of  
573 wall section. For example, from an architectural perspective, the notion of efficiency also  
574 includes considerations such as the design function, thermal performance, and environmental  
575 impacts. For instance, the thermal performance efficiency of 3DP cob was explored thoroughly  
576 in a recent study by Gomaa et al. [22], which demonstrated that the voids present in 3DP wall  
577 patterns dramatically improve thermal efficiency compared to solid cob walls. This means that  
578 the relative thermal performance of the alternate wall sections A, B or C may not necessarily  
579 match their relative structural performance. Hence, it is recommended that selecting the wall  
580 section type should be undertaken using a holistic approach that considers their structural,  
581 thermal, and environmental efficiency.

#### 582 4.2.3 Parametric study into the influence of the material properties

583 As demonstrated by the review of experimental studies (Table 1), the mechanical properties of  
584 cob can exhibit drastic variation depending on the mix composition. To account for the limited  
585 number of material tests in the current study, a parametric study was undertaken to examine  
586 the sensitivity of the feasibility study findings on the quality of the material. To this end, the  
587 mean compressive strength ( $f_{cm}$ ) and elastic modulus ( $E$ ) were varied so as to cover a realistic  
588 range of the respective properties as identified through the review of past testing (Table 1).

591 Three scenarios were considered (Note: Symbol ‘\*’ refers to the value being representative of  
592 the accompanying tests in Section 3):

- 593 1. Varied  $f_{cm} = 0.6/0.9^*/1.35$  MPa, at constant  $E = 23^*$  MPa,
- 594 2. Varied  $E = 20^*/40/80$  MPa, at constant  $f_{cm} = 0.87^*$  MPa,
- 595 3.  $E$  and  $f_{cm}$  both varied in equal proportion:  $[f_{cm}, E] = [0.4, 20^*]$ ,  $[0.8^*, 40]$ , and  $[1.6, 80]$   
596 MPa.

597  
598 The purpose of the first two scenarios was to gain insight into the parametric influence of the  
599 respective properties by varying them in isolation, while the third was meant to represent  
600 variation of the overall quality of the material by changing both properties simultaneously.

602 The study considers wall pattern type C and varies the tributary width while keeping  $H_w = 3$   
603 m. Aside from  $f_c$  and  $E$ , the remaining inputs listed in Table 4 remain unchanged. The results  
604 are presented in Figures 19–24 respectively.

605  
606 • Scenario 1

607 The first scenario (Figures 19 and 20) looks at variation of compressive strength between  
608 0.6/0.9/1.35 MPa while maintaining  $E$  as per the current tests (23 MPa). Note that the  
609 intermediate strength level (0.9 MPa) is similar to the result of the current tests. It is observed  
610 that in the 1-storey case, the required cross section is relatively insensitive over the three levels  
611 of strength. In the 2-storey case however, the reduced strength (0.6 MPa) requires a cross  
612 section that becomes excessively large for any tributary width exceeding 1m, thus making the  
613 walls effectively incapable of performing a loadbearing function. Conversely, the improved  
614 strength (1.35 MPa) allows for a smaller section to be used, saving up to 30% in material  
615 volume.

616  
617 • Scenario 2

618 The second scenario (Figures 21 and 22) looks at variation of the elastic modulus at levels of  
619 20/40/80 MPa while maintaining  $f_{cm}$  as per the current tests (0.87 MPa). The lowest  $E$  value  
620 (i.e. 20 MPa) is comparable to the material of the current tests. For both the 1- and 2-storey  
621 cases, a higher elastic modulus leads to a reduction in the necessary cross section size. The  
622 improvement in increasing  $E$  from 20 to 80 MPa results in a material saving between 10–50%.  
623 It is also interesting to note that a higher elastic modulus results in an optimal cross section that  
624 has an increased wall thickness ( $d$ ) while having a lower shell thickness ( $t$ ); this can be  
625 explained by improved resistance to local buckling.

626  
627 • Scenario 3

628 The last scenario (Figures 23 and 24) examines the effect of proportionally increasing both  $f_{cm}$   
629 and  $E$ , which can be considered analogous to an overall variation in the quality of the material,  
630 i.e. low (0.4/40MPa), intermediate (0.8/40MPa) and high (1.6/80MPa) quality. The graphs  
631 indicate a strong dependence between the loadbearing capacity (i.e. required section size) and  
632 the input material properties in both the 1- and 2-storey cases. While not being directly  
633 comparable to the previous two scenarios because of different input values, a general  
634 comparison indicates that the most efficient improvement in overall loadbearing performance  
635 is achieved by simultaneously enhancing both  $f_{cm}$  and  $E$ , rather than by increasing either of  
636 these properties alone.

637  
638 Overall, the sensitivity study indicates that the feasibility of cob walls to act as loadbearing is  
639 conditional on a minimum required level of material performance. The 3DP cob tested in this  
640 study meets this threshold, but it is evident that a reduced compressive strength ( $< 0.75$  MPa)  
641 may not be sufficient for loadbearing walls in a 2-storey house. On the other hand, even weak  
642 cob ( $\approx 0.4$  MPa) may still be sufficient to construct loadbearing walls in a single-storey house.

644

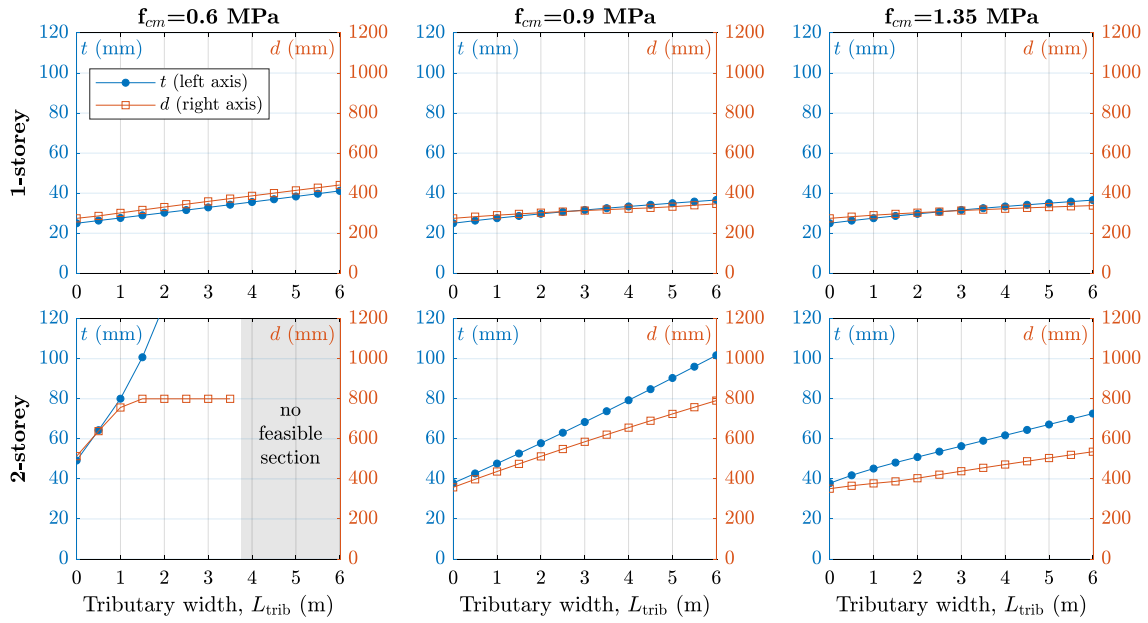


Figure 19: Dimensions  $t$  and  $d$  of optimised sections for varied compressive strength (constant  $E$ ).

645

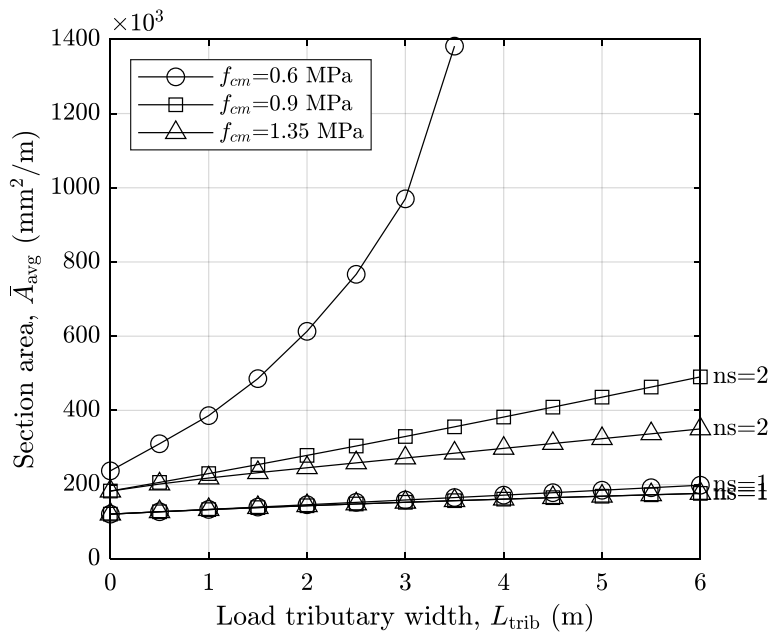


Figure 20: Material consumption of the optimised sections plotted in Figure 19.

646

647

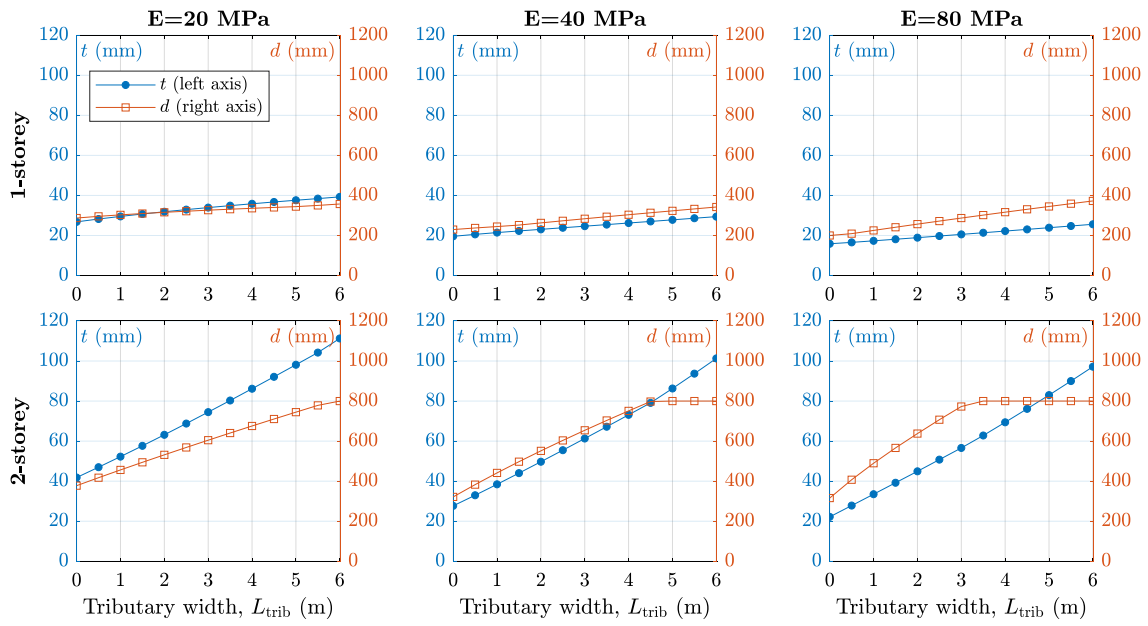


Figure 21: Dimensions  $t$  and  $d$  of optimised sections for varied elastic modulus (constant  $f_{cm}$ ).

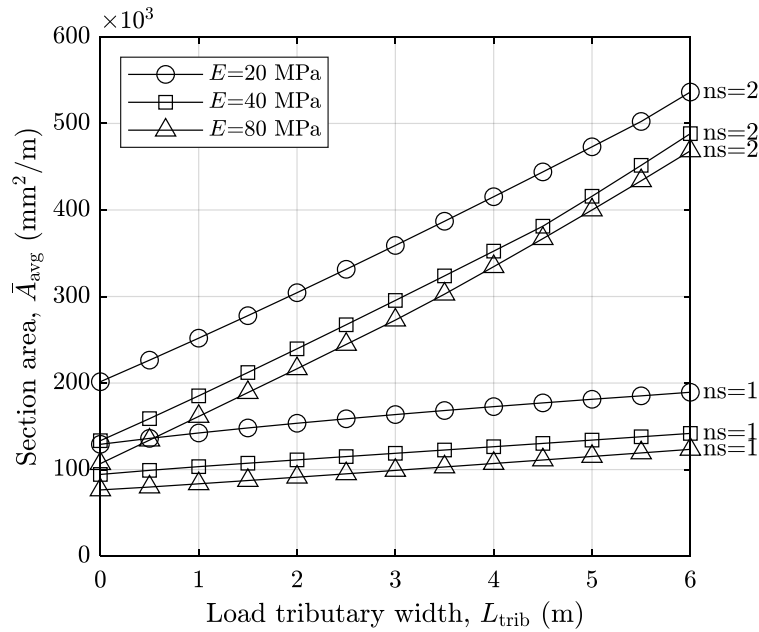


Figure 22: Material consumption of the optimised sections plotted in Figure 21.

653

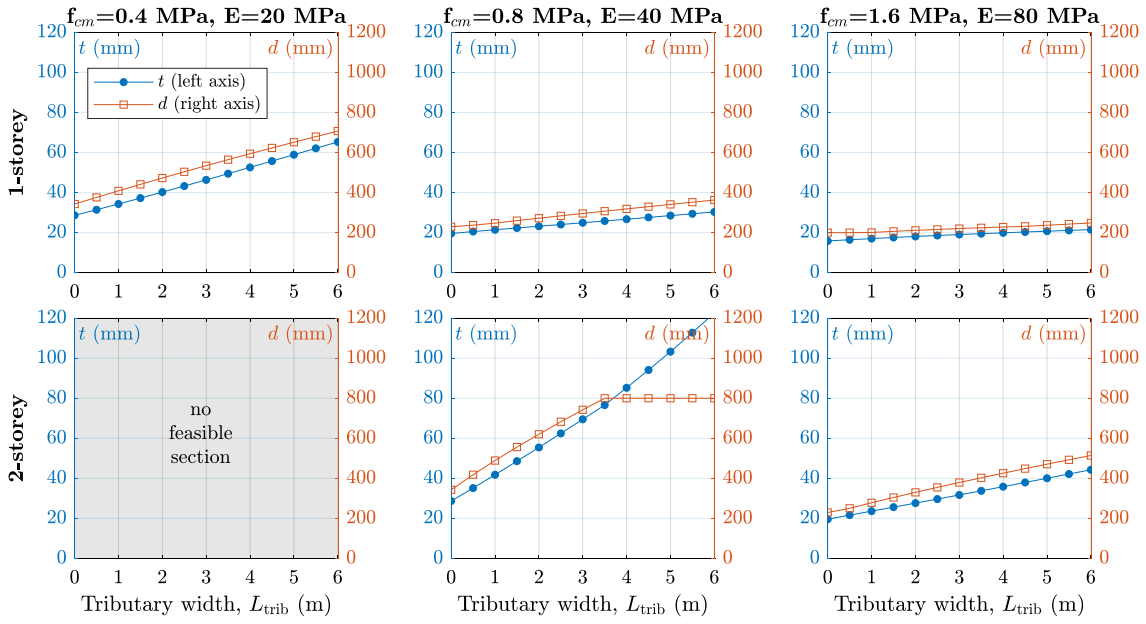


Figure 23: Dimensions  $t$  and  $d$  of optimised sections for varied  $f_{cm}$  and  $E$ , with ratio  $f_{cm}/E$  held fixed.

654

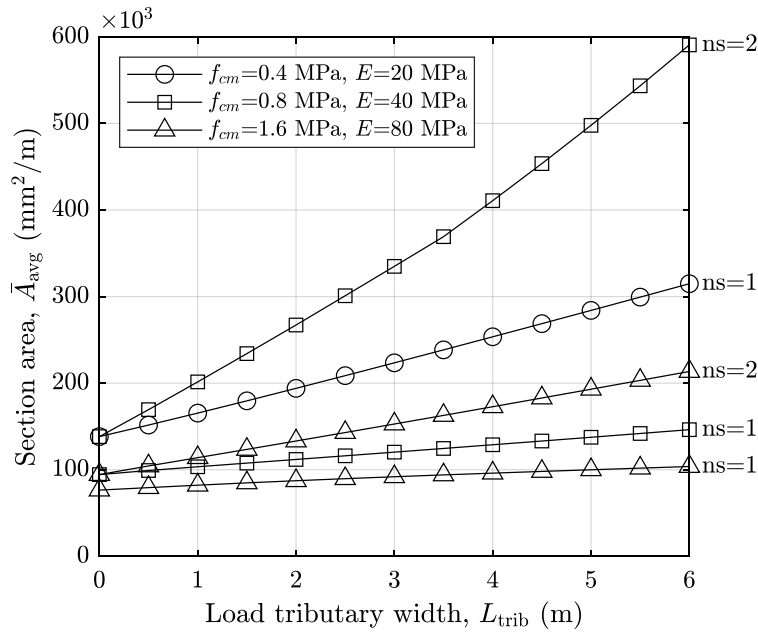


Figure 24: Material consumption of the optimised sections plotted in Figure 23.

655

656

657

658

659



## 5 Case study of a small 3DP cob house

As explained previously, the approach to leveraging the wall sizing charts (e.g. Figure 15) depends both on structural and architectural design considerations. To demonstrate the essential design process, a case study involving a small house will now be presented. The process starts with a floor plan defining the zoning and dimensions of the spaces (Figure 25). For illustrative purposes, the hypothetical house incorporates four spaces with different sizes and opening configurations, representing typical design requirements. The dimensions of the spaces range from 2m to 4 m, wall heights are set at 3m, and the number of storeys is taken as either 1 or 2. The roof (in the 1 and 2-storey cases) and the suspended floor (in the 2-storey case) are treated as one-way spanning in the directions indicated on Figure 25.

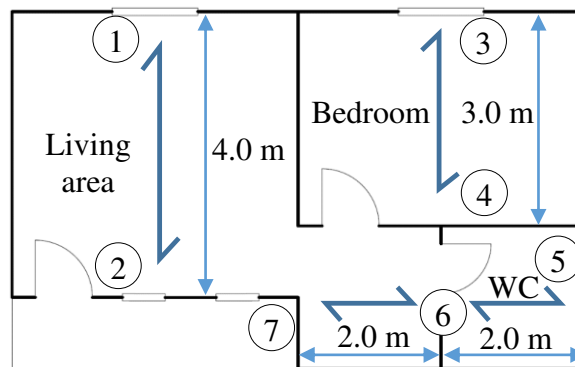


Figure 25: Basic floor plan of the idealised 3DP cob house. Half-headed arrows indicate the span direction of the suspended floor and roof. Loadbearing walls are numbered from 1 to 7.

The design parameters and final sizing of each wall are summarised in Tables 6 and 7 for the single and double storey alternatives respectively. The procedure to determine the minimum section sizes is as follows:

1. Establish which walls are loadbearing by considering the span direction of the floor/roof. In this example, walls 1–7 are loadbearing (Figure 25).
2. The ‘basic’ tributary width of each loadbearing wall is determined by considering whether the wall is internal or external and the effective span of the floor/roof being supported, using gross dimensions (refer to Figure 10).
3. If the wall has an opening, the basic tributary width is upscaled in relation to the ratio of the openings (as described in Section 4.1.4). For instance, a wall containing 50% openings (in plan view) carries an effective tributary width equal to double the basic tributary width. Note that for simplicity, the effective tributary widths in Tables 6 and 7 are rounded-up to the nearest 1m.
4. Non-loadbearing walls are analogous to having a zero effective tributary width.
5. The effective tributary width is then used to select  $t$  and  $d$  from the relevant design chart (Figure 15).

Note that the nominated section sizes in Tables 6 and 7 assume the material properties quantified in the accompanying material tests (i.e. using Figure 15). Also note that consideration is given here only to gravity loads and not to out-of-plane loads due to wind or earthquake, which are region-specific and outside the scope of the current paper.

Figure 26 illustrates the floor plan by assigning the minimum section sizes to each wall. Since the minimum required section size can be different for each wall, the designer has the choice of standardising the sizes as needed to suit the other project requirements (e.g. thermal and architectural) which may also serve to reduce the complexity of the design and improve the efficiency of the construction process.

Table 6: Design of loadbearing (1–7) and non-loadbearing (NLB) walls in the 1-storey example house.

Wall	Basic $L_{trib}$ (m)	Opening ratio (%)	Tributary scale factor	Effective $L_{trib}$ (m)	Corresponding $t$ and $d$ (mm)					
					Type A		Type B		Type C	
					$t$	$d$	$t$	$d$	$t$	$d$
1	2	25	1.5	3	30	300	35	310	35	320
2	2	50	2.0	4	<b>35</b>	<b>310</b>	<b>35</b>	<b>320</b>	<b>35</b>	<b>330</b>
3	1.5	30	1.6	3	30	300	35	310	35	320
4	1.5	15	1.3	2	30	290	35	300	35	310
5	1	5	1.1	1	<b>30</b>	<b>280</b>	<b>30</b>	<b>290</b>	<b>30</b>	<b>300</b>
6	2	30	1.6	3	30	300	35	310	35	320
7	1	40	1.8	2	30	290	35	300	35	310
NLB	0	0	n/a	0	25	320	25	350	25	380

Table 7: Design of loadbearing (1–7) and non-loadbearing (NLB) walls in the 2-storey example house.

Wall	Basic $L_{trib}$ (m)	Opening ratio (%)	Tributary scale factor	Effective $L_{trib}$ (m)	Corresponding $t$ and $d$ (mm)					
					Type A		Type B		Type C	
					$t$	$d$	$t$	$d$	$t$	$d$
1	2	25	1.5	3	70	600	75	600	70	600
2	2	50	2.0	4	<b>80</b>	<b>700</b>	<b>85</b>	<b>640</b>	<b>80</b>	<b>700</b>
3	1.5	30	1.6	3	70	600	75	600	70	600
4	1.5	15	1.3	2	60	500	60	520	60	520
5	1	5	1.1	1	<b>45</b>	<b>420</b>	<b>50</b>	<b>420</b>	<b>50</b>	<b>420</b>
6	2	30	1.6	3	70	600	75	600	70	600
7	1	40	1.8	2	60	500	60	520	60	520
NLB	0	0	n/a	0	35	350	40	370	40	390

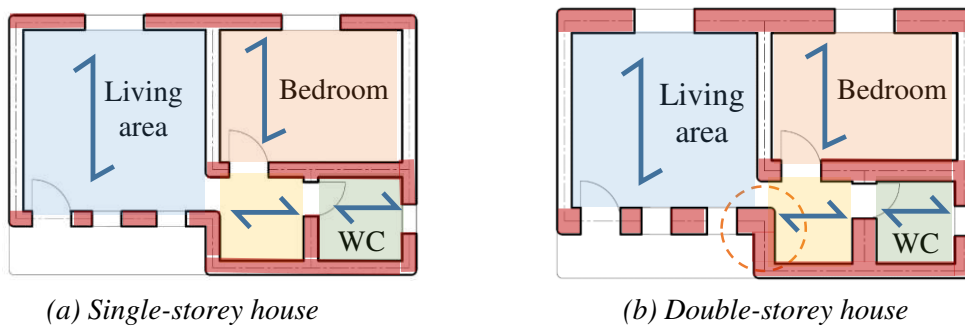


Figure 26: Floor plan showing the minimum required wall sizes walls to scale. (Shown for pattern type A for illustrative purposes)

From Table 6 and Figure 26a, it can be seen that in the case of 1-storey house, the required sections are relatively consistent across all of the walls present (in terms of  $t$  and  $d$ ), regardless of the chosen pattern (A, B, C). For example, if we consider pattern A, the required  $t$  varies between 30–35 mm, and  $d$  between 280–310 mm. The consistency in wall sizes in the case of a 1-storey building results from the required cross section being relatively insensitive to the tributary width, as reflected by Figure 15. For construction simplicity, the designer may therefore choose to standardise the wall sizes by assigning the largest required section to every wall.

In contrast to the 1-storey house, in the case of the 2-storey house the required section sizes (Table 7) vary substantially between the walls present (e.g. for type A:  $t = 45\text{--}80$  mm,  $d = 420\text{--}700$  mm). The resulting floor plan (Figure 26b) visually illustrates the difference in the wall thickness demands, especially between loadbearing and non-loadbearing walls. Therefore, in the case of the 2-storey building, the designer may opt for a suitable compromise between standardising the wall section sizes and economical material usage, for instance by adopting two or three different sizes across the building. Large wall thickness can also negatively impact the architectural functionality of the spaces, where, as highlighted in this example by the dotted circle in Figure 26b, the aisle linking the living area with the bedroom becomes severely narrowed due to the large thickness of the walls on both sides. Such considerations may require an iterative re-adjustment of the floor plan until both the structural and architectural requirements are satisfied.

An alternate way that the designer can balance the structural and architectural requirements in relation to wall section sizes is by dictating the gravity load path by controlling: 1) the span directivity of the floor/roof system being carried by the walls, 2) which cob walls act as loadbearing, and 3) which internal walls can be formed using lightweight partitions. To demonstrate this, Figure 27 illustrates three alternatives that maintain the same space layout as the original arrangement (Figure 25) but are reconfigured by altering the floor (or roof) spans and by implementing internal partitions to affect which walls are loadbearing.

Arrangement (a) is similar to the original configuration but rotates the floor span in south-east zone, thus allowing cob wall no. 6 (see Figure 25) to be replaced by a lightweight partition and also to reduce the size of wall no. 7. By removing some of the internal cob walls, configuration (a) arguably reduces the overall 3DP construction complexity compared to the original layout.

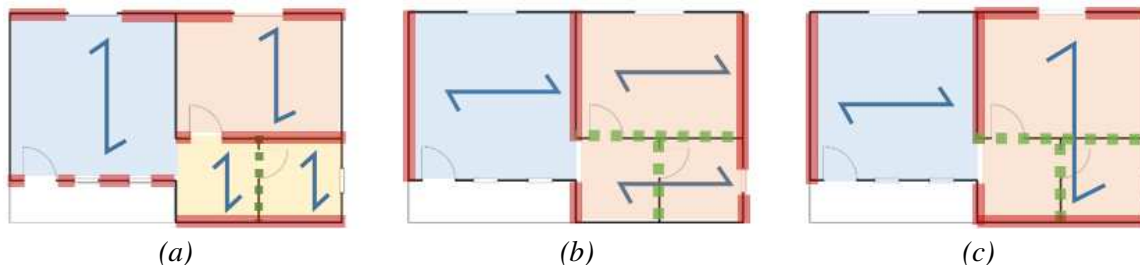
737 It does however increase the load demand on internal wall no. 4, therefore enlarging its section,  
738 and potentially hindering the functionality of the smaller rooms (i.e. toilets and lobby).

739 The presence of the internal cob wall (no. 4) in the original arrangement and configuration (a)  
740 also limits the freedom for future architectural changes to the internal space layout.  
741 Configurations (b) and (c) address this by replacing the internal walls in the east side of the  
742 house with lightweight partitions, thus improving the versatility for future layout alternations,  
743 but at the cost of requiring larger external walls because of a longer floor span in the east half  
744 out the house [compared to (a)].

745 Comparing configurations (b) and (c), a possible downside of (b) is that the central wall  
746 requires a large section since it acts as an internal loadbearing wall. By altering the direction  
747 of the floor span in the east half of the house, configuration (c) approximately halves the load  
748 on the central wall, but it does so at the cost of making the north and south outer walls  
749 loadbearing. Overall this would act to make the required wall sizes in option (c) more uniform  
750 across the house than in option (b), thus making (c) the potentially preferable option from a  
751 constructability point-of-view.

752 Overall, this example demonstrates that the process of selecting of the structural configuration  
753 is and exercise that involves compromise between a number of factors, including

- 754 • the dimensions and functionality of the spaces and location of openings,
- 755 • constructability and economical use of material,
- 756 • allowance for future alterations to the internal layout, and
- 757 • other factors not considered here, such as thermal insulation performance.



758  
759  
760  
761  
762  
763  
764  
765  
*Figure 27. Examples of alternative arrangements of the floor/roof span directivity in the example small 3DP cob house. The loadbearing walls in each instance are highlighted in red. The lightweight partitions are highlighted in green dotted lines.*

## 6 Conclusion

760 The increased uptake of 3DP technologies in construction, accompanied by a movement toward  
761 environmentally efficient materials has led to leveraging earthen materials in a contemporary  
762 3DP process. 3DP cob has been a subject of investigation for several years now; however,  
763 while those investigations have focused mostly on the architectural aspects and environmental  
764 performance, investigation into the material's feasibility to be used for load-carrying building  
765 elements has not yet been undertaken sufficiently.

766 This study has conducted a comprehensive feasibility investigation into the structural capacity  
767 of 3DP cob walls under gravity loads. This was accomplished by first quantifying the basic  
768 mechanical properties of 3DP cob using a standardised compression test. The tests  
769 demonstrated that 3DP cob appears to exhibit similar mechanical performance to conventional  
770 cob in terms of compressive strength and elastic modulus. The expected load-carrying capacity  
771 of 3DP walls was then predicted using established structural mechanics concepts and limit-  
772 state design principles. These predictions demonstrate that 3DP cob walls are expected to have  
773 sufficient capacity to act as loadbearing in residential buildings up to two storeys.

774 The feasibility study also demonstrated the following:

- 775 • Due to the favourable geometric properties of printable hollow sections, 3DP cob walls can  
776 perform a loadbearing function with more efficient material usage compared to traditional  
777 (non-3DP) solid cob walls.
- 778 • The model design approach demonstrated in this paper provides a means for integrating the  
779 structural design process of 3DP cob into the design-to-construction framework. The  
780 generated design guidelines can be directly implemented to a Rhino-Grasshopper definition  
781 that enables visual modelling and direct interfacing with the 3D-printing system.
- 782 • The range of wall section sizes (as informed by the analysis) required for loadbearing  
783 functionality in buildings up to 2-storeys can be efficiently fabricated using available 3DP  
784 technologies and extrusion systems.

785 The findings of this study complete a broader feasibility investigation of 3DP cob for modern  
786 construction which combines structural performance with three other aspects: 1)  
787 constructability and fabrication process, 2) thermal performance, and 3) life cycle assessment.  
788 The results lead to the conclusion that 3DP cob construction emerges as a strong competitor to  
789 conventional and 3DP concrete construction. 3DP cob can substitute concrete-based  
790 construction in small to medium size low-rise residential projects, especially as it provides  
791 higher environmental efficiency and rationalised energy use. It can also provide novel design  
792 opportunities in addition to higher precision compared to manually constructed cob, especially  
793 for producing complex geometries. Moreover, 3DP cob construction can provide quick  
794 sheltering solutions with low cost and efficient use of local materials in expeditionary and  
795 hostile environments.

796 It is however important to highlight that while the current study provides promising and  
797 necessary first insight into the structural feasibility of 3DP cob walls, the findings are based on  
798 structural analysis with input from small-scale material tests. Therefore, proof-of-concept  
799 structural testing on full printed wall sections is envisaged as a crucial next step of this research.

800 Furthermore, while the outcomes of this study are positive overall, the accompanying  
801 sensitivity study undertaken demonstrates that the quality of the material in terms of its  
802 mechanical properties (compression strength and elastic modulus) is highly influential on the  
803 resulting loadbearing capability of the walls. Therefore, further research into the development  
804 of 3DP-suitable cob mixtures with a focus on ensuring consistently high-quality mechanical  
805 performance could yield significant additional benefit to this form of construction.  
806 Accompanying focus into other material performance aspects, in particular shrinkage and  
807 creep, is also required.

808 **Acknowledgements**

1  
2 809 We would like to acknowledge Dr Alejandro Veliz Reyes for his valuable collaboration and  
3 support (University of Plymouth). We also extend our gratitude to Aikaterini Chatzivasileiadi  
4 810 and Anas Lila (Cardiff University) for their invaluable help.  
5 811  
6

7 812 **Funding Resources**

8  
9  
10 813 This work was supported financially by the Engineering and Physical Sciences Research  
11 814 Council (EPSRC) and The University of Nottingham under the Network Plus: Industrial  
12 815 Systems in the Digital Age, Grant number: EP/P001246/1. This work is also partially supported  
13 816 by the University of Adelaide through the Research Abroad Scholarship scheme.  
14  
15

16 817 **References**

- 17  
18 818 [1] P. Feng, X. Meng, J.-F. Chen, and L. Ye, “Mechanical properties of structures 3D  
19 819 printed with cementitious powders,” *Constr. Build. Mater.*, vol. 93, pp. 486–497, 2015,  
20 820 doi: 10.1016/j.conbuildmat.2015.05.132.  
21 821 [2] A. Kazemian, X. Yuan, E. Cochran, and B. Khoshnevis, “Cementitious materials for  
22 822 construction-scale 3D printing: Laboratory testing of fresh printing mixture,” *Constr.*  
23 823 *Build. Mater.*, vol. 145, pp. 639–647, 2017, doi: 10.1016/j.conbuildmat.2017.04.015.  
24 824 [3] B. Zareiyan and B. Khoshnevis, “Interlayer adhesion and strength of structures in  
25 825 Contour Crafting - Effects of aggregate size, extrusion rate, and layer thickness,”  
26 826 *Autom. Constr.*, vol. 81, pp. 112–121, 2017, doi: 10.1016/j.autcon.2017.06.013.  
27 827 [4] B. Khoshnevis, “Automated construction by contour crafting — related robotics and  
28 828 information technologies,” vol. 13, pp. 5–19, 2004, doi: 10.1016/j.autcon.2003.08.012.  
29 829 [5] T. T. Le, S. A. Austin, S. Lim, R. A. Buswell, A. G. F. Gibb, and T. Thorpe, “Mix  
30 830 design and fresh properties for high-performance printing concrete,” *Mater. Struct.*  
31 831 *Constr.*, vol. 45, pp. 1221–1232, 2012, doi: 10.1617/s11527-012-9828-z.  
32 832 [6] A. Perrot, D. Rangeard, and A. Pierre, “Structural built-up of cement-based materials  
33 833 used for 3D- printing extrusion techniques,” *Mater. Struct.*, vol. 49, pp. 1213–1220,  
34 834 2016, doi: 10.1617/s11527-015-0571-0.  
35 835 [7] L. Wang, H. Jiang, Z. Li, and G. Ma, “Mechanical behaviors of 3D printed lightweight  
36 836 concrete structure with hollow section,” *Arch. Civ. Mech. Eng.*, vol. 20, pp. 1–17, Mar.  
37 837 2020, doi: 10.1007/s43452-020-00017-1.  
38 838 [8] H. Alhumayani, M. Gomaa, V. Soebarto, and W. Jabi, “Environmental Assessment of  
39 839 large-Scale 3D Printing in Construction: A Comparative Study between Cob and  
40 840 Concrete,” *J. Clean. Prod.*, vol. 270, pp. 122463, Jun. 2020, doi:  
41 841 10.1016/j.jclepro.2020.122463.  
42 842 [9] CyBe, “3D Studio 2030 — CyBe Construction,” 2019. [https://cybe.eu/case/3d-studio-](https://cybe.eu/case/3d-studio-2030/)  
43 843 [2030/](https://cybe.eu/case/3d-studio-2030/) (accessed Nov. 20, 2019).  
44 844 [10] C. Shrubsole *et al.*, “Bridging the gap: The need for a systems thinking approach in  
45 845 understanding and addressing energy and environmental performance in buildings,”  
46 846 *Indoor Built Environ.*, vol. 28, pp. 100–117, 2019, doi: 10.1177/1420326X17753513.  
47 847 [11] S. Ford and M. Despeisse, “Additive manufacturing and sustainability: an exploratory  
48 848 study of the advantages and challenges,” *J. Clean. Prod.*, vol. 137, pp. 1573–1587,  
49 849 2016, doi: 10.1016/j.jclepro.2016.04.150.  
50 850 [12] E. Hamard, B. Cazacliu, A. Razakamanantsoa, and J. C. Morel, “Cob, a vernacular  
51 851 earth construction process in the context of modern sustainable building,” *Build.*  
52 852 *Environ.*, vol. 106, pp. 103–119, 2016, doi: 10.1016/j.buildenv.2016.06.009.  
53  
54  
55  
56  
57  
58  
59  
60  
61  
62  
63  
64  
65



- 853 [13] E. Quagliarini, A. Stazi, E. Pasqualini, and E. Fratolocchi, "Cob construction in Italy:  
 1 854 Some lessons from the past," *Sustainability*, vol. 2, pp. 3291–3308, 2010, doi:  
 2 855 10.3390/su2103291.
- 3 856 [14] T. Morton, F. Stevenson, B. Taylor, and N. C. Smith, "Low Cost Earth Brick  
 4 857 Construction: Monitoring & Evaluation," Fife, UK, 2005. [Online]. Available:  
 5 858 [http://www.arc-architects.com/downloads/Low-Cost-Earth-Masonry-Monitoring-](http://www.arc-architects.com/downloads/Low-Cost-Earth-Masonry-Monitoring-Evaluation-Report-2005.pdf)  
 6 859 [Evaluation-Report-2005.pdf](http://www.arc-architects.com/downloads/Low-Cost-Earth-Masonry-Monitoring-Evaluation-Report-2005.pdf).
- 7 860 [15] L. Ben-Alon, V. Loftness, K. A. Harries, and E. Cochran Hameen, "Integrating  
 8 861 Earthen Building Materials and Methods into Mainstream Construction Using  
 9 862 Environmental Performance Assessment and Building Policy," *IOP Conf. Ser. Earth*  
 10 863 *Environ. Sci.*, vol. 323, pp. 012139, 2019, doi: 10.1088/1755-1315/323/1/012139.
- 11 864 [16] O. O. Akinkurolere, C. Jiang, A. T. Oyediran, O. I. Dele-Salawu, and A. K. Elensinnla,  
 12 865 "Engineering properties of Cob as a building material," *Journal of Applied Sciences*,  
 13 866 vol. 6, pp. 1882–1885, 2006, doi: 10.3923/jas.2006.1882.1885.
- 14 867 [17] J. Fordice and L. Ben-Alon, "A research project dedicated to making cob legally  
 15 868 accessible to the public," 2017.
- 16 869 [18] E. Kianfar and V. Toufigh, "Reliability analysis of rammed earth structures," *Constr.*  
 17 870 *Build. Mater.*, vol. 127, pp. 884–895, 2016, doi: 10.1016/j.conbuildmat.2016.10.052.
- 18 871 [19] A. Veliz Reyes, W. Jabi, M. Gomaa, A. Chatzivasileiadi, L. Ahmad, and N. M.  
 19 872 Wardhana, "Negotiated matter: a robotic exploration of craft-driven innovation,"  
 20 873 *Archit. Sci. Rev.*, vol. 62, pp. 1–11, 2019, doi: 10.1080/00038628.2019.1651688.
- 21 874 [20] 3D-WASP, "3D Printers | WASP | Leading Company in the 3d printing industry,"  
 22 875 2020. <https://www.3dwaspp.com/en/> (accessed Jan. 10, 2020).
- 23 876 [21] M. Gomaa, W. Jabi, A. Veliz Reyes, and V. Soebarto, "3D Printing System for Earth-  
 24 877 based construction: Case Study of Cob Walls," *Autom. Constr.*, vol. 124, pp. 103577,  
 25 878 2021, doi: <https://doi.org/10.1016/j.autcon.2021.103577>.
- 26 879 [22] M. Gomaa, J. Carfrae, S. Goodhew, W. Jabi, and A. Veliz Reyez, "Thermal  
 27 880 performance exploration of 3D printed cob," *Archit. Sci. Rev.*, vol. 62, pp. 1–8, Apr.  
 28 881 2019, doi: 10.1080/00038628.2019.1606776.
- 29 882 [23] A. Perrot, D. Rangeard, and E. Courteille, "3D printing of earth-based materials:  
 30 883 Processing aspects," *Constr. Build. Mater.*, vol. 172, pp. 670–676, 2018, doi:  
 31 884 10.1016/j.conbuildmat.2018.04.017.
- 32 885 [24] L. Keefe, *Earth building : methods and materials, repair and conservation*, 1st ed.  
 33 886 New York: Taylor and Francis Ltd., 2005.
- 34 887 [25] S. S. Damluji, *The Architecture of Yemen: From Yafi to Hadramut*. London: Laurence  
 35 888 King Publishing, 2008.
- 36 889 [26] Green Home Buildings, "Mixing and Applying Cob," 2020.  
 37 890 <http://www.greenhomebuilding.com/QandA/cob/mixing.htm> (accessed Jul. 03, 2020).
- 38 891 [27] Earth Devon, "Cob Dwellings: Compliance with The Building Regulations," *Cob*  
 39 892 *Unbaked Earth Dwellings*, vol. 2000, pp. 1–21, 2008.
- 40 893 [28] A. Weismann and K. Bryce, *Building with cob: a step-by-step guide*. Devon: Green  
 41 894 Books ltd, 2006.
- 42 895 [29] L. Miccoli, U. Müller, and P. Fontana, "Mechanical behaviour of earthen materials: A  
 43 896 comparison between earth block masonry, rammed earth and cob," *Constr. Build.*  
 44 897 *Mater.*, vol. 61, pp. 327–339, 2014, doi: 10.1016/j.conbuildmat.2014.03.009.
- 45 898 [30] D. J. Wright, "Building From The Ground Up : Understanding and Predicting The  
 46 899 Strength of Cob , An Earthen Construction Material," The University of Tulsa. PhD  
 47 900 thesis, 2019.
- 48 901 [31] R. H. Saxton, "Performance of cob as a building material," *Struct. Eng. London*, vol.  
 49 902 73, pp. 111–115, 1995.

- 903 [32] Q. M. Pullen and T. V. Scholz, "Index and engineering properties of Oregon Cob," *J.*  
904 *Green Build.*, vol. 6, pp. 88–106, 2011, doi: 10.3992/jgb.6.2.88.
- 905 [33] E. Quagliarini and G. Maracchini, "Experimental and FEM Investigation of Cob Walls  
906 under Compression," *Adv. Civ. Eng.*, vol. 2018, pp. 21–29, 2018, doi:  
907 10.1155/2018/7027432.
- 908 [34] H. Houben and H. Guillaud, *Earth construction: a comprehensive guide*, 1st ed.  
909 London: Intermediate Technology Publications, 1994.
- 910 [35] L. Ziegert, "Konstruktion, Schäden und Sanierung, Berichte aus dem Konstruktiven  
911 Ingenieurbau," Technical University of Berlin. PhD Thesis., 2003.
- 912 [36] K. A. Coventry, "Specification Development for the Use of Devon Cob in Earthen  
913 Construction," University of Plymouth. PhD thesis, 2004.
- 914 [37] G. Minke, *Building with Earth: design and technology of a sustainable architecture*.  
915 Basel: Walter de Gruyter, 2012.
- 916 [38] M. Rizza and H. Bottger, *Effect of Straw Length and Quantity on Mechanical*  
917 *Properties of Cob*. San Francisco, 2015.
- 918 [39] G. Brunello, J. Espinoza, and A. Golitz, "Cob Property Analysis,". Dep of Civil &  
919 Environmental Engineering. Santa Clara University. MSc Thesis., 2018.
- 920 [40] T. Vincenaslas, E. Hamard, A. Razakamanantsoa, and F. Bendahmane, "Further  
921 development of a laboratory procedure to assess the mechanical performance of cob,"  
922 *Environ. Geotech.*, vol. 7, pp. 200–207, 2018, doi: 10.1680/jenge.17.00056.
- 923 [41] A. Jiménez Rios and D. O'Dwyer, "Experimental validation for the application of the  
924 flat jack test in cob walls," *Constr. Build. Mater.*, vol. 254, 2020, doi:  
925 10.1016/j.conbuildmat.2020.119148.
- 926 [42] A. Fabbri, J.-C. Morel, and D. Gallipoli, "Assessing the performance of earth building  
927 materials: a review of recent developments," *RILEM Tech. Lett.*, vol. 3, pp. 46–58,  
928 2018, doi: 10.21809/rilemtechlett.2018.71.
- 929 [43] S. Goodhew, PP. C. Grindley, and S. D. Probeif, "Composition, Effective Thermal  
930 Conductivity And Specific Heat Of Cob Earth-walling," *Trans. Built Environ.*, vol. 15,  
931 pp. 205–213, Jan. 1995, doi: 10.2495/STR950231.
- 932 [44] CEN, "EN 772-1. Methods of test for masonry units - Part 1: Determination of  
933 compressive strength," 2011. [Online]. Available: [https://infostore.saiglobal.com/en-  
934 us/Standards/EN-772-1-2011-A1-2015-331320\\_SAIG\\_CEN\\_CEN\\_761952/](https://infostore.saiglobal.com/en-us/Standards/EN-772-1-2011-A1-2015-331320_SAIG_CEN_CEN_761952/).
- 935 [45] Standards Australia, *AS 1170.1–2002 (R2016) Structural design actions Part 1 :  
936 Permanent , imposed and other actions*. Sydney, NSW: Australian / New Zealand  
937 Standard <sup>TM</sup>, 2002.
- 938 [46] Standards Australia, *Australian Standard for Masonry structures (AS 3700:2018)*.  
939 Sydney, NSW: Australian / New Zealand Standard <sup>TM</sup>, 2018.
- 940 [47] R. McNeel, "Grasshopper - in Rhino 6," 2020.  
941 <https://www.rhino3d.com/6/new/grasshopper> (accessed Jul. 30, 2020).  
942

## GENERAL

We wish to again thank all of the Reviewers for their constructive feedback on how to improve the paper. We have addressed the comments from the second phase of review as follows.

### Reviewer #3

1. In general, writing has been improved but further polishing is still recommended. Issues in writing were still identified regarding:

- Definite/indefinite articles,
- Usage of plurals,
- Frequent use of demonstrative pronouns and demonstrative determiners,
- Incorrect verb constructions,
- Grammatical tense (past tense often wrongly used),
- Usage of contractions is not recommended in scientific writing,
- Capitalization

We have undertaken a thorough proof-read of the paper and addressed as many of these issues as we could identify. Please refer to the marked-up paper with the changes being highlighted in red.

2. In Figure 15 and Figure 16, it is recommended to add a legend to the graphs, similar to Figure 17, denoting which series corresponds to "t" and which one corresponds to "d" (necessary for when the paper is printed in gray scale). The same recommendation applies to Figure 19, Figure 21, and Figure 23.

We have modified the figures by adding a legend as recommended by the Reviewer.

3. It is recommended to only mention future studies in the conclusion section (see Section 4.2.2).

We have identified two such instances in the main text. We deleted one, but retained the other as it is integral to the context of the discussion (on line 297), as follows:

“... thus providing impetus for future investigations into 3DP-suitable cob mix design to focus on not just the material’s strength but also stiffness”

### **Highlights**

- Basic mechanical properties of 3D-printed cob were experimentally quantified.
- Mechanical properties of 3DP cob are shown to be comparable to traditional (non-3DP) cob.
- A model technique for compression design is demonstrated using a limit-state framework.
- Loadbearing 3DP cob wall are shown to be feasible for residential construction up to 2 stories.

### **CRediT author statement**

**Mohamed Gomaa:** Conceptualization, Methodology, Data curation, Formal analysis, Investigation, Resources, Software, Validation, Visualization, Writing - original draft, Writing - review & editing, Project administration, Funding acquisition

**Jaroslav Vaculik:** Conceptualization, Methodology, Data curation, Formal analysis, Investigation, Resources, Software, Validation, Visualization, Writing - original draft, Writing - review & editing.

**Veronica Soebarto:** Conceptualization, Writing - review & editing, Supervision

**Michael Griffith:** Methodology, Writing - review & editing, Supervision

**Wassim Jabi:** Resources, review & editing, funding acquisition

## **Feasibility of 3DP Cob Walls Under Compression Loads in Low-Rise Construction**

Mohamed Gomaa<sup>ae</sup>, Jaroslav Vaculik<sup>b,c\*</sup>, Veronica Soebarto<sup>a</sup>, Michael Griffith<sup>b,c</sup>, Wassim Jabi<sup>d</sup>

<sup>a</sup> School of Architecture and Built Environment, Horace Lamb Building, University of Adelaide, Adelaide SA5005, Australia.

<sup>b</sup> The School of Civil, Environmental and Mining Engineering, Engineering North Building, University of Adelaide, Adelaide SA5005, Australia.

<sup>c</sup> Bushfire and Natural Hazards Cooperative Research Centre, Melbourne, Australia

<sup>d</sup> The Welsh School of Architecture, Bute Building, Cardiff University, Cardiff CF10 3NB, UK.

<sup>e</sup> School of Engineering, B251- RMIT Bundoora East Campus, RMIT University, Melbourne VIC 3083, Australia.

\*Corresponding Author

Postal address: The School of Civil, Environmental and Mining Engineering, Engineering North Building, University of Adelaide, Adelaide SA5005, Australia.

Phone: (+61 8 8313 5451)



**Declaration of interests**

The authors declare that they have no known competing financial interests or personal relationships that could have appeared to influence the work reported in this paper.

The authors declare the following financial interests/personal relationships which may be considered as potential competing interests: